Victorien Emile Prot

Modelling and numerical analysis of the porcine and human mitral apparatus

Thesis for the degree of philosophiae doctor

Trondheim, October 2008

Norwegian University of
Science and Technology
Faculty of Engineering Science and Technology
Department of Structural Engineering

NTNU
Norwegian University of
Science and Technology

NTNU
Norwegian University of Science and Technology

Thesis for the degree of philosophiae doctor

Faculty of Engineering Science and Technology
Department of Structural Engineering

ISBN 978-82-471-1192-5 (printed ver.)
ISBN 978-82-471-1193-2 (electronic ver.)
ISSN 1503-8181

Theses at NTNU, 2008:249

Printed by Tapir Uttrykk

Modelling and numerical analysis of the porcine and human mitral apparatus

Victorien Emile Prot

Norwegian University of Science and Technology

Faculty of Engineering Science and Technology

Department of Structural Engineering

Trondheim, Norway

Preface

This doctoral thesis is submitted to the Norwegian University of Science and Technology (NTNU) for the degree Philosophiae Doctor.
The project work has been carried out at the Departement of Structural Engineering, NTNU. My supervisor has been Professor Bjørn Skallerud and my co–supervisors have been Professor Hans Torp (Circulation and Medical Imaging, NTNU) and Professor Rune Haaverstad (Department of Cardiothoracic Surgery, St. Olav Hospital). The work has been supported by a scolarship from the Norwegian University of Science and Technology, Trondheim, and by Simula School of Research and Innovation AS.

Acknowledgements

First, I would like to acknowledge my supervisor Professor Bjørn Skallerud who initially introduced me to biomechanics and gave me financial backup to pursue the project work. He has always shown great interest and commitment to my work. His ideas and tremendous support had a major influence on this thesis. I have really much appreciated his scientific competence, his critical reviews and his excellent advice. I also want to express my deepest gratitude for his dynamism and his great encouragement and support during all these years. I learnt a lot during this time working with him; thank you very much, Bjørn.

Professor Gerhard H. Holzapfel showed a keen interest in my project. I owe him great thanks for helpful collaboration and for inviting me to the Institute of Biomechanics in Graz to perform experimental work. I also want to thank all the people at the Institute of Biomechanics for their great hospitality and helpfulness.

I would like to thank Professor Rune Haaverstad (Department of Cardiothoracic Surgery, St. Olav Hospital) for supporting me in my plans to obtain ultrasound data. Thanks also to Professor Hans Torp, Dr. Lasse Løvstakken and MD Hans Henrik Dedichen (Department of circulation and medical imaging) and MD Håvard Bersås Nordgaard (Department of Cardiothoracic Surgery, St. Olav Hospital) who helped me with these measurements. Many thanks go to Professor Ivar Nordrum (Department of Laboratory Medicine, Children's and Women's Health) for his generous help in the anatomical study of mitral valves and to Bjarne Bergheim who guided me through my initial studies.

Thanks are also due to the Simula School for financing the end of my PhD period.

I am grateful to the PhD students and colleagues at the Department of Structural Engineering for their professional help and for creating such a nice atmosphere in the lab. Special acknowledgements also go to Espen Berg and Sune Pettersen for their valuable help with Latex, Linux and Matlab.

Johann, Svatopluk, Iva, Enno, Guillaume and Séverine, thank you for your friendship and the social life.

Last but not least, I wish to thank my family for their support and my friends from France for their everlasting friendship.

Contents

Preface **i**

1 Introduction **1**
1.1 Motivations 1
1.2 Aims of the study 2

2 Anatomy and physiology of the mitral valve **5**
2.1 Cardiac cycle 5
2.2 Anatomy 7
2.2.1 The annulus 8
2.2.2 The leaflets 8
2.2.3 The chordae 8
2.2.4 The papillary muscles 9

3 Mitral leaflets and chordae mechanical behaviour **11**
3.1 Chordae 11
3.2 Leaflets 11

4 Introduction to large deformations and hyperelasticity **15**
4.1 Deformation and strain measures 15
4.2 Hyperelasticity 16
4.3 Transversely isotropic hyperelasticity 18
4.4 Stress and elasticity tensors 19

5 Summary of appended papers **23**

6 Conclusions and further work **25**
6.1 Conclusions 25
6.2 Directions for further work 26

PAPER I **33**
1 Introduction 33
2 Continuum Mechanical Framework and Material Models 35
2.1 Kinematics 35
2.2 Incompressible Transversely Isotropic Materials 35
2.3 Strain-Energy Functions for Mitral Valves 37

3 Numerical Examples . . . 46
3.1 Equibiaxial Test Simulation . . . 46
3.2 Out of Plane Loading . . . 46
3.3 Initial Simulations of Mitral Valve Leaflets . . . 51
4 Concluding Remarks . . . 56

PAPER II **63**
1 Introduction . . . 63
2 Methods . . . 65
2.1 Model geometry, boundary conditions and finite element mesh . . . 65
2.2 Material Model . . . 69
3 Results . . . 71
4 Discussion . . . 78
5 Conclusion . . . 80
6 Limitations . . . 80

PAPER III **89**
1 Introduction . . . 89
2 Continuum mechanical framework . . . 91
2.1 Kinematics . . . 91
2.2 Strain energy function . . . 92
2.3 Stress and elasticity tensors . . . 93
3 Numerical examples . . . 95
3.1 Biaxial test simulations . . . 95
3.2 Comparison between solid and membrane elements . . . 97
3.3 Mitral valve simulations . . . 101
4 Discussion . . . 107
5 Conclusion . . . 111

PAPER IV **119**
1 Introduction . . . 119
2 Method . . . 122
2.1 Mechanical testing . . . 122
2.2 Results and optimization . . . 123
2.3 Comparison with porcine data . . . 127
3 Finite element analysis . . . 128
3.1 Geometry, material and boundary conditions . . . 129
3.2 Results . . . 130
4 Discussion . . . 130

Chapter 1

Introduction

This thesis contains an introductory section and four separate papers. The introductory section is organized in six chapters. The first one presents the motivations and the aims of the project. The second chapter gives an overview of the mitral valve anatomy. The third one presents the mechanical behaviour of the mitral leaflets and the chordae tendinae. In the fourth chapter, some basic principles of continuum mechanics are presented briefly in order to describe deformation and stress, and establish constitutive material laws in hyperelasticity. In chapter five, the summaries of the papers are presented. In chapter six, concluding remarks are presented and topics for further research are discussed.

1.1 Motivations

The Mitral valve is one of the four valves of the heart. Located between the left atrium and left ventricle the mitral valve prevents the blood from flowing back into the left atrium when the ventricle contracts (see Figure 1.1). The normal function of the valve depends on the coordinated action of different anatomical parts: the left atrium, the mitral annulus, the mitral leaflets, the chordae tendinae, the papillary muscles and the left ventricle. The mitral apparatus itself consists of two leaflets attached to the annulus,the papillary muscles and the chordae tendinae attached at one end to the leaflets and at the other end to the papillary muscles. The chordae and the papillary muscles are also referred as the subvalvular apparatus. Malfunction or failure of one of these constituents can affect the function of the valve, with further consequence of pathological heart function.

In order to assess pathologies of the mitral valve it is of primary importance to understand the functional characteristics of its different constituents.

The finite element (FE) method is a powerful technique in order to calculate strain and stress distributions in complex structures. FE models have been used to analyse mitral valve response [1], [2], diseases [3] or surgical techniques such as annuloplasty [4] or edge-to-edge repair [5] [6]. Experimental in vitro tests carried out on porcine mitral leaflets [7] showed that both leaflets exhibit highly nonlinear response and are anisotropic. The investigation lead to the formulation of a transversely isotropic hyperelastic constitutive law for porcine mitral valve leaflets [8]. In FE method, the material behaviour is a crucial point in order to calculate accurately the response of a structure.

However, in vivo tissue has a different response compared to in vitro tissue. And in vivo stress

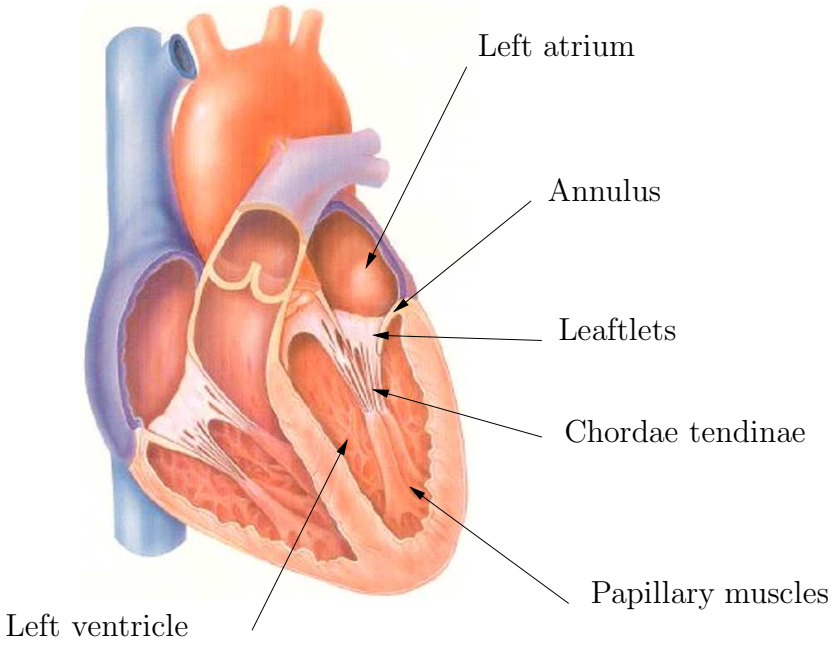

Figure 1.1: Overview of the mitral apparatus.

measurements are not possible. Hence, the validation of the modelling of the mitral apparatus requires comparison of the computed response from the finite element simulation to in vivo measurements.

Imaging techniques such as echocardiography are commonly used to diagnose mitral valve diseases in hospitals. Echocardiographic images provide fine details of tissue motion and blood flow velocities. In addition, information extracted from imaging, such as geometry and measured global motion of the mitral apparatus, can be incorporated in FE models as boundary conditions [9].

With appropriate boundary conditions and constitutive material laws, FE models can be valuable tools in order to describe both geometrical changes and stress–strain distribution in the mitral apparatus. As mechanical stress is of primary importance for evolution of the tissue, FE analysis can be used to estimate stress–strain distributions in the mitral apparatus in order to assess how a disease affect the tissue and help in making decisions for surgical treatments.

1.2 Aims of the study

The main aim of this thesis work has been to develop three-dimensional finite element models combining realistic geometry, boundary conditions and material models for the mitral valve.

As material models have an important role in the accuracy of the FE model, they have to be as close as possible to the reality in order to understand the natural mitral valve function. In [8] the focus was on in vitro biaxial testing of mitral valve tissue, and on the identification of a strain-energy function and material parameters, but not on its numerical implementation. Commercial codes do not contain specialized models for human tissues. These material models for mitral leaflet tissue and chordae tissue are necessary for finite element modelling of the mitral valve

apparatus. We thus wanted to implement transversely isotropic hyperelastic material models in the finite element code `ABAQUS` for membrane-shell elements as a first approach. With this, it is possible to account for the anisotropic behaviour of the leaflet in the simulation of mitral valve in healthy and diseased conditions.

The typical modelling of the annulus is to assume it as flat and rigid whereas we know it has a saddle shape and is non-rigid. The chordae tendinae form a complex network of fibrous strings between the leaflets and the papillary muscles preventing mitral valve prolapse into the left atrium. Hence, we wanted to investigate the influence of the annulus shape variations on the mitral valve response and to characterize the tensions carried by the different types of chordae. This gives a tool to understand the role of the annulus deformations and function of the different chordae tendinae in the response of healthy mitral valve.

The mitral leaflets can be considered as three layered laminated structures: the atrialis on the atrium side, the ventricularis on the ventricular side and the inner fibrosa layer. These layers may have different effects on the stress distributions in the leaflet walls. We wanted to develop a three-dimensional finite element model using continuum elements taking into account the layered structure of the mitral valve. With this, one has a tool to take into account finer details such as variation of leaflets material properties through the thickness and to improve understanding of tissue adaptation.

In vitro mechanical data of porcine mitral tissue are available in the literature. However, human data are not available yet. Hence, we wanted to perform mechanical tests on human mitral valve in order to obtain material parameters for leaflets and chordae tendinae from the same valve. The material parameters would be used in FE models to compare diseased and healthy valves. This can be used to better understand function and adaptation of diseased valves.

Chapter 2

Anatomy and physiology of the mitral valve

2.1 Cardiac cycle

The sequence of events that occur in the heart during one heart beat is called the cardiac cycle. The heart can be seen as a double-acting pump: the left side delivers blood at high pressure into the systemic circulation, while the right side pumps blood through the lungs, i.e., the pulmonary circulation. Coming from the venae cavae, venous blood enters the right atrium. From there it flows into the right ventricle which pumps it into the lungs via the pulmonary arteries. In the lungs the blood is oxygenated and is returned to the left atrium via the pulmonary veins. From there it flows into the left ventricle which pumps it into the aorta and on through the systemic circulation. The blood flow path is controlled by four one-way valves (see Figure 2.1). The inlet valves of the ventricles are called the AV (atrioventricular) valves. They permit blood to flow in one direction only, from the atria to the ventricles. The valve located between the right atrium and the right ventricle is called the tricuspid valve because it has three leaflets, or cups. The valve located between the left atrium and the left ventricle is called the mitral valve because it has only two leaflets, which resemble a bishops miter. The outlet valves of the ventricles are called semilunar valves. They also allow blood to flow in a single direction, from each ventricle into a large outflow-tract vessel. Both the pulmonary valve, located between the right ventricle and pulmonary artery, and the aortic valve, located between the left ventricle and aorta, have three leaflets. The cardiac cycle can be divided into phases, from the point of view of the ventricles and of the positions of their valves, four distinct phases can be considered:

- Inflow phase (phase 1). Inlet valve is open and the outlet valve is closed.
- Isovolumetric contraction (phase 2). Both valves are closed, with no blood flow.
- Outflow phase (phase 3). The outlet valve is open and the inlet valve is closed.
- Isovolumetric relaxation (phase 4). Both valves are closed with no blood flow.

Commonly, the cardiac cycle can also be divided into two phases, diastole and systole (see Figure 2.2). The diastole and the systole are synonymous with the relaxation and contraction of a muscle, respectively. Basically, the ventricles are filled during diastole and the blood is

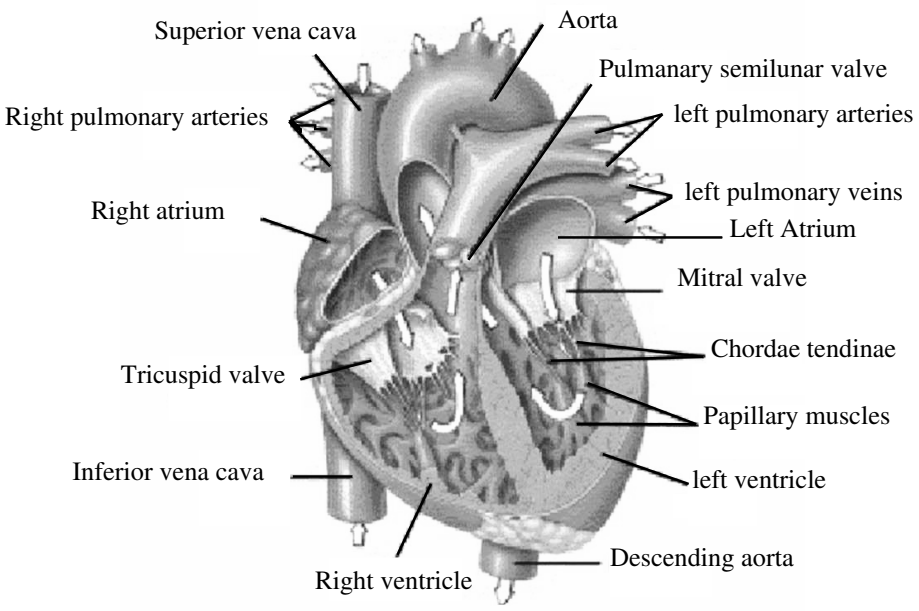

Figure 2.1: Frontal cross section of the heart (the white arrows represent the blood flow path)

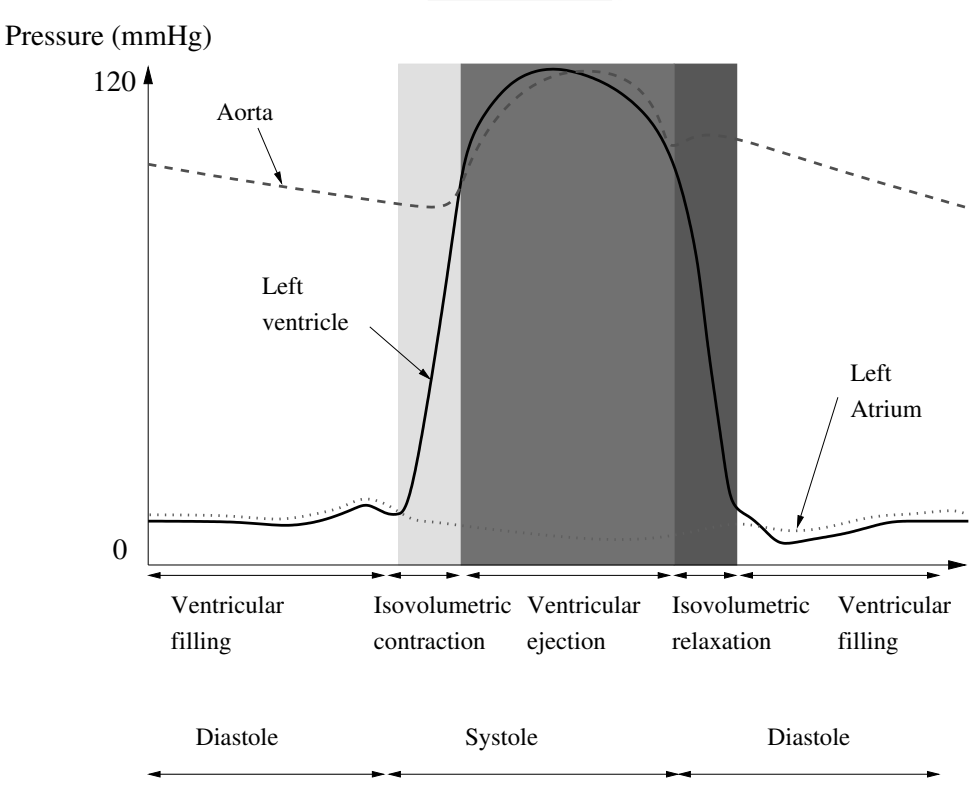

Figure 2.2: Pressures during the cardiac cycle

ejected during systole.
Diastole begins with a period of isovolumetric relaxation, when ventricular pressure decreases. During diastole, when the heart is in a relaxed state, the two ventricles are filling with blood through the wide open tricuspid and mitral valve. Diastole is followed by an energetic contraction of the muscular walls of the two ventricles, leading to a sudden rise in the blood pressure within them and the closure of the tricuspid and mitral valves.
At the beginning of ventricular systole, the pressure in the left ventricle increases, closing the mitral valve. The pressure in the left ventricle continues to rise and when the pressure in the ventricle is greater than the pressure in the aorta, the aortic valve opens, allowing the rapid ejection of blood from the ventricle.

2.2 Anatomy

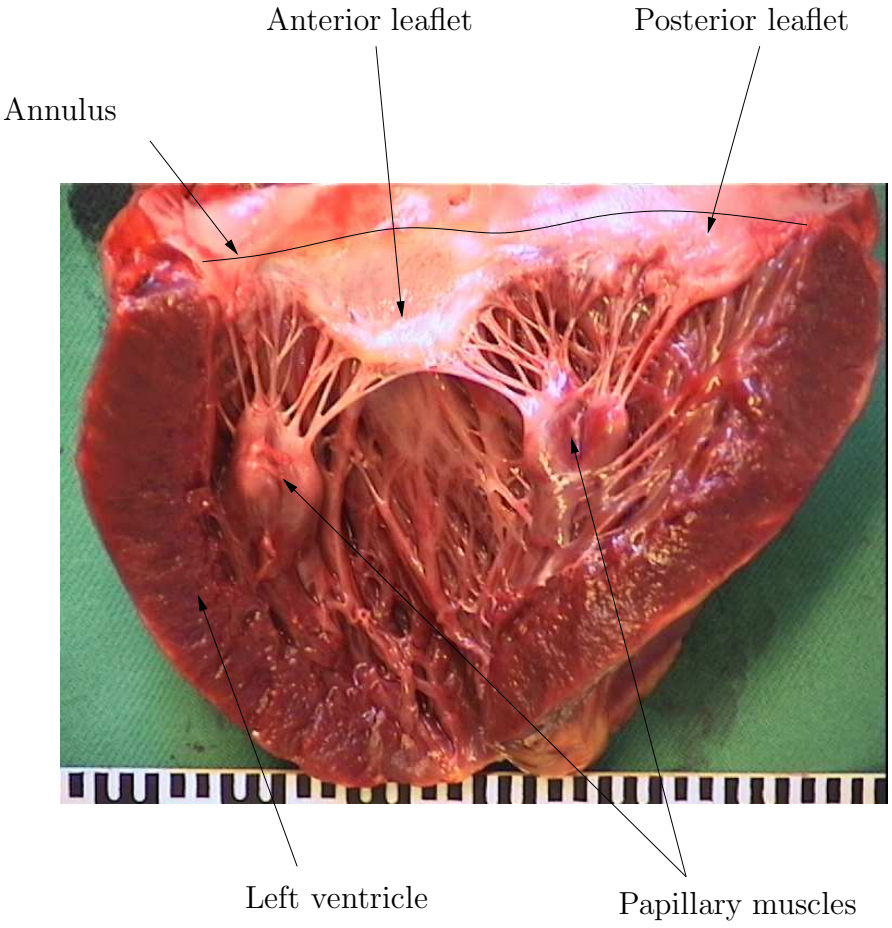

Figure 2.3: Overview of a human mitral apparatus[1]

[1]autopsy picture approved by the Ethics Committee of the Medical Faculty Trondheim

2.2.1 The annulus

The annulus is not a well defined anatomical structure. It can be defined as the line around which the mitral leaflets rotate during opening and closure of the valve. It defines the transition between the left atrium endocardium and the valve leaflets (see Figure 2.3).
The mitral annulus shape and its dynamic behaviour during the cardiac cycle have been studied in animals and humans using different imaging techniques such as two-dimensional and three-dimensional echocardiography, magnetic resonance. The annulus shape is often described as a saddle because of its resemblance to a nonplanar ellipse [11], [12]). The annulus saddle height increases during systole. The annular contraction occurs between end of diastole and beginning of systole [13].

2.2.2 The leaflets

The mitral leaflets represent an uninterrupted structure divided in an anterior (aortic or septal) leaflet and a posterior (mural) leaflet. The two leaflets exhibit some anatomical differences (see Figure 2.3). The anterior leaflet, adjacent to the aortic artery, occupies about one third of the annulus length and is larger than the posterior leaflet. The anterior leaflet has a rounded free margin and is characterized on its atrial surface by a rough zone along the free edge [10] approximatively 1 cm in the middle of the leaflet and narrowing toward the commissural areas. This region is thicker than the rest of the leaflet due to the abundance of chordal insertions. During valve closure this zone comes into contact with the posterior leaflet, view from the atrium the closure line of the valve resembles a smile. The ends of the closure line are referred to as the commissures, which are about 5 mm long from their free margin to the annulus and mark the continuity between the two leaflets. The posterior leaflet occupies two thirds of the annular circumference and is narrower than the anterior leaflet. It is often divided into three scallops. Raghanathan et al. [10] found that the middle scallop is larger than the two others located near the commissural areas.
The principal biochemical components of the mitral leaflets are water, collagen, elastin and glycosaminoglycans [14]. Among these components collagen has the highest stiffness. The mitral leaflets can be divided into three layers: an atrial/spongiosa layer on the atrium side composed of loose connective tissue, the ventricularis layer on the ventricular side composed of elastic fibres and an inner fibrosa layer containing dense collagen. The fibrosa is the thickest layer while the ventricularis is the thinnest layer. The thicknesses of these layers vary from the annulus to the free edge of the leaflets [14].

2.2.3 The chordae

The chordae are fibrous strings that represent the connection between the valve leaflets and the ventricular wall. They originate from the tips of the papillary muscles or directly from the ventricular wall and insert into the valve leaflets.
The chordae attached to the commissure are named commissural chordae and are inserting into the free edge of the commissural region.
Two kinds of chordae attached to the anterior leaflet can be distinguished: the primary chordae or marginal chordae inserted into the free margin and the secondary chordae inserted into the rough zone of the leaflet (beyond the free edge of the leaflet). Often these chordae split into two

or three branches after their origin from the papillary muscle. Among the secondary chordae two are thicker and larger than the other mitral valve chordae and have been observed in 90% of the human hearts [15]. These two chordae are called strut (see Figure 2.4) and have been recently of particular interest (see [16], [17], [18], [19], [20]).

The chordae attached to the posterior leaflet can be divided into three groups. As in the

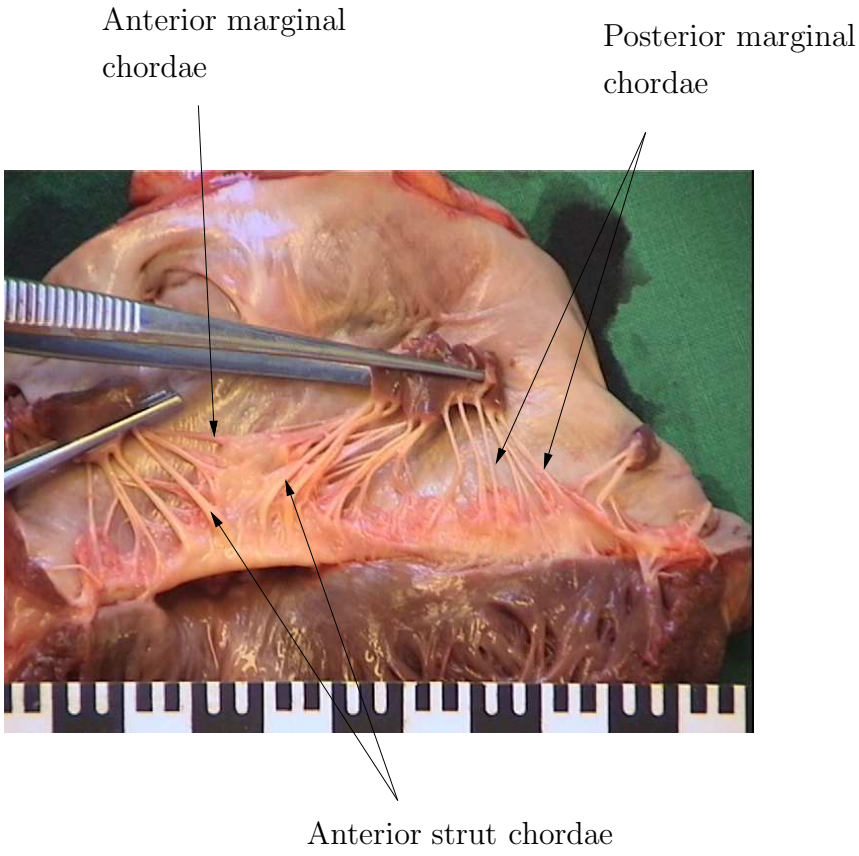

Figure 2.4: View of the ventricular surface of a human mitral valve

anterior leaflet, the primary chordae are inserted into the free margin and the secondary chordae into the rough zone, note the posterior does not have any strut chordae. In addition, a third type of chordae unique to the posterior leaflet can be observed. These chordae insert into the basal region of the leaflet, i.e. near the annulus, and are named third order chordae or basal chordae [15].

2.2.4 The papillary muscles

The left ventricle has two papillary muscles, an anterior one and a posterior one, arising at the junction of the apical and middle thirds of the ventricular free wall (see Figure 2.3). The anterior papillary muscle originates from the anterior wall of the ventricle at its lateral border, and the posterior muscle arises from the posterior wall, at its junction with the ventricular septum. They are usually composed of two or three very closely related structures each com-

ing in contact during ventricular contraction. The apices of the papillary muscles bifurcate or trifurcate into smaller terminations from which chordae tendinae originate [21].
Papillary muscles contraction and elongation have a critical role during the closing and opening phases of the valve leaflets in order to allow coaptation and prevent mitral valve prolapse [21]. Papillary muscles have an essential role in the load bearing of the mitral valve during systole [22]. In addition, in normal subjects both papillary muscle tip and annulus move apically during systole and the relative distance between the papillary muscle tip and annulus plane is nearly constant during systole [23].
At end diastole, the distance from the annulus plane to the papillary muscle tips is approximatively 26 mm and the distance between the two papillary muscles is 22 mm in healthy individuals [24].

Chapter 3

Mitral leaflets and chordae mechanical behaviour

3.1 Chordae

Both human and porcine chordae have been studied. The different mechanical behaviours of both strut and marginal chordae were tested with uniaxial tensile tests [25], [17]. Stress in the marginal chordae is higher than that on the basal ones at all recorded strains. Moreover, marginal chordae are less extensible than strut chordae [25], see Figure 3.1. Hence, the mechanical properties of the chordae are type dependent.
The mechanical behaviour of the chordae tendinae is also dependent on size. Indeed, smaller chordae exhibit less extensibility than larger ones [26], [27].
Some differences in the structure of the chordae constituting the mitral valve appear: thinner chordae are less extensible than thicker chordae and marginal chordae are the thinnest. In addition, collagen fibril crimp period are smaller in thicker chordae than in the thinner ones. Moreover, the marginal chordae have smaller collagen fibril diameters and greater average fibril density than the other types of chordae. However, the area percentages of the chordae occupied by collagen fibrils is nearly constant between all types of chordae. Since thin chordae have smaller collagen fibril diameter than thick chordae, their greater modulus may be due to the greater number of interfibrillar linkages [27].
Regarding failure of the mitral valve chordae tendinae, the marginal chordae and posterior chordae requires less strain and less load to fail than strut chordae and anterior leaflet chordae, respectively [20].

3.2 Leaflets

May-Newman and Yin [8] formulated a strain energy function describing the large deformations of the fibrous architecture of the mitral valve tissue. Their biaxial tests on anterior and posterior porcine mitral leaflets demonstrated that both leaflets exhibited large deformations and behaved anisotropically, being stiffer along the circumferential direction (concentric to the annulus). The posterior leaflet is more extensible than the anterior one. Assuming that the loading and unloading responses could be modeled by the same constitutive law and as the mitral valve

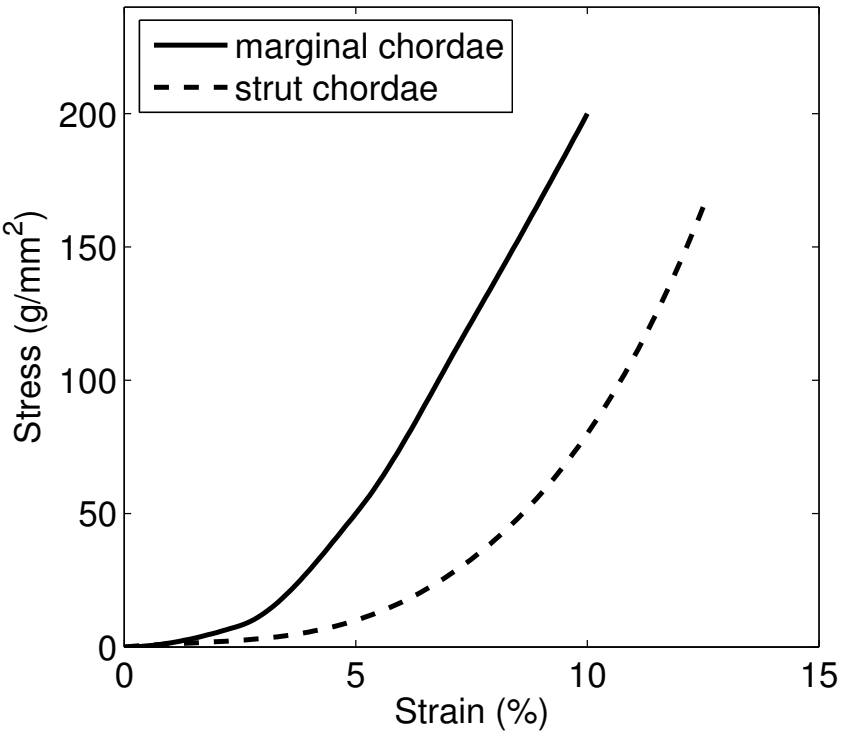

Figure 3.1: Stress/strain behaviour of porcine mitral valve chordae tendinae in uniaxial tension [25]

tissue is composed of an oriented parallel network of crimped collagen fibrils and as the angle of these fibrils is relatively uniform through the thickness and in the region used for testing, they proposed that mitral valve tissue might be modeled as a transversely isotropic material. The strain energy function proposed has an exponential form analogous to the one proposed by Fung et al. [28] to describe arterial mechanical properties:

$$\Psi = c_0 \left(e^{c_1 (I_1 - 3)^2 + c_2 (\alpha - 1)^4} - 1 \right), \tag{3.1}$$

where c_0, c_1, c_2 are material parameters, $I_1 = \mathrm{tr}(\mathbf{C})$ and $\alpha = \mathbf{NCN}$, $\mathbf{C}$ is the right Cauchy strain tensor, $\mathbf{N}$ is a unit vector defining the preferred fibre direction of the material in the undeformed configuration, α is the stretch of the fibre.

The stiffness of the mitral leaflets is mainly due to collagen. The mitral valve leaflets contain highly oriented collagen fibres. The collagen fibres in the central part of both leaflets are oriented parallel to the annulus. In the anterior leaflet, they turn gradually orthogonal to the annulus and insert in the region next to the fibrous trigones [29]. The collagen fibre architecture mapping is provided for both leaflets in [29] and [30].

In vitro studies showed that the central portion of the anterior leaflet in pig undergoes anisotropic strains [31], [32]. The anterior leaflet exhibits a large nonhomogeneous radial stretch and a small circumferential stretch and the principal stretches were maintained at nearly constant values during the closed phase of the valve. It is important to note that these simulations are difficult to validate in vivo with available imaging technologies.

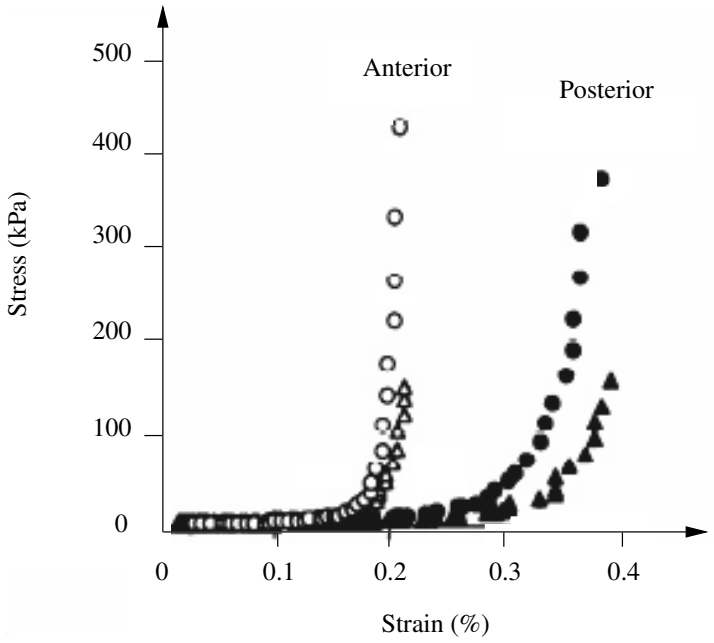

Figure 3.2: Stress–strain relation for posterior and anterior leaflets of one porcine mitral valve. Circles, circumferential direction, triangles, radial directions. This figure is taken from May-Newman and Yin [7].

In addition, the mitral valve leaflets have the ability to withstand loading without time dependent effects [33].

Chapter 4

Introduction to large deformations and hyperelasticity

In this part, some basic principles of continuum mechanics are recalled in order to describe deformation and stress. These principles are used in the development of constitutive model of different constituents of the mitral valve and in the finite element implementation. This chapter is mainly based on the account provided by Holzapfel [34] and Belytschko et al. [35].

4.1 Deformation and strain measures

Consider Ω and Ω_0 as the initial (reference) and deformed (current) configurations, respectively, and the deformation map $\chi(\mathbf{X}) : \Omega_0 \rightarrow \mathbf{R}^3$, which transforms a referential position $\mathbf{X} \in \Omega_0$ of a point P_0 into the related current position $\mathbf{x} = \chi(\mathbf{X}) \in \Omega$ P, see Figure 4.1. Hence, the deformation gradient $\mathbf{F}$ is defined as:

$$\mathbf{F} = \frac{\partial \chi(\mathbf{X})}{\partial \mathbf{X}} = \frac{\partial \mathbf{x}}{\partial \mathbf{X}}. \tag{4.1}$$

$\mathbf{F}$ takes into account large deformations and rotations that are not considered in linear elasticity theory. The Jacobian of the transformation $J = \det\mathbf{F}$ represents the volume dilatation in the neighbourhood of a point P_0 between the instants t and t_0. The axiom of non-interpenetrability gives: $J > 0 \quad \forall \mathbf{X} \quad$ and $\quad \forall t$ (note that for an incompressible material $J = 1$). The right and left Cauchy green tensors are defined as $\mathbf{C} = \mathbf{F}^T\mathbf{F}$ and $\mathbf{B} = \mathbf{F}\mathbf{F}^T$, respectively. $\mathbf{C}$ and $\mathbf{B}$ are symmetric and positive definite tensors and the square root of their principal values are equal to the principal stretches.

Here, we consider two different strain measures: the Green-Lagrange strain tensor $\mathbf{E}$ and the rate of deformation tensor $\mathbf{D}$. $\mathbf{E}$ and $\mathbf{D}$ vanish for any rigid body motion.

The Green strain tensor $\mathbf{E}$ measures the difference of square length of an infinitesimal segment in the current configuration $d\mathbf{x}$ and the reference configuration $d\mathbf{X}$ and is defined as:

$$d\mathbf{x} \cdot d\mathbf{x} - d\mathbf{X} \cdot d\mathbf{X} = 2d\mathbf{X} \cdot \mathbf{E} \cdot d\mathbf{X}. \tag{4.2}$$

As $d\mathbf{x} = \mathbf{F}d\mathbf{X}$, it gives:

$$\mathbf{E} = \frac{1}{2}\left(\mathbf{F}^T\mathbf{F} - \mathbf{1}\right) = \frac{1}{2}\left(\mathbf{C} - \mathbf{1}\right). \tag{4.3}$$

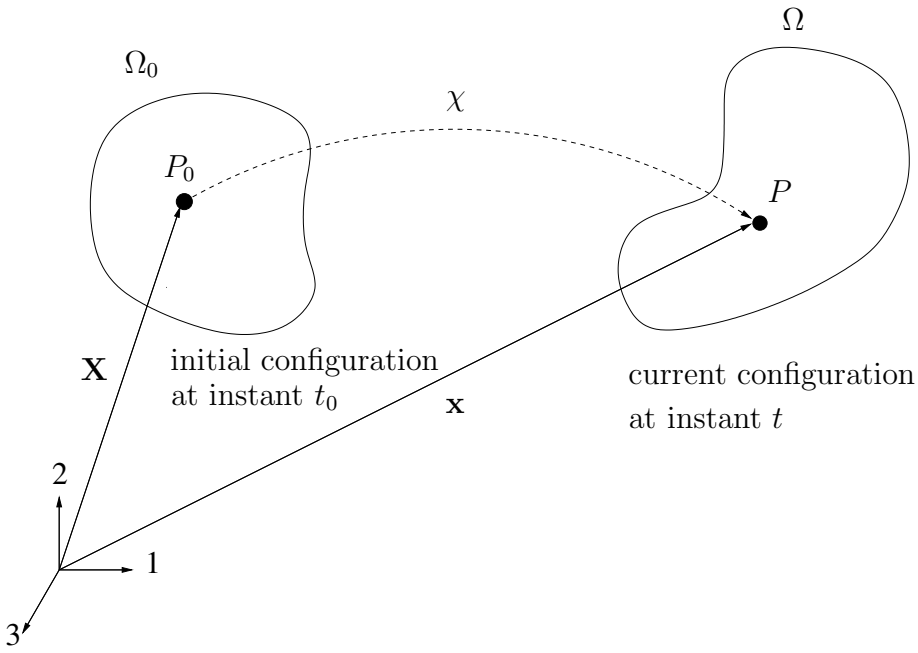

Figure 4.1: Transformation from undeformed to deformed configuration.

Compared to the Green strain tensor $\mathbf{E}$ the rate of deformation tensor $\mathbf{D}$ is a rate measure of deformation. $\mathbf{D}$ is defined as the symmetric part of the velocity gradient $\mathbf{L}$:

$$\mathbf{D} = \frac{1}{2}\left(\mathbf{L} + \mathbf{L}^T\right). \tag{4.4}$$

Note that $\mathbf{L} = \mathbf{D} + \mathbf{W}$, where $\mathbf{W}$ is the skew–symmetric part of $\mathbf{L}$.
The rate of deformation is a measure of the rate change of the square of the length of an infinitesimal material line segment:

$$\frac{\partial}{\partial t}\left(d\mathbf{x} \cdot d\mathbf{x}\right) = 2d\mathbf{x} \cdot \mathbf{D} \cdot d\mathbf{x}. \tag{4.5}$$

Note also the relation between the time derivative of the Green strain tensor $\dot{\mathbf{E}}$ and the rate of deformation tensor $\mathbf{D}$:

$$\dot{\mathbf{E}} = \mathbf{F}^T\mathbf{D}\mathbf{F}, \quad \mathbf{D} = \mathbf{F}^{-T}\dot{\mathbf{E}}\mathbf{F}^{-1}. \tag{4.6}$$

4.2 Hyperelasticity

Hyperelasticity is a suitable nonlinear constitutive theory in order to describe physical phenomena undergoing finite strains such as extension of ligaments or tendons and blood vessels subjected to an internal pressure. From a mechanical point of view, a hyperelastic material has a purely reversible behaviour, i.e. the loading and unloading stress strain curves are identical and the original shape is recovered upon unloading. In addition, a hyperelastic material is path–independent, i.e. the stress and the strain energy depend only on the current level of strain and not on the strain history. Moreover, it has non dissipative behaviour: the energy expended in deformation is stored in the material and can be recovered upon unloading. Finally,

it is rate–independent, i.e. the behavior is insensitive to the strain rate.
A hyperelastic material assumes the existence of a free energy function Ψ defined here per unit reference volume, which is a thermodynamic potential. Only isothermal (constant temperature) transformations are considered here and the strain energy function $\Psi = \Psi(\mathbf{F})$ is only a function of $\mathbf{F}$.
Let's choose the energy conjugate pair of objective tensors $\mathbf{P}$ and $\mathbf{F}$, where $\mathbf{P}$ is the first Piola–Kirchhoff stress tensor. The Clausius–Planck inequality becomes an equality for hyperelastic materials as they have a reversible behaviour from a mechanical point of view:

$$\mathcal{D}_{int} = \mathbf{P} : \dot{\mathbf{F}} - \frac{\partial \Psi}{\partial t} = \left(\mathbf{P} - \frac{\partial \Psi}{\partial \mathbf{F}} \right) : \dot{\mathbf{F}} = 0, \tag{4.7}$$

where $\mathcal{D}_{int}$ is the internal dissipation, $\mathbf{P} : \dot{\mathbf{F}}$ the stress power and $\frac{\partial \Psi}{\partial t}$ the rate of internal energy. As eq.(4.7) must be satisfied for an arbitrary tensor $\dot{\mathbf{F}}$, we obtain:

$$\mathbf{P} - \frac{\partial \Psi}{\partial \mathbf{F}} = 0, \quad \text{and} \quad \mathbf{P} = \frac{\partial \Psi}{\partial \mathbf{F}}. \tag{4.8}$$

Hence, a given strain energy function Ψ is sufficient to describe a hyperelastic behaviour. Note that $\dot{\mathbf{F}}$ is not an objective tensor. However, as in the constitutive law eq.(4.8) with the pair ($\mathbf{P}$, $\mathbf{F}$), $\dot{\mathbf{F}}$ is not involved, it is not necessary to replace it with an objective derivative.
Choosing the pair $\mathbf{S}$ and $\mathbf{E}$ of objective tensors, where $\mathbf{S}$ is the second Piola–Kirchhoff stress tensor, we would obtain using Clausius–Plank form:

$$\mathbf{S} = \frac{\partial \Psi}{\partial \mathbf{E}}, \tag{4.9}$$

and as $\mathbf{C} = 2\mathbf{E} + \mathbf{1}$,

$$\mathbf{S} = \frac{\partial \Psi}{\partial \mathbf{E}} = 2\frac{\partial \Psi}{\partial \mathbf{C}}, \tag{4.10}$$

A consequence from the objectivity principle or material frame invariance principle is that the strain energy function Ψ must be objective, i.e. independent of an observer. Thus, the strain energy function $\Psi = \Psi(\mathbf{F})$ must obey:

$$\Psi(\mathbf{QF}) = \Psi(\mathbf{F}), \tag{4.11}$$

for all orthogonal tensors $\mathbf{Q}$ and for all tensors $\mathbf{F}$ with $\det\mathbf{F} > 0$, i.e. the strain energy is unaffected by rigid rotations and translations of the current configuration. Choosing $\mathbf{Q} = \mathbf{R}^T$, where $\mathbf{R}$ is defined by the right polar decomposition of the deformation gradient $\mathbf{F}$, we find that $\Psi(\mathbf{F}) = \Psi(\mathbf{R}^T\mathbf{F}) = \Psi(\mathbf{R}^T\mathbf{RU})$ using $\mathbf{F} = \mathbf{RU}$ and:

$$\Psi(\mathbf{F}) = \Psi(\mathbf{U}). \tag{4.12}$$

Eq.(4.12) shows the strain energy does not depend on the rotation $\mathbf{R}$, but only depends on the stretch tensor $\mathbf{U}$ that characterizes the local stretching at a given material point. In fact, the value of the strain energy function is independent of deformation tensor chosen in the description. Indeed, $\mathbf{E}$ and $\mathbf{C}$ being functions of $\mathbf{U}$, we also have:

$$\Psi(\mathbf{F}) = \Psi(\mathbf{U}) = \Psi(\mathbf{C}) = \Psi(\mathbf{E}). \tag{4.13}$$

In addition, the strain energy must be unchanged by rotations and translations of the reference configuration. In the case of isotropy, we say that a material is isotropic relative to the reference configuration if for a strain energy function of a form $\Psi = \Psi(\mathbf{F})$:

$$\Psi(\mathbf{F}) = \Psi(\mathbf{F}\mathbf{Q}^T), \tag{4.14}$$

for all orthogonal tensors $\mathbf{Q}$ and for all tensors $\mathbf{F}$ with det$\mathbf{F} > 0$, or if the strain energy function adopts the form $\Psi(\mathbf{F}) = \Psi(\mathbf{C})$ (see eq.(4.13)),

$$\Psi(\mathbf{C}) = \Psi(\mathbf{Q}\mathbf{C}\mathbf{Q}^T), \tag{4.15}$$

for all orthogonal tensors $\mathbf{Q}$ and for all symmetric tensors $\mathbf{C}$.

4.3 Transversely isotropic hyperelasticity

For a material reinforced by only one family of fibres as it can be the case for some biological tissues composed of a matrix material and reinforced by one collagen fibre family, the stress response to a given applied load does not only depend on $\mathbf{F}$ but also on the fibre direction called the preferred direction. In the plane perpendicular to the preferred direction, the material response is isotropic. This kind of material are referred to as transversely isotropic material with respect to this preferred direction.
One approach in order to derive transversely isotropic hyperelastic constitutive material model is to introduce a unit vector field $\mathbf{a}_0(\mathbf{X})$ representing the direction of a fibre at a point $\mathbf{X}$ in the reference configuration Ω_0 directly in the strain energy function. Then, the strain energy function Ψ may be written as a function of the second order tensors $\mathbf{C}$ and $\mathbf{a}_0 \otimes \mathbf{a}_0$:

$$\Psi = \Psi(\mathbf{C}, \mathbf{a}_0 \otimes \mathbf{a}_0). \tag{4.16}$$

As $\mathbf{C}$ and $\mathbf{a}_0 \otimes \mathbf{a}_0$ are material tensors, they are unaffected by rigid body motions superimposed to the current configuration. Hence, the principle of material frame invariance is satisfied for the strain energy function $\Psi(\mathbf{C}, \mathbf{a}_0 \otimes \mathbf{a}_0)$.
Moreover, an other requirement for the strain energy $\Psi(\mathbf{C}, \mathbf{a}_0 \otimes \mathbf{a}_0)$ is to be unchanged by rotations in the reference configuration of both the matrix material and the fibres. Hence, Ψ must obey:

$$\Psi(\mathbf{C}, \mathbf{a}_0 \otimes \mathbf{a}_0) = \Psi(\mathbf{Q}\mathbf{C}\mathbf{Q}^T, \mathbf{Q}\mathbf{a}_0 \otimes \mathbf{a}_0\mathbf{Q}^T), \tag{4.17}$$

for all orthogonal tensors $\mathbf{Q}$ and for all symmetric tensors $\mathbf{C}$. A hyperelastic material is said to be transversely isotropic with respect to a reference configuration if eq.(4.17) is satisfied.
According to Spencer [36], function (4.16) may be expressed in terms of five invariants. Thus

$$\tilde{\Psi}(\mathbf{C}, \mathbf{a}_0 \otimes \mathbf{a}_0) = \Psi^*(I_1, \ldots, I_5), \tag{4.18}$$

where I_1, I_2, I_3 are the three invariants related to isotropic hyperelasticity, while

$$I_4 = \mathbf{a}_0 \cdot \mathbf{C}\mathbf{a}_0, \quad I_5 = \mathbf{a}_0 \cdot \mathbf{C}^2\mathbf{a}_0 \tag{4.19}$$

are two pseudo invariants of $\mathbf{C}$ and $\mathbf{a_0} \otimes \mathbf{a_0}$. Note that I_4 in $(4.19)_1$ is the square of the stretch in the fibre direction.

4.4 Stress and elasticity tensors

For a hyperelastic material, the second Piola–Kirchhoff stress tensor $\mathbf{S}$ is derived from the strain energy function Ψ (see eq.(4.9) and eq.(4.10)). The Cauchy stress tensor $\boldsymbol{\sigma}$ is calculated by the push–forward operation of $\mathbf{S}$ into the current configuration:

$$\boldsymbol{\sigma} = \frac{1}{J}\mathbf{F}\mathbf{S}\mathbf{F}^T. \tag{4.20}$$

The material elasticity tensor $\mathbb{C}$ is defined as:

$$\mathbb{C} = \frac{\partial^2 \Psi}{\partial \mathbf{E} \partial \mathbf{E}} = 4\frac{\partial^2 \Psi}{\partial \mathbf{C} \partial \mathbf{C}}. \tag{4.21}$$

It is a fourth order tensor that gives the following relation between the material time derivatives of $\mathbf{S}$ and $\mathbf{E}$:

$$\dot{\mathbf{S}} = \mathbb{C} : \dot{\mathbf{E}}. \tag{4.22}$$

Note that for a hyperelastic material $\mathbb{C}$ possesses the major and minor symmetries.
The spatial description the elasticity tensor is defined as the push-forward operation of $\mathbb{C}$ as:

$$\mathbb{c} = \boldsymbol{\chi}_*(\mathbb{C}), \quad c_{ijkl} = \frac{1}{J}F_{iI}F_{jJ}F_{kK}F_{lL}C_{IJKL}. \tag{4.23}$$

$\mathbb{c}$ is also referred as the spatial tangent moduli and gives the following relationship,

$$\mathcal{L}_{\mathcal{V}}\boldsymbol{\tau} = \dot{\boldsymbol{\tau}} - \mathbf{L}\boldsymbol{\tau} - \boldsymbol{\tau}\mathbf{L}^T = J\mathbb{c} : \mathbf{D} \tag{4.24}$$

where $\boldsymbol{\tau} = J\boldsymbol{\sigma}$ is the Kirchhoff stress tensor, $\mathbf{L}$ the velocity gradient, $\mathbf{D}$ the rate of deformation, and $\mathcal{L}_{\mathcal{V}}\boldsymbol{\tau}$ the convected rate of the Kirchhoff stress, also called the Lie derivative of the Kirchhoff stress.
Other objective stress rates that can be used are the Jaumann stress rate$\boldsymbol{\tau}^{\nabla \mathcal{J}}$ or the Green-Naghdi stress rate $\boldsymbol{\tau}^{\nabla \mathcal{G}}$. Then the Jaumann (Kirchhoff) tangent moduli $\mathbb{C}^{\tau \mathcal{J}}$ and the Green-Naghdi (Kirchhoff) tangent moduli $\mathbb{C}^{\tau \mathcal{G}}$ give the following relation between $\boldsymbol{\tau}^{\nabla \mathcal{J}}$ and $\mathbf{D}$ and $\boldsymbol{\tau}^{\nabla \mathcal{G}}$ and $\mathbf{D}$, respectively:

$$\boldsymbol{\tau}^{\nabla \mathcal{J}} = \mathbb{C}^{\tau \mathcal{J}} : \mathbf{D}, \quad \boldsymbol{\tau}^{\nabla \mathcal{G}} = \mathbb{C}^{\tau \mathcal{G}} : \mathbf{D}. \tag{4.25}$$

These tangent moduli are useful for the implementation of constitutive material law in a finite element code. Now we provide explicit expressions and relations between the different tangent moduli (Jaumann and Green-Naghdi) for incompressible materials. The Jaumann objective stress rate $\boldsymbol{\tau}^{\nabla \mathcal{J}}$ is used in `ABAQUS`/Standard for continuum elements:

$$\boldsymbol{\tau}^{\nabla \mathcal{J}} = \dot{\boldsymbol{\tau}} - \mathbf{W}\boldsymbol{\tau} - \boldsymbol{\tau}\mathbf{W}^T = \mathbb{C}^{\tau \mathcal{J}} : \mathbf{D}, \tag{4.26}$$

where $\mathbb{C}^{\tau \mathcal{J}}$is the Jaumann (Kirchhoff) tangent moduli. This leads to the following relation between the spatial second elasticity tensor $\mathbb{c}$ defined by eq.(4.23) and the Jaumann (Kirchhoff)

tangent moduli $\mathbb{C}^{\tau\mathcal{J}}$,

$$\begin{aligned}
\mathcal{L}_{\mathcal{V}}\boldsymbol{\tau} &= \boldsymbol{\tau}^{\nabla\mathcal{J}} - (\mathbf{L}-\mathbf{W})\boldsymbol{\tau} - \boldsymbol{\tau}(\mathbf{L}-\mathbf{W})^T = J\mathbb{C} : \mathbf{D} \\
&= \boldsymbol{\tau}^{\nabla\mathcal{J}} - \mathbf{D}\boldsymbol{\tau} - \boldsymbol{\tau}\mathbf{D}, && (4.27)\\
J\mathbb{C} : \mathbf{D} &= \mathbb{C}^{\tau\mathcal{J}} : \mathbf{D} - J\mathbb{C}^{'} : \mathbf{D}, && (4.28)\\
\text{with} \quad \mathbb{C}^{'} : \mathbf{D} &= \mathbf{D}\boldsymbol{\sigma} + \boldsymbol{\sigma}\mathbf{D}, && (4.29)\\
\text{and} \quad C^{'}_{ijkl} &= \frac{1}{2}(\delta_{ik}\sigma_{jl} + \delta_{il}\sigma_{jk} + \delta_{jk}\sigma_{il} + \delta_{jl}\sigma_{ik}), && (4.30)\\
\text{then} \quad \mathbb{C}^{\tau\mathcal{J}} &= J\left(\mathbb{C} + \mathbb{C}^{'}\right) && (4.31)
\end{aligned}$$

The fourth order tensor $\mathbb{C}^{'}$ possesses the major and minor symmetries. $\mathbb{C}^{\tau\mathcal{J}}$ is the Jaumann (Kirchhoff) tangent moduli which must be implemented in the ABAQUS/Standard user subroutine UMAT for continuum elements.
In matrix notation, $\mathbb{C}^{'}$ is expressed as:

$$[\mathbb{C}^{'}] = \begin{bmatrix}
2\sigma_{11} & 0 & 0 & \sigma_{12} & \sigma_{13} & 0 \\
0 & 2\sigma_{22} & 0 & \sigma_{21} & 0 & 0 \\
0 & 0 & 2\sigma_{33} & 0 & \sigma_{31} & \sigma_{32} \\
\sigma_{21} & \sigma_{12} & 0 & \frac{1}{2}\sigma_{22} + \frac{1}{2}\sigma_{11} & \frac{1}{2}\sigma_{23} & \frac{1}{2}\sigma_{13} \\
\sigma_{31} & 0 & \sigma_{13} & \frac{1}{2}\sigma_{32} & \frac{1}{2}\sigma_{33} + \frac{1}{2}\sigma_{11} & \frac{1}{2}\sigma_{12} \\
0 & \sigma_{32} & \sigma_{23} & \frac{1}{2}\sigma_{31} & \frac{1}{2}\sigma_{21} & \frac{1}{2}\sigma_{33} + \frac{1}{2}\sigma_{22}
\end{bmatrix}. \qquad (4.32)$$

The relation between the Green-Naghdi rate of Kirchhoff stress $\boldsymbol{\tau}^{\nabla\mathcal{G}}$ and the rate of deformation tensor $\mathbf{D}$ reads:

$$\boldsymbol{\tau}^{\nabla\mathcal{G}} = \dot{\boldsymbol{\tau}} - \boldsymbol{\Omega}\boldsymbol{\tau} - \boldsymbol{\tau}\boldsymbol{\Omega}^T = \mathbb{C}^{\tau\mathcal{G}} : \mathbf{D}, \qquad (4.33)$$

where $\boldsymbol{\Omega}$ is the angular velocity tensor, $\boldsymbol{\Omega}$ is skew-symmetric.

$$\boldsymbol{\Omega} = \dot{\mathbf{R}}\mathbf{R}^T, \qquad (4.34)$$

where $\mathbf{R}$ is an orthogonal tensor defined such as $\mathbf{F} = \mathbf{V}\mathbf{R}$, where $\mathbf{V}$ is the left stretch tensor.

The relation between the Lie derivative and the Green-Naghdi rate of the Kirchhoff stress is:

$$\begin{aligned}
\mathcal{L}_{\mathcal{V}}\boldsymbol{\tau} &= \boldsymbol{\tau}^{\nabla\mathcal{G}} - \mathbf{D}\boldsymbol{\tau} - \boldsymbol{\tau}\mathbf{D} - (\mathbf{W}-\boldsymbol{\Omega})\boldsymbol{\tau} - \boldsymbol{\tau}(\mathbf{W}-\boldsymbol{\Omega})^T, && (4.35)\\
J\mathbb{C} : \mathbf{D} &= \mathbb{C}^{\tau\mathcal{G}} : \mathbf{D} - J\mathbb{C}^{'} : \mathbf{D} - J\mathbb{C}^{*} : \mathbf{D}, && (4.36)\\
\text{where,} \quad & \mathbb{C}^{*} : \mathbf{D} = (\mathbf{W}-\boldsymbol{\Omega})\boldsymbol{\sigma} + \boldsymbol{\sigma}(\mathbf{W}-\boldsymbol{\Omega})^T, && (4.37)\\
\text{then} \quad \mathbb{C}^{\tau\mathcal{G}} &= J\left(\mathbb{C} + \mathbb{C}^{'} + \mathbb{C}^{*}\right). && (4.38)
\end{aligned}$$

Mehrabadi and Nemat-Nasser [40] showed that the term $(\mathbf{W}-\boldsymbol{\Omega})$ can be expressed as:

$$\mathbf{W} - \boldsymbol{\Omega} = \boldsymbol{\Lambda} : \mathbf{D}. \qquad (4.39)$$

$\mathbf{\Lambda}$ is a fourth order tensor defined by:

$$\mathbf{\Lambda} : \mathbf{D} = \frac{1}{I_{1\mathbf{V}} I_{2\mathbf{V}} - I_{3\mathbf{V}}} \left(I_{1\mathbf{V}}^2 (\mathbf{VD} - \mathbf{DV}) - I_{1\mathbf{V}} (\mathbf{BD} - \mathbf{DB}) + \mathbf{BDV} - \mathbf{VDB} \right), \tag{4.40}$$

$$\text{where} \quad I_{1\mathbf{V}} = \text{tr}(\mathbf{V}), \quad I_{2\mathbf{V}} = \frac{1}{2}(\text{tr}(\mathbf{V})^2 - \text{tr}(\mathbf{V}^2)), \quad I_{3\mathbf{V}} = \det(\mathbf{V}). \tag{4.41}$$

$\mathbf{W}$ and $\mathbf{\Omega}$ are both skew symmetric then $\mathbf{W} - \mathbf{\Omega}$ is also skew-symmetric, this gives the following expression for $\mathbb{C}^*$:

$$\begin{aligned} \mathbb{C}^* : \mathbf{D} &= (\mathbf{W} - \mathbf{\Omega})\boldsymbol{\sigma} - \boldsymbol{\sigma}(\mathbf{W} - \mathbf{\Omega}) \\ &= (\mathbf{\Lambda} : \mathbf{D})\boldsymbol{\sigma} - \boldsymbol{\sigma}(\mathbf{\Lambda} : \mathbf{D}), \end{aligned} \tag{4.42}$$

$$C^*_{ijkl} D_{kl} = \Lambda_{imkl} D_{kl} \sigma_{mj} - \sigma_{im} \Lambda_{mjkl} D_{kl}, \tag{4.43}$$

$$C^*_{ijkl} = \Lambda_{imkl} \sigma_{mj} - \sigma_{im} \Lambda_{mjkl}. \tag{4.44}$$

In index notation, $\mathbf{\Lambda}$ is expressed as:

$$\begin{aligned} \Lambda_{ijkl} \quad = \quad & \frac{1}{I_{1\mathbf{V}} I_{2\mathbf{V}} - I_{3\mathbf{V}}} (I_{1\mathbf{V}}^2 \frac{1}{2} (\delta_{jl} V_{ik} + \delta_{jk} V_{il} - (\delta_{ik} V_{jl} + \delta_{il} V_{jk})) \\ & - I_{1\mathbf{V}} \frac{1}{2} (\delta_{jl} B_{ik} + \delta_{jk} B_{il} - (\delta_{ik} B_{jl} + \delta_{il} B_{jk})) \\ & + \frac{1}{2} (B_{ik} V_{lj} + B_{il} V_{kj} - (V_{ik} B_{lj} + V_{il} B_{kj}))). \end{aligned} \tag{4.45}$$

Note that $\mathbf{\Lambda}$ does not have the major symmetries but possesses minor symmetry and skew symmetry:

$$\Lambda_{ijkl} \neq \Lambda_{klij} \tag{4.46}$$

$$\Lambda_{ijkl} = \Lambda_{ijlk} = -\Lambda_{jikl} \tag{4.47}$$

The following terms of $\mathbf{\Lambda}$ are equal to zero:

$$\Lambda_{1111} = \Lambda_{1122} = \Lambda_{1112} = \Lambda_{2211} = \Lambda_{2222} = \Lambda_{2212} = 0. \tag{4.48}$$

Chapter 5

Summary of appended papers

Transversely isotropic membrane shells with application to mitral valve mechanics. Constitutive modeling and finite element implementation
V. Prot, B. Skallerud, G. A. Holzapfel
International Journal for Numerical Methods in Engineering 71(8):987–1008, 2007
Constitutive modelling and implementation of transversely isotropic material models for finite element analysis of mitral valve are presented for two convex strain energy potential. Implementation is checked with single element tests and an out–of–plane loading example and initial simulations of mitral valve leaflets are conducted.

Finite element analysis of the mitral apparatus: annulus shape effect and chordal force distribution.
V. Prot, R. Haaverstad, B. Skallerud
Biomechanics and Modeling in Mechanobiology. Accepted, 2007.
A porcine mitral apparatus using a hyperelastic transversely isotropic material model for the leaflets is analysed using a three dimensional finite element model. Annulus deformations extracted from echocardiographic measurements are used as boundary conditions and chordal force distribution is described between early and peak systole.

Nonlinear solid finite element analysis of mitral valves with heterogeneous leaflet layers
V. Prot, B. Skallerud
Computational Mechanics. Accepted 2008
An implementation of an incompressible hyperelastic transversely isotropic material for solid finite element analysis of mitral valve response is presented. The implementation is compared in an out–of–plane loading example to a membrane implementation. The influence of the collagen structure of the mitral leaflets on mitral valve response is investigated with different layer arrangements.

Healthy and hypertrophic obstructive cardiomyopathic human mitral valves and chordae tendinae: mechanical experiments, constitutive modelling, finite element analyses
V. Prot, B. Skallerud, G. Sommer, G. A. Holzapfel
Submitted, 2008
Uniaxial mechanical tensile tests of a healthy and a diseased (HOCM) human mitral valve are

presented. These experimental data are used in two finite element case studies to investigate the effects of the material properties on mitral valve response. The finite element analyses show that the HOCM human mitral valve undergoes much larger deformations than the healthy human mitral valve during systole.

Other aspects have been presented:

On numerical modelling and analysis of the human mitral valve
V. Prot, B. Skallerud
17th Nordic Seminar on computational mechanics, Stockholm, 2004.

An improved transversely isotropic hyperelastic material model for simulation of mitral valve response
V. Prot, B. Skallerud
Journal of Biomechanics, Volume 39, Supplement 1, 2006, Page S618. Presented as a poster in the 5th World Congress of Biomechanics, Munich, 2006.

Finite element analysis of the influence of the chordae on the mitral valve response
V. Prot, B. Skallerud
19th Nordic Seminar on computational mechanics, Lund, 2006.

Effects of connective tissue pathologies on mitral valve response
V. Prot, B. Skallerud, G. A. Holzapfel
MHM 2007, Modelling of heterogeneous materials with applications in construction and biomedical engineering, Prague, 106-107, 2007.

Solid versus membrane finite elements in analysis of the mitral valve: a case study
V. Prot, B. Skallerud
The 6th International Conferense on Computation of Shell and Spatial Structures, IASS-IACM 2008: "Spanning Nano to Mega", 28-31 May 2008, Cornell University, Ithaca, NY, USA

Mitral valve finite element analysis using human uniaxial tensile data
V. Prot, B. Skallerud, G. A. Holzapfel
8th. World Congress on Computational Mechanics (WCCM8), 5th European Congress on Computational Methods in Applied Sciences and Engineering (ECCOMAS 2008), June 30 –July 5, 2008, Venice, Italy

Chapter 6

Conclusions and further work

6.1 Conclusions

In this study two implementations of a transversely isotropic hyperelastic material model are presented based on invariant formulation for the simulation of mitral valve leaflets.
In the first one for membrane shell elements, incompressibility is explicitly accounted for using the plane stress condition. In the second one for solid elements, incompressibility was treated via a penalty method.
A polyconvex strain-energy function similar to the one proposed by Holzapfel et al. [37] for the simulation of blood vessels is employed in the formulation of the constitutive law and fitted to mitral valve tissue test results provided by May-Newman and Yin [8]. In addition, the model used in this study only requires three material parameters.

We used a three dimensional finite element model using membrane elements to study the mitral valve response during systole. This thesis shows the supportive role of strut (secondary) chordae on the mitral valve systolic function and their importance in order to reduce the apical motion of the anterior leaflets. In addition, we introduced the annulus flexibility by measuring the deformations of the annulus from three dimensional echocardiographic recordings. Our results show that when increasing the annulus saddle height in the physiological regime during systole the anterior leaflets stresses and the chordal force distribution are not significantly affected. Moreover, we showed that the principal stress are aligned with the fibre direction in the anterior leaflet. The stresses in the mitral apparatus are sensitive to the thickness employed and to the pressure level during systole whereas the deformations remain nearly constant after complete coaptation of the leaflets.

We developed a three dimensional finite element model of the mitral valve using solid elements. Membrane elements may be sufficient to capture the global response of the mitral valve. However, in order to assess finer details such as the stress distribution through the thickness of the leaflets solid finite elements are needed. In addition, we observed using a passive transversely isotropic hyperelastic material model a too large deflection of the leaflets in the left atrium. This may be due to the presence of active muscle fibres in the mitral leaflets [38], [13].

6.2 Directions for further work

Since chordae tendinae are tendon-like and collagen fibres are very much aligned, they should be modeled with transversely isotropic material model.

This research project has used passive mechanical data in order to model mitral leaflets. However, the muscles fibres seem to be a crucial component in the mitral leaflet response. A future development of material models should include their contribution to the transversely isotropic constitutive model implemented in the present work. Hence, anatomical and mechanical data on the muscle fibres in the mitral leaflets are needed.

According to previous studies [14], [39] the mitral leaflets can be considered as three layered laminated structures, each layer having different mechanical behaviour. These layer specific data are currently missing and need further research.

This study has used porcine material data for the modelling of the mitral leaflets and chordae. This data may correspond well to children. However, the mechanical behaviour for adult human tissue may be rather different since extensibility of soft tissue decreases with age. Hence, age specific human material data need further investigations.

Collagen fibre orientation has been reported in pigs mitral valve leaflets [29]. However, little is know about collagen fibres local density and their distribution through the thickness of the leaflets. Advanced microscopy may be a valuable tool in order to extract more information on these fibres.

The hemodynamics in the left ventricle and its interaction with the mitral valve is highly relevant in order to understand the global function of the heart. Two dimensional fluid structure interaction models have been developed. Now, three dimensional fluid structure interaction models need to be developed in order to study the interaction between the mitral valve dynamics, the blood flow and the left ventricle.

Bibliography

[1] K. S. Kunzelman, R. P. Cochran, C. Chuong, W. S. Ring, E. D. Verrier, and R. D. Eberhart. Finite element analysis of the mitral valve. *Journal of Heart Valve Disease*, 2:326–340, 1993.

[2] D. R. Einstein, K. Kunzelman, P. Reinhall, M. Nicosia, and R. P. Cochran. Haemodynamic determinants of the mitral valve closure sound: a finite element study. *Med. & Biol. Eng. & Comput.*, 42:832–846, 2004.

[3] R. P. Cochran and K. S. Kunzelman. Effect of Papillary Muscle Position on Mitral Valve Function: Relationship to Homografts. *The Society of Thoracic Surgeons*, 66:155–161, 1998.

[4] E. Votta, F. Maisano, S. F. Bolling, O. Alfieri, F. M. Montevecchi, A. Redaelli. The Geoform Disease-Specific Annuloplasty System: A Finite Element Study. *Ann. Thorac. Surg.*, 84:92–101, 2007.

[5] E. Votta, F. Maisano, M. Soncini, A. Redaelli, F. M. Montevecchi, and O. Alfieri. 3-D computational analysis of the stress distribution on the leaflets after edge-to-edge repair of mitral regurgitation. *Journal of Heart Valve Disease*, 11:810–822, 2002.

[6] F. Dal Pan, G. Donzella, C. Fucci, and M. Schreiber. Structural effects of an innovative surgical technique to repair heart valve defects. *J. Biomech.*, 38:2460–2471, 2005.

[7] K. May-Newman and F. C. P. Yin. Biaxial mechanical behavior of excised porcine mitral valve. *J. Biomech. Eng.* 120, 38–47, 1995.

[8] K. May-Newman and F. C. P. Yin. A constitutive law for mitral valve tissue. *J. Biomech. Eng.*, 120:38–47, 1998.

[9] K. H. Lim, J. H. Yeo, C. M. Duran. Three-dimensional asymmetrical modeling of the mitral valve: a finite element study with dynamic boundaries. *J Heart Valve Dis.* 14:386392, 2005.

[10] N. Ranganathan, J. H. Lam, E. D. Wigle, M. D. Silver. Morphology of the human mitral valve: II. The valve leaflets. *Circ.*, 41:459–467, 1970.

[11] F. A. Flachskampf, S. Chandra, A. Gaddipatti, R. A. Levine, A. E. Weyman, W. Ameling, P. Hanrath, J. D. Thomas. Analysis of shape and motion of the mitral annulus in subjects with and without cardiomyopathy by echocardiographic 3-dimensional reconstruction. *J Am Soc Echocardiogr.* 13(4):277–87, 2000.

[12] S. R. Kaplan, G. Bashein, F. H. Sheehan, M. E. Legget, B. Munt, X. N. Li, M. Sivarajan, E. L. Bolson, M. Zeppa, R. W. Martin. Three-dimensional echocardiographic assessment of annular shape changes in the normal and regurgitant mitral valve. *American Heart Journal*, 139:378–87, 2000.

[13] T. A. Timek, D. T. Lai, P. Dagum, F. Tibayan, G. T. Daughters, D. Liang, G. J. Berry, D. C. Miller and N. B. Ingels. Ablation of mitral annular and leaflet muscle: effects on annular and leaflet dynamics. *Am. J. Physiol. Heart Circ. Physiol.* 285:1668–1674, 2003.

[14] Kunzelman KS, Cochran RP, Murphree SS, Ring WS, Verrier ED, Eberhart RC. Differential collagen distribution in the mitral valve and its influence on biomechanical behavior. *J. Heart Valve Dis.* 1993; **2**:236-244.

[15] J. H. Lam, N. Ranganathan, E. D. Wigle, M. D. Silver. Morphology of the human mitral valve: I. Chordae tendinae: a new classification. *Circ.*, 41:449–458, 1970.

[16] J. Ritchie, J. Jimenez, Z. He, M. S. Sacks, A. P. Yoganathan. The material properties of the native porcine mitral valve chordae tendineae: an in vitro investigation. *J. Biomech.*, 39(6):1129-35, 2006.

[17] J. H. Jimenez, D. D. Soerensen, Z. He, S. He, A. P. Yoganathan. Effects of a Saddle Shaped Annulus on Mitral Valve Function and Chordal Force Distribution: An In Vitro Study. *Annals of Biomedical Engineering*, 31:1171–1181, 2003.

[18] F. Rodriguez, F. Langer, K. B. Harrington, F. A. Tibayan, Ma. K. Zasio, A. Cheng, D. Liang, G. T. Daughters, J. W. Covell, J. C. Criscione, N. B. Ingels, D. C. Miller. Importance of mitral valve second-Order chordae for left ventricular geometry, wall thickening mechanics, and global systolic function *Cirulation*, 110(2):115–122, 2004.

[19] E. Messas, B. Pouzet, B. Touchot, J.L. Guerrero, G.J. Vlahakes, M. Desnos, P. Menasche, A. Hagege, R. A. Levine. Efficacy of Chordal Cutting to Relieve Chronic Persistent Ischemic Mitral Regurgitation. *Circulation*, 108:111–115, 2003.

[20] L. Sedrandsk, K. J. Grande-Allen, I. Vesely. Failure mechanics of mitral valve chordae tendinae. *Journal of Heart Valve Disease*, 11:644–650, 2002.

[21] J. B. Barlow. Perspectives on the Mitral Valve. Philadelphia : F.A. Davis, 1987

[22] M. O. Jensen, A. Fontaine, A. P. Yoganathan. Improved In Vitro Quantification of the Force Exerted by the Papillary Muscle on the Left Ventricular Wall Three Dimensional Force Vector Measurement System. *Annals of Biomedical Engineering*, 10:111–124, 2000.

[23] A. J. Sanfilippo, P. Harrigan, A. D. Popovic, A. E. Weyman, and R. A. Levine. Papillary muscle traction in mitral valve prolapse: quantitation by two-dimensional echocardiography. *J. Am. Coll. Cardiol.* 19:564–571, 1992

[24] P. Nordblom and O. Bech-Hanssen Reference values describing the normal mitral valve and the position of the papillary muscles. *Echocardiography*, 24(7):665–672, 2007.

[25] K. S. Kunzelman and R. P. Cochran. Mechanical Properties of Basal and Marginal Mitral Valve Chordinae. *Trans Am Soc Artif Intern Organs*, 36:405–408, 1990.

[26] K. O. Lim KO, D. R. Boughner. Mechanical properties of human mitral valve chordae tendinae: variation with size and strain rate. *Can J Physiol Pharmacol*, 53(3):330–339, 1975.

[27] J. Liao, I.Vesely. A structural basis for the size-related mechanical properties of mitral valve chordae tendinae. *Journal of Biomechanics*, 36(8):1125–33, 2003.

[28] Y. C. Fung, K. Fronek, and P. Patitucci. Pseudoelasticity of arteries and of its mathematical expression. *American Physiological Society*, 237:620:631, 1979.

[29] R. P. Cochran, K. S. Kunzelman, C. J. Chuong, M. S. Sacks and R. C. Eberhart. Nondestructive analysis of mitral valve collagen fiber orientation. *ASIAO Trans.*, 37(3):447–448, 1991

[30] D. R. Einstein, K. S. Kunzelman, P. G. Reinhall, M. A. Nicosia, R. P. Cochran. The relationship of normal and abnormal microstructural proliferation to the mitral valve closure sound. *Journal of Biomechanical Engineering*, 127:134–147, 2005.

[31] M. S. Sacks, Z. He, L. Baijens, S. Wanant, P. Shah, H. Sugimoto and A. P. Yoganathan. Surface Strains in the Anterior Leaflet of the Functioning Mitral Valve. *Annals of Biomedical Engineering*, 30:1281–1290, 2002.

[32] L. Chen, A. D. McCulloch and K. May-Newman. Nonhomogeneous deformation in the anterior leaflet of the mitral valve. *Annals of Biomedical Engineering*, 32:1599–1606, 2004.

[33] J. S. Grashow, M. S. Sacks, J. Liao, A. P. Yoganathan. Planar biaxial creep and stress relaxation of the mitral valve anterior leaflet. *Annals of biomedical engineering*, 34(10):1509–1518, 2006

[34] G. A. Holzapfel. *Nonlinear Solid Mechanics. A Continuum Approach for Engineering.* John Wiley & Sons, Chichester, 2000.

[35] T. Belytschko, W. K. Liu and B. Moran. *Nonlinear finite elements for continua and structures.* John Wiley & Sons, Chichester, 2000.

[36] A. J. M. Spencer. Constitutive theory for strongly anisotropic solids. In A. J. M. Spencer, editor, *Continuum Theory of the Mechanics of Fibre-Reinforced Composites*, pages 1–32. Springer-Verlag, Wien, 1984. CISM Courses and Lectures No. 282, International Centre for Mechanical Sciences.

[37] G. A. Holzapfel, G. Sommer, C. T. Gasser, and P. Regitnig. Determination of the layer-specific mechanical properties of human coronary arteries with non-atherosclerotic intimal thickening, and related constitutive modelling. *Am. J. Physiol. Heart Circ. Physiol.*, 289:H2048–2058, 2005.

[38] E. H. Sonnenblick, L. M. Napolitano, W. M. Daggett, and T. Cooper. An intrinsic neuromuscular basis for mitral valve motion in the dog. *Circ. Res.*, 21: 915, 1967.

[39] A. Jensen, U. Baandrup, J. Hasenkam, T. Kundu, C. Jørgensen. Distribution of the microelastic properties within the human anterior mitral leaflet. *Ultrasound in Medicine & Biology*, 2(12):1943–1948, 2006.

[40] M. M. Mehrabadi and S. Nemat-Nasser. Some basic kinematical relations for finite deformations of continua. *Mech. Mat.*, 6:127–138, 1987.

PAPER I

Transversely isotropic membrane shells with application to mitral valve mechanics. Constitutive modeling and finite element implementation.

V. Prot, B. Skallerud, G. A. Holzapfel

International Journal for Numerical Methods in Engineering 71(8):987–1008, 2007

Is not included due to copyright

PAPER II

Finite element analysis of the mitral apparatus: annulus shape effect and chordal force distribution.

V. Prot, R. Haaverstad, B. Skallerud

Biomechanics and Modeling in Mechanobiology. Accepted, 2007.

Finite element analysis of the mitral apparatus: annulus shape effect and chordal force distribution

V. Prot[1], R. Haaverstad[2,3], B. Skallerud[1]

[1]Department of Structural Engineering, Norwegian University of Science and Technology, N-7491 Trondheim, Norway
[2]Department of Cardiothoracic Surgery, St. Olav Hospital, N-7018 Trondheim, Norway
[3]The Medical Faculty, Norwegian University of Science and Technology, N-7030 Trondheim, Norway

ABSTRACT

This study presents a three-dimensional finite element model of the mitral apparatus using a hyperelastic transversely isotropic material model for the leaflets. The objectives of this study are to illustrate the effects of the annulus shape on the chordal force distribution and on the mitral valve response during systole, to investigate the role of the anterior secondary (strut) chordae and to study the influence of thickness of the leaflets on the leaflets stresses. Hence, analyses are conducted with a moving and fixed saddle shaped annulus and with and without anterior secondary chordae. We found that the tension in the secondary chordae represents 31% of the load carried by the papillary muscles. When removing the anterior secondary chordae, the tension in the primary anterior chordae is almost doubled, the displacement of the anterior leaflet toward the left atrium is also increased. The moving annulus configuration with an increasing annulus saddle height does not give significant changes in the chordal force distribution and in the leaflet stress compared to the fixed annulus. The results also show that the maximum principle stresses in the anterior leaflet are carried by the collagen fibers. The stresses calculated in the leaflets are very sensitive to the thickness employed.

keywords: mitral valve, chordal force, annulus shape, leaflet stresses, finite element analysis.

1 Introduction

The mitral valve is one of the four valves of the heart, separating the left atrium and the left ventricle. The mitral apparatus consists of an atrioventricular ring or annulus, two leaflets called anterior and posterior, chordae tendinae and two groups of papillary muscles. The

anterior leaflet is larger than the posterior leaflet. Both are attached to the mitral annulus and to the chordae tendinae, and the chordae tendinae are attached to the papillary muscles. These muscles are attached to the left ventricular wall. Located between the left atrium and the left ventricle, defects in the mitral apparatus have direct influence on the functionality of the left ventricle, and vice versa. A significant number of people are affected by impairment in both the mitral apparatus and the left ventricle either separately or combined. There is hence a need for a better understanding of the mitral apparatus in order to improve the treatment of mitral valve disease.

During systole the mitral apparatus prevent blood from flowing back into the atrium. Hence, it is of major importance in order to avoid regurgitation.

In order to assess pathologies, one first needs to understand the healthy heart and its tissues. Today the diagnostics obtained using ultrasound have matured to a level showing fine details of tissue motion and blood flow velocities *in vivo*. It is known that mechanical stress is of primary importance for change and development of the tissue. However, it is not possible to perform stress measurements *in vivo*. Recently, *in vitro* studies have been carried out on the mitral apparatus (see Saks et al. [24], Ritchie et al. [23], Limenez et al. [9] and Nielsen et al. [19]). These *in vitro* studies are able to predict the stress state of the chordae and the strain in the leaflets, but not the stress state of the leaflets. With a finite element model it is possible to estimate the stress state of the mitral apparatus. In case of valvular malfunction, surgical repair or replacement of some constituents of the mitral apparatus may be needed. A finite element model can be a tool to study numerically the effects of surgical procedures such as replacement, transection or transposition of chordae by simulating the anatomical changes resulting from surgery or ischemic mitral disease. This can potentially help surgeons to choose the best reconstructive technique. Modelling can also be used to study degenerative diseases affecting the tissues by modifying the material parameters of different parts of the mitral apparatus (Prot et al. [20]).

In order to predict the stress–strain behaviour of the mitral apparatus, one needs to establish proper material models. Previously, numerical simulations of the mitral apparatus have been conducted (see Kunzelman et al. [12], Votta et al. [30], Einstein et al. [4] and Dal Pan et al. [3]). In all these finite element studies the annulus was assumed flat and rigid and most employed simplified material models for chordae and leaflets. During the last decade, the material properties of the chordae tendinae and the mitral leaflets have been investigated. Kunzelman et al. [11], Liao et al. [14], and Ritchie et al. [23] have performed mechanical tests on different kinds of chordae and highlighted differences in the mechanical behaviour depending on size and type of mitral chordae. May–Newman and Yin [17] conducted biaxial testing for anterior and posterior porcine mitral leaflets.

The geometry of the valve also plays an important role in order to determine the stress state in the leaflets. The mitral annulus shape and its dynamic behaviour during the cardiac cycle have been studied in animals and humans using different imaging techniques such as two-dimensional and three-dimensional echocardiography, magnetic resonance etc (see, e.g., Salgo et al. [25], Tibayan et al. [29], Green et al. [6], Flachskampf et al. [5], Kaplan et al.[10]). Currently, the tendency is to describe the annulus shape as a saddle because of its resemblance to a nonplanar ellipse.

In the present work, an anisotropic material model is used for the valve leaflets based on the mechanical tests of porcine leaflets by May–Newman et al.[17]. The material model used for the

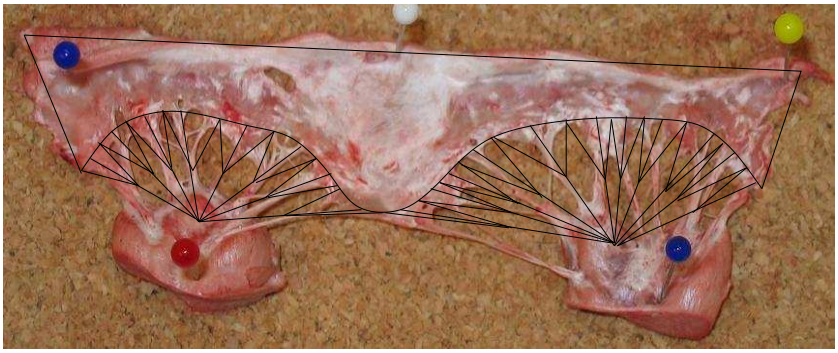

Figure 1: View of the porcine mitral valve (autopsy picture) and geometric modelling of the chordae and the leaflets

chordae tendinae is based on mechanical tests carried out on porcine chordae by Kunzelman and Cochran [11]. The analyses are based on a recent implementation of a transversely isotropic hyperelastic material model, using the user material interface `UMAT` in `ABAQUS` (Prot et al. [21]). Based on ultrasound measurements and autopsy of the mitral valve in a pig, we established the best possible three dimensional representation of the heart valve geometry for our model. The validity of the finite element model is checked against ultrasound measurements presented herein.
The key points of our study are as follow:
1) As the typical modelling of the annulus is to assume it as flat and rigid whereas we know it has a saddle shape and is non-rigid, the issue of moving or fixed saddle shaped annulus during systole is addressed.
2) The importance of the secondary (strut) chordae on mitral response is investigated by running simulations where they are cut.
3) From the autopsy it is observed that the thickness of the leaflets is inhomogeneous. Herein, we take a very simplistic approach and study the effect on leaflets stress when a homogeneous thickness of 1mm or 0.5mm is employed.
In all above cases, results concerning leaflet stresses, stretches, and chordae force distribution are presented.

2 Methods

2.1 Model geometry, boundary conditions and finite element mesh

In this study, the mitral valve geometry is based on three-dimensional echographic measurements carried out on a pig and on anatomical measurements (see Figure 1) carried out on the same pig post mortem (at St Olav University Hospital, Trondheim, Norway). The pig used for this study was a Noroc (hybrid of one quarter Duroc, one quarter Yorkshire and one quarter Norwegian landsvin) of 65 kg.
After the pig had been anaesthetized and intubated, the chest was opened. A 3D GE Vingmed ultrasound probe was positioned on the apex. A gel pad was positioned between the probe and the ventricular wall to avoid arrhythmia and improve the resolution of the ultrasound recording.

Three-dimensional echocardiography was performed from the apex. Compared to transthoracic echography this technique avoids perturbations due to bones and fat.

Annular reconstruction

The three-dimensional shape of the annulus was extracted from the ultrasound recordings with the commercial software Matlab at the beginning of systole and at peak systole. For these time frames, the annulus points were picked manually from the echocardiographic recording. These 3D points picked along the annulus were transformed into a Cartesian coordinate system with the z-axis aligned with depth-axis of the transducer, see Figure 2.

In the present study, the shape of the annulus was idealized as a symmetric non-planar ellipse.

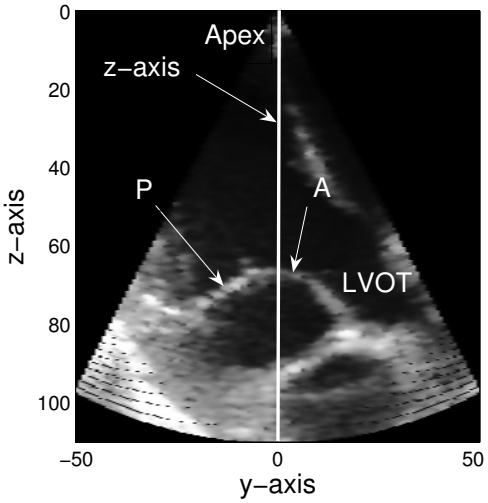

Figure 2: View of a plane of the 3D ultrasound recording. Anterior (A) and posterior (P) mitral valve leaflets and Left ventricular outflow tract (LVOT).

The elliptic shape of the annulus was obtained by fitting the ellipse to the x and y coordinates of the points selected along the annulus curve (see Figure 3). To obtain the non-planar shape a polynomial fitting (using the Matlab function polyfit) was carried out on the x an z coordinates of these points (see Figure 4). The annulus shape obtained at peak systole is shown in Figure 5. The dimensions of the idealized annulus are given in Table 1 for beginning and peak systole. The 3D annular perimeter was defined as the path length of the fitted annular curve. The interpeak distance was measured from the highest point of the anterior part of the annulus to the highest point on the opposite side of the annulus, i.e. the posterior part. The posterior part was almost planar during systole and assumed flat in our model. The saddle height was measured as the maximum distance between the anterior annulus and the plane defined the posterior annulus. The intervalley distance was measured between the two lowest points of the annulus, and these points correspond to the commissural part of the valve.

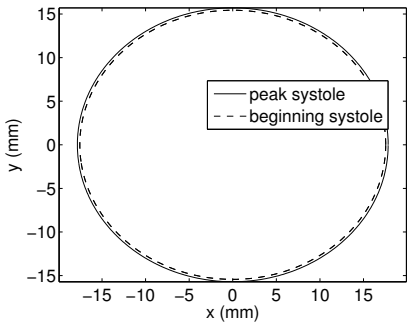

Figure 3: Planar elliptic shape at beginning of systole (dashed line) and at peak systole (solid line), calculated from 3D ultrasound measurements.

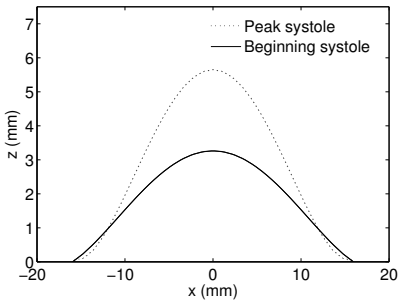

Figure 4: Polynomial fitting of the x and z coordinates for the anterior part of the mitral annulus at beginning of systole (solid line) and at peak systole (dashed line), calculated from 3D ultrasound measurements.

Table 1: Dimensions of the idealized annulus

	Saddle height (mm)	intervalley (mm)	interpeak (mm)	perimeter (mm)
beginning of systole	4.81	34.1	30.9	103.5
peak systole	6.85	35.6	31.4	108.5

Autopsy measurements

During the autopsy of the pig, the maximum distance from the annulus to the free edge of the anterior and posterior leaflets were measured to be 22 mm and 11 mm respectively, and the length of the annulus 105 mm. The annulus length value given by the autopsy agrees well with the one obtained from the 3D reconstruction of the annulus from the echocardiographic data. The anterior leaflet has a rounded convex free edge and has a larger area than the posterior leaflet. However, the posterior leaflet is narrow and has a longer attachment to the annulus. We assumed the posterior leaflet free edge to be divided in three scallops [7], a large middle one and two smaller ones representing the commissural parts of the valve.
Figure 1 shows that each papillary muscle is divided in several parts attached to each other. During ventricular contraction, these parts are much closer than shown on the figure (Barlow [1]). Hence, as a modelling simplification, the chordae attached to each of the papillary muscles were assumed to arise from the same point. In addition, the multiple insertions of the marginal

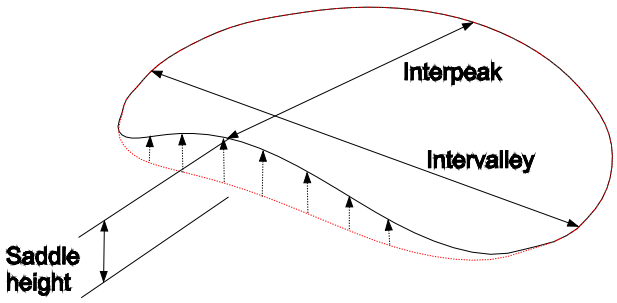

Figure 5: Three-dimensional shape of the annulus and displacements (arrows) of the anterior annulus during systole (calculated from 3D ultrasound measurements). Undeformed configuration dashed line (position at beginning of systole). Deformed configuration solid line (peak systole).

chordae to the free edge of the leaflets were modelled with branches arising from the middle point of the marginal chordae (Figure 1).
The lengths of the chordae were measured to be between 15 mm and 20 mm. During the autopsy of the pig two types of chordae were observed, the marginal chordae attached to the free edge of the leaflets and the secondary chordae attached beyond the free edge. The cross section areas of these chordae used in our model were based on the average values given by Liao et al. [14]: 0.38 mm^2 and 2.05 mm^2 for marginal and secondary chordae, respectively. The secondary chordae considered herein are also called "strut" chordae by Lam et al. [13] and are observed in 90% of human hearts and are by far the thickest and the largest chordae of the mitral valve. The morphology of the porcine mitral apparatus is close to the human mitral apparatus, hence the presence of these two secondary chordae corresponds to physiological conditions. In total, eight anterior marginal chordae, six posterior marginal chordae, six commissural chordae and two anterior secondary (strut) chordae were attached the leaflets.

Boundary conditions and mesh

The papillary muscles were assumed to be fixed. This assumption is quite consistent with the in vivo finding that the relative distance between the annulus and the papillary muscle tip is nearly constant during systole in normal subjects (Sanfilippo et al. [26]). The leaflets were allowed to rotate at the annular attachment. The chordae were attached at one end to the node representing the papillary muscle and at the other end to a node of the leaflets (a free edge node for the marginal and commissural chordae and a node beyond the free edge for the secondary chordae). A hard contact condition was set between the surfaces of the anterior and posterior leaflets in order to capture coaptation. A finite-sliding and a node to surface formulations were used for the computation of the quasi-static analyses (see ABAQUS analysis User's Manual).
Several analyses were conducted with a fixed annulus having the dimensions determined at the

beginning of systole and with a moving annulus. In the last case, since the main change in the annulus shape during systole appears to be the increase of the saddle height for the anterior annulus, displacement boundary conditions were prescribed to increase gradually the annulus saddle height from the value determined at the beginning of systole to the one determined at peak systole, see Table 1 and Figure 5. The ultrasound measurements showed that the posterior part of the annulus did not vary much in shape during systole. Hence, it was kept fixed.
In addition, for both annulus configurations analyses were run with and without secondary chordae to study their influence on the mitral valve response and on the chordal force distribution.
A uniform ventricular pressure was applied on the surface of the leaflets (see Figure 6). The

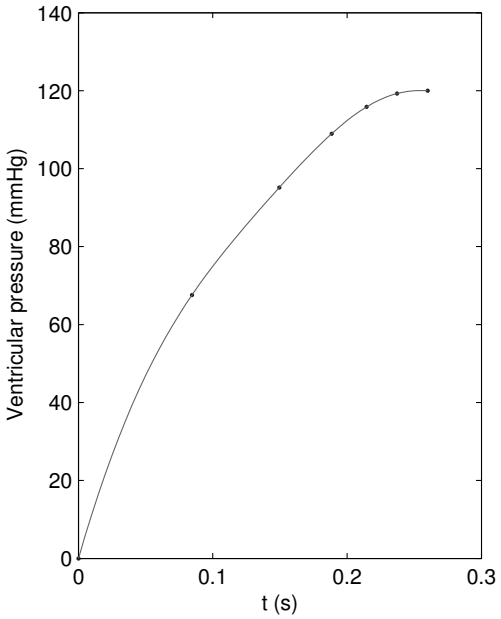

Figure 6: Left ventricular pressure applied on the ventricular surface of the leaflets from early to peak systole. A quasi-static solution was applied over this period.

peak systolic pressure in the left ventricle measured on the anaesthetized pig was 120 mmHg. Additionaly, the analyses were conducted with a pressure up to 200 mmHg to study the response at hypertension.
The valve leaflets were meshed with 1090 three noded membrane elements and the chordae with 81 truss elements, see Figure 7. Note that the figure corresponds to the initial (reference) configuration where the ventricular pressure is zero. Quasi–static conditions were employed in all simulations.

2.2 Material Model

Leaflets

Experimental data provided by May–Newman and Yin [17] show that the mitral leaflets tissue exhibits highly nonlinear mechanical response and that one approach to derive the material

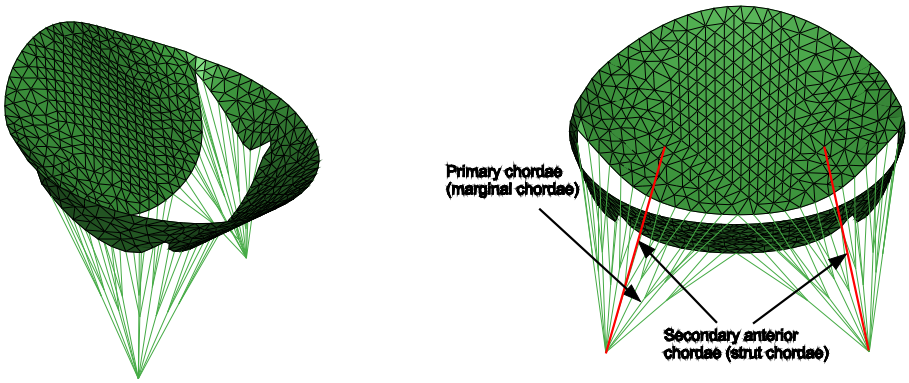

Figure 7: Finite element mesh and modelling of the initial configuration of the mitral apparatus.

constitutive model of the leaflets can be based on strain invariants and assumption of material incompressibility and transverse isotropy. The pseudo elastic response was simplified to be hyperelastic.

Here, we recall some continuum mechanics definitions used to derive these constitutive material models.

The deformation gradient is defined as $\mathbf{F} = \partial\mathbf{x}/\partial\mathbf{X}$ where $\mathbf{X}$ is the position of a point in the initial (undeformed) configuration related to a point $\mathbf{x}$ in the current (deformed) configuration. The right Cauchy-Green deformation tensor is denoted $\mathbf{C} = \mathbf{F}^T\mathbf{F}$.

The three invariants of $\mathbf{C}$ given by $I_1 = tr\ \mathbf{C}$, $I_2 = 1/2((tr\ \mathbf{C})^2 + tr\ \mathbf{C}^2)$ and $I_3 = det\ \mathbf{C}$ are related to isotropic hyperelasticity.

In order to describe transverse isotropy, the unit vector $\mathbf{a}_0$ defining the prefered average collagen fiber direction of the material is introduced. It is possible to define two pseudo-invariants I_4 and I_5 of $\mathbf{C}$ and $\mathbf{a}_o \otimes \mathbf{a}_0$ as $I_4 = \mathbf{a}_0 \cdot \mathbf{C}\mathbf{a}_0$ and $I_5 = \mathbf{a}_0 \cdot \mathbf{C}^2\mathbf{a}_0$. According to Spencer [28], the strain energy function of transversely isotropic hyperelasticity can be described by these five invariants.

The stress tensors are derived from a strain energy function Ψ:

$$\mathbf{S} = 2\frac{\partial\Psi}{\partial\mathbf{C}}, \quad \boldsymbol{\sigma} = J^{-1}\mathbf{F}\mathbf{S}\mathbf{F}^T, \tag{1}$$

where $\mathbf{S}$ and $\boldsymbol{\sigma}$ are the second Piola-Kirchhoff stress tensor and the Cauchy stress tensor, respectively.

The fourth-order material elasticity tensor is determined from:

$$\mathbb{C} = 4\frac{\partial^2\Psi}{\partial\mathbf{C}^2}. \tag{2}$$

The strain energy function employed herein to derive the constitutive model is the one proposed by Holzapfel et al. [8],

$$\Psi(I_1, I_4) = c_0[\exp^{c_1(I_1-3)^2+c_2(I_4-1)^2} - 1] + p(J-1), \tag{3}$$

where, c_i, $i = 0, 1, 2$, are material parameters, the scalar p serves as an indeterminate Lagrange multiplier and $J = det\mathbf{F}$ is the Jacobian of the deformation. The material parameters c_i,

$i = 0, 1, 2$ were fitted to biaxial *in vitro* tests on porcine mitral valve tissue carried out by May–Newman and Yin [17], using a nonlinear least square technique. Note that May–Newman and Yin [17] proposed the following strain energy function, $\Psi(I_1, I_4) = c_0[\exp^{c_1(I_1-3)^2+c_2\left(\sqrt{I_4}-1\right)^4} - 1]+p(J-1)$. The material model derived from this strain energy function was also implemented (Prot et al. [21]), but the model derived from (3) showed better numerical efficiency.
The anterior and posterior leaflets have different responses, the posterior one is more extensible than the anterior one. The material parameters of the strain energy function (3) are given in table 2 for both leaflets.
In the present model, the fibers are oriented parallel to the annulus (circumferential direction)

Table 2: Material parameter values for the strain-energy function (3)

	c_0(kPa)	c_1	c_2
Anterior leaflet	0.0520	4.63	22.6
Posterior leaflet	0.171	5.28	6.46

in the center of the anterior leaflet, with a gradual transition to an orthogonal orientation (radial direction) at the commissures (Cochran et al. [2]). May–Newman and Yin [16] found that the posterior leaflet was stiffer in the circumferential direction (parallel to the annulus) than in the radial direction. As the material model employed herein is based on their study the collagen fibers were oriented parallel to the annulus in the posterior leaflet. But, as shown subsequentely, this may not be an optimal collagen orientation. The local collagen direction is set by the material axes, i.e. the local collagen fiber orientation is aligned with the local 1-direction of the membrane elements, see Figure 6.8(a). The collagen fibers are embedded in the continuum. Their initial orientations are specified at the start of the analysis and then rotated according to the deformations of the valve leaflets.

Chordae

The chordae were modeled with an incompressible isotropic hyperelastic material. The nonlinear stress-stretch behaviour was implemented from experimental data published by Kunzelman and Cochran [11]. The same material model was used for all the chordae derived from the following strain energy function,

$$U(I_1) = a_1(\exp^{(a_2(I_1-1))} - 1), \tag{4}$$

$a_1 = 0.0565$ kPa and $a_2 = 29.6$ for the marginal chordae and $a_1 = 0.050$ kPa and $a_2 = 35$ for the secondary chordae (strut chordae).

3 Results

Leaflet stresses

The collagen fiber orientation and the maximum principal stress orientation are plotted in Figure 8 at a systolic pressure of 120mmHg. In the anterior leaflet, the fiber direction and the maximum principal stress direction are nearly aligned, this is not the case in the posterior

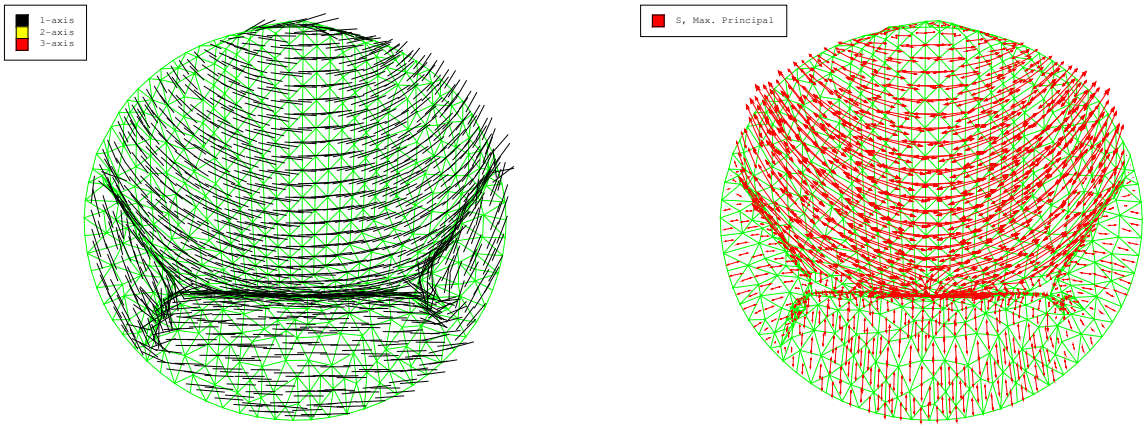

(a) Collagen fiber orientation (view from the left atrium)

(b) Maximum principal stress orientation (view from the left atrium)

Figure 8: (a) The collagen fiber orientation plotted at a systolic pressure of 120mmHg, (b) the maximal principal stress orientation in the leaflets plotted at a systolic pressure of 120mmHg (FE calculation).

leaflet where the principal stresses are nearly perpendicular the collagen fiber direction. This non-physiological result is addressed in the Discussion section. The directions of the highest maximum principal stresses flow from the fibrous trigones to the secondary chordae insertion zone. The stresses are higher in the anterior leaflet than in the posterior leaflet.
The Von Mises stresses are plotted on the valve leaflets at a systolic pressure of 120 mmHg in Figure 9 for two different leaflet thicknesses: 0.5 and 1 mm. The maximum Von Mises stresses were approximatively two times higher with a thickness of 0.5 mm than with a thickness of 1 mm.

Anterior leaflet stretches

In Figure 10 the principal stretches in a central region of interest of the anterior leaflet are plotted against the ventricular pressure, for different leaflet thicknesses: 0.5 and 1 mm. These results are compared to the maximum measured stretches from the *in vitro* study by Sacks et al. [24].

In this region, the collagen fibers are oriented parallel to the annulus (i.e. parallel to the circumferential direction), which means that the local 1-direction of the membrane surface is parallel to the annulus. The minor direction of the principal stretch (λ_1) was aligned parallel to the fibers and the major direction of the principal stretch (λ_2) was aligned perpendicularly to the fibers. As Sacks et al. [24], who measured the surface strains in *in vitro* tests on porcine mitral leaflets, we observe a rapid increase in the principal stretches during the closure of the valve and after the ventricular pressure reaches a value of 40 mmHg the principal stretches values are nearly constant. λ_2 was 1.19 times greater than λ_1 at a pressure of 120 mmHg. The value of λ_2 at a systolic pressure of 120 mmHg is very similar to the one obtained by Sacks et al. [24] but our model gives a somewhat stiffer behaviour along the fibers. The values obtained

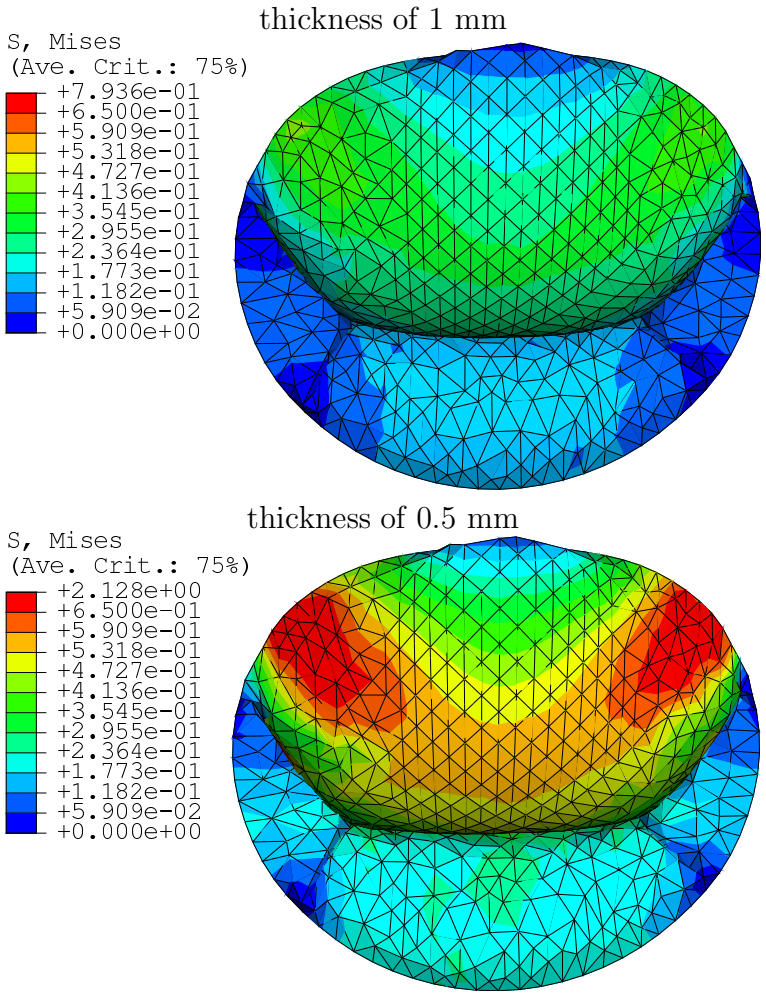

Figure 9: FE calculation of Von Mises stresses plotted at a systolic pressure of 120mmHg (MPa) for simulations using 0.5 and 1 mm for the thickness of the leaflets (without strut chordae).

at a pressure of 120 mmHg for the principal stretches using a leaflet thickness of 0.5 mm were 1.03 and 1.01 times greater than with a leaflet thickness of 1 mm in the directions parallel and perpendicular to the fiber, respectively. In addition, we observe that the coaptation of the leaflets occurs at 30 mmHg with the simulation using 0.5 mm for the thickness of the leaflet and at 40 mmHg with a thickness of 1 mm.

Chordae tensions and stretches

Analyses were carried out with a fixed saddle annulus and a moving saddle annulus, respectively. In both cases two analyses were performed, a first one with two secondary chordae attached on the anterior leaflet (healthy case) and a second one without secondary chordae (pathological case).
The forces carried by the different chordae at a systolic pressure of 120 mmHg are given in Table 3 for both annulus models, with and without secondary chordae.
The tensions reported in Table 3 are slightly higher in the anterior marginal chordae for the

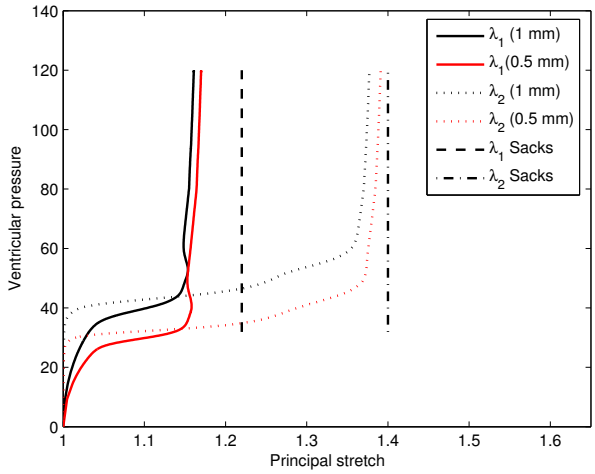

Figure 10: Principal stretches in the central region of the anterior leaflet for two different thicknesses obtained from FE calculation. The results are compared to the principal stretch values obtained experimentally by Sacks et al. [24] after the closure of the valve.

Table 3: Summary of chordae tendinae tension at a systolic pressure of 120 mmHg

		with secondary chordae				no secondary chordae			
		moving annulus		fixed annulus		moving annulus		fixed annulus	
chordae	number	F (N)	SD	F (N)	SD	F (N)	SD	F (N)	SD
anterior marginal	4	0.27	0.13	0.28	0.13	0.46	0.18	0.46	0.19
posterior marginal	3	0.40	0.069	0.40	0.069	0.43	0.084	0.42	0.056
commissural	3	0.19	0.056	0.19	0.056	0.19	0.056	0.19	0.083
anterior secondary chordae	1	1.3	–	1.3	–	–	–	–	–

fixed annulus, however the moving annulus and the fixed annulus does not induce any significant differences in force distribution in the chordae. Table 3 shows that the tension in the anterior marginal chordae is 1.7 times higher when the secondary chordae are removed. In addition, the tension in the secondary chordae is at least three times higher than in any other chordae.
The tensions in the different chordae obtained from the analyses are of the same magnitude as the ones obtained by Jimenez et al. [9] from experiments carried out *in vitro* on human mitral apparatus.
In Figures 11 and 12, the forces carried by the different groups of chordae and the corresponding papillary muscle are plotted against ventricular pressure for the simulations with and without secondary chordae, using a moving annulus.

At a systolic pressure of 120 mmHg the forces carried by the posterior marginal, anterior marginal and anterior secondary chordae are almost equal. However, when the anterior secondary chordae are removed the forces carried by the anterior marginal chordae group is multiplied by 1.64.
The percentages of the force carried by the different groups of chordae relative to the total pap-

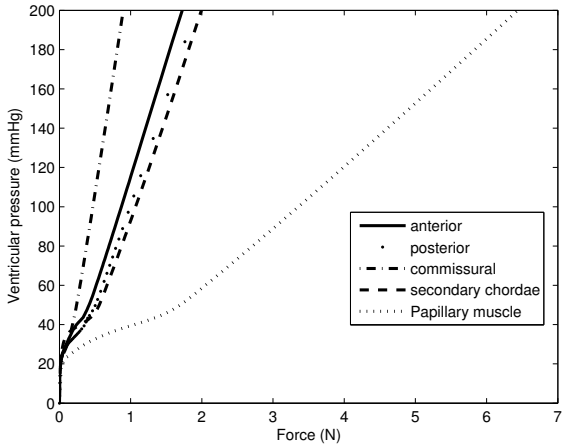

Figure 11: Forces carried by the different groups of chordae and the papillary muscle to which they are attached in the simulation using a moving annulus and secondary chordae (FE calculation)

Table 4: Distribution of the force carried by one papillary muscle among the different groups of chordae at a systolic pressure of 120 mmHg for the simulation using a flexible annulus, with and without secondary chordae.

chordae groups	with secondary chordae	no secondary chordae
anterior marginal	26%	50%
posterior marginal	29%	35%
commissural	14%	15%
anterior secondary chordae	31%	–

illary muscle force are given in Table 4. If we call $\mathbf{R}$ the force vector carried by the papillary muscle, $\mathbf{R}$ is equal to the sum of the vectors representing the tension in each chordae attached to this papillary muscle. Hence, if the force carried by one group of chordae is represented by the vector $\mathbf{T}$ the proportion of $\mathbf{R}$ carried by this group was calculated as,

$$\frac{||\mathbf{R}|| - ||\mathbf{R} - \mathbf{T}||}{||\mathbf{R}||}$$

When the secondary chordae are removed the proportion of the load carried by the group of anterior marginal chordae increases from 29% to 50%. The simulations with the secondary chordae shows an even distribution of the load between the anterior marginal, posterior marginal chordae groups and the secondary chordae.
Using the moving or the fixed annulus, the stretches in the chordae remained nearly unchanged and were equal to 1.05, 1.07, 1.04 and 1.05 at a systolic pressure of 120 mmHg, in the anterior marginal, posterior marginal, commissural and strut chordae, respectively.

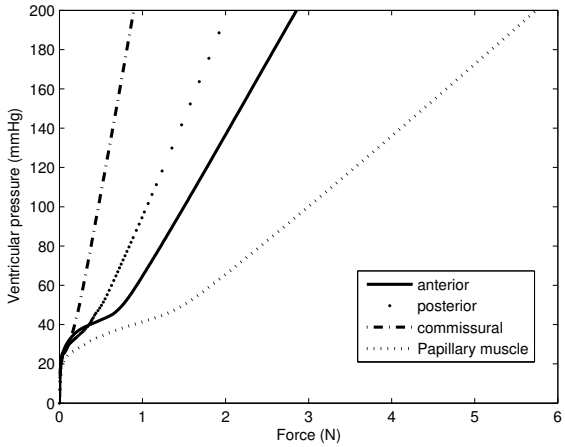

Figure 12: Forces carried by the different groups of chordae and the papillary muscle to which they are attached in the simulation using a moving annulus without secondary chordae (FE calculation)

Ultrasound comparison

In this section, the global finite element model response is compared with two-dimensional ultrasound measurements carried out on the pig. The relative displacement Δ_{rel} towards the interpeak line (see Figure 13) of a node located in the middle of the anterior leaflet is compared with the echographic measurements. The displacement of the node is compared to the 2D

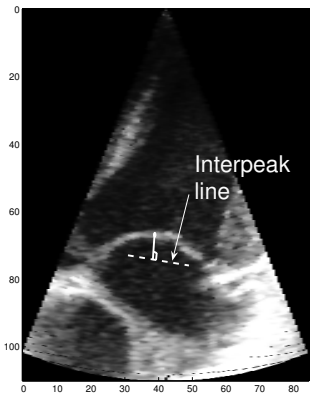

Figure 13: 2D ultrasound data. The dashed line represents the interpeak line between the two annulus points. The solid line is the measured relative displacement Δ_{rel} of the anterior mitral leaflet with respect to the annulus plane.

ultrasound measurements in Figure 14 for different configurations: fixed saddle shaped annulus with secondary chordae and moving saddle shaped annulus with secondary chordae. The configuration with the moving annulus shows the best agreement with the ultrasound data.

Δ_{rel} is given in Table 5 for the different configurations and the 2D ultrasound measurements

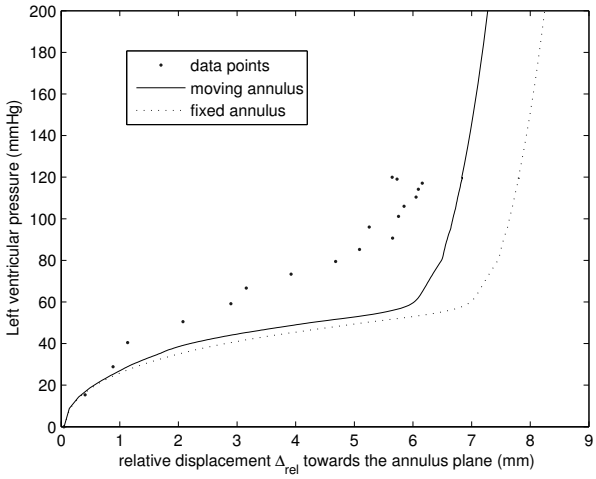

Figure 14: Comparison of the displacement towards the interpeak line of a node located in the middle of the anterior leaflet

Table 5: Summary of the relative displacement Δ_{rel} towards the interpeak line at a systolic pressure of 120 mmHg

	with secondary chordae		no secondary chordae		ultrasound
	moving annulus	fixed annulus	moving annulus	fixed annulus	
$\Delta_{rel}(mm)$	6.8	7.7	7.6	8.5	≈ 6

at a systolic pressure of 120 mmHg. With the moving annulus, Δ_{rel} is 0.8 mm larger when the secondary chordae are removed.

Hypertension

In this section, the results obtained with a systolic pressure of 200 mmHg are compared to those obtained at 120 mmHg (i.e. the ventricular pressure measured on the anaesthetizised pig). The tensions in the different groups of chordae are related in Table 6 for this pressure level.

The force carried by one papillary muscle at systolic pressure values of 120 mmHg and 200 mmHg for the flexible annulus configuration (with secondary chordae) was 3.97 N and 6.42 N, respec-

Table 6: Summary of chordae tendinae tension at a systolic pressure of 200 mmHg

		with secondary chordae				no secondary chordae			
		moving annulus		fixed annulus		moving annulus		fixed annulus	
chordae	number	F (N)	SD	F (N)	SD	F (N)	SD	F (N)	SD
anterior marginal	4	0.44	0.22	0.46	0.23	0.73	0.31	0.75	0.32
posterior marginal	3	0.64	0.11	0.64	0.11	0.69	0.14	0.69	0.14
commissural	3	0.30	0.093	0.30	0.095	0.30	0.094	0.30	0.094
anterior secondary chordae	1	2.0	–	2.0	–	–	–	–	–

tively. The relative displacement towards the interpeak line Δ_{rel} of the same node used in Figure 14 at systolic pressure values of 120 mmHg and 200 mmHg for the flexible annulus configuration (with secondary chordae) was 6.8 mm and 7.2 mm, respectively.

4 Discussion

A three–dimensional finite element model has been developed to assess the mitral valve response. A hyperelastic transversely isotropic material model was used to account for the different constituents and fiber direction in the mitral valve.

The results obtained for the chordal force distribution from our finite element analysis are in good agreement with the results of the in vitro study of Jimenez et al. [9]. This indicates that the branches adopted in the modelling of the chordae tendinae (see Figure 1) is a suitable choice.

The tension in a single secondary chordae is higher than the load carried by any of the other groups composed of three or four marginal chordae (see Figure 1) and represents 29% of the total load carried by the papillary muscle. This shows their importance in the structure of the mitral apparatus. This result is in agreement with the study conducted by Sedransk et al. [27] where anterior secondary chordae exhibit much higher failure load than the other types of chordae and may explain why the secondary chordae are larger than the marginal ones.

In table 4, we observe that when the secondary chordae are present, the load carried by the marginal anterior and posterior chordae groups are almost equal. The analyses in which anterior secondary chordae are removed show a significant increase of the tension in the anterior marginal chordae (see Table 3). Hence, cut or failure of the secondary chordae may lead to deterioration or even failure of other chordae remaining due to higher loading.

Contrary to the study conducted by Jimenez et al. [9], the flexible annulus configuration with an increasing annulus saddle height does not give significant changes in the chordal force distribution. However, Jimenez et al. [9] compared the results between two rigid annulus shape configurations having a saddle height difference of 9 mm while in the present work the saddle height is increased by 2 mm only. Mitral annulus saddle shape varies from species to species, but the anatomy of the porcine mitral valve is quite close to the human one. Thus the increase of 2 mm of the saddle height that was prescribed in this study between beginning of systole and peak systole is in good agreement with the results given by Kaplan et al. [10].

Our simulations show that the anterior secondary chordae reduce the motion of the anterior leaflet towards the left atrium. However, when they are removed, we find that the marginal chordae alone are sufficient to insure the proper closure of the valve and prevent mitral valve prolapse. In mitral valve surgery, the practical importance of this is the employment of multiple and strong artificial chordae attached to the free edge in treatment of anterior leaflet prolapse.

In Table 7, the Von Mises maximum stresses obtained with the flat and saddle configurations are compared to those obtained with existing finite element model at a similar pressure level (120 mmHg) and with similar geometries. The maximum Von Mises stresses obtained with the fixed saddle shape configurations show a quite good agreement with those obtained by Dal Pan et al. [3] with a hyperelastic isotropic model. A hyperelastic isotropic material model may be sufficient to determine the Mises equivalent stress level in the leaflets, but in order to determine principal stresses, the inclusion of the collagen fibers in the material model is important.

Table 7: Comparison of maximum Von Mises stress with other existing FEM models

Maximum Von Mises stress (MPa)		Systole (120 mmHg)	thickness (mm)
Moving annulus	anterior leaflet	0.386	1
	posterior leaflet	0.243	1
Fixed annulus	anterior leaflet	0.371	1
	posterior leaflet	0.243	1
hyperelastic isotropic model results			
Dal Pan et al. [3]	anterior leaflet	0.330	-
	posterior leaflet	0.252	-
linear-elastic model results			
Dal Pan et al. [3]	anterior leaflet	0.336	-
	posterior leaflet	0.225	-
Kunzelman et al.[12]	anterior leaflet	0.350	1.31
	posterior leaflet	0.200	1.26
Votta et al. [30]	anterior leaflet	0.396	0.8
	posterior leaflet	0.194	0.8

The stresses in posterior leaflet were found to be lower than in the anterior leaflet (Figure 9), as the posterior leaflet is smaller and carry less load. In the anterior leaflet, the maximum stresses were observed close to the fibrous trigones along the annulus. These areas are located where the annulus has the highest curvature. The study conducted by Salgo et al. [25] using a linear elastic material model for the leaflets and fixed boundary conditions for the annulus and the chordae showed that the leaflet stresses were reduced when the saddle height was increased. However, the present work does not give any significant differences in the anterior leaflet stresses when increasing the annulus saddle height in the physiological regime of the pig employed herein.

The directions of the maximum principal stresses in the anterior leaflet are nearly aligned with the collagen fiber orientation. This result shows that the maximum principal stresses are carried by the collagen fibers in the anterior leaflet. According to the results of May–Newman and Yin [16], the collagen fibers in the posterior leaflet are oriented parallel to the annulus in our model. In the posterior leaflet, the calculated maximum principal stress direction were nearly orthogonal to the collagen fibers. This does not seem physiological and it would be logic that the fibers will orient according to the maximum principal stress direction. Hence, an analysis with the collagen fibers orthogonal to the annulus in the posterior leaflet was performed and gave the same principal stress directions. Note that this latter collagen fiber orientation for the posterior leaflet did not affect the chordae load distribution. This may indicate that our collagen fiber orientation in the posterior leaflet shown in Figure 6.8(a), is not correct. This warrants further study.

The peak pressure in the left ventricle measured on the anaesthetized pig was 120 mmHg. Our simulations show that the stresses in the mitral apparatus increase significantly if the peak systolic pressure is increased. On the other hand, the global motions and the strains of the mitral apparatus are not very sensitive to the pressure level after complete closure of the valve. This is due to the typical soft tissue stress–strain exponential behavior of the its different constituents. Before closure the chordae and the leaflets are soft enough to allow proper coaptation of the mitral valve. After closure, the chordae tendinae and the leaflets become stiffer and prevent further deformations of the valve.

The thickness of the leaflets is also an important aspect in the modelling of the mitral apparatus. In the rough zone, the anterior leaflet is thicker, the width of this zone is about one third of the anterior leaflet length. However, the thickness of the leaflet can be much lower in the area with no chordal attachment. Our simulations show that the closure of the valve and the stress level in the leaflets strongly depends on thickness: the stresses are much greater and the closure of the valve happens at a lower pressure value with thinner leaflets. However, coaptation should occur for even lower pressure value. This deviation may be due to the starting position of the valve in our simulation. This delay in the closure of the valve was also observed with the finite element model using shell elements of Lim et al. [15]. In their study, the valve was still open during IVC (isovolumetric contraction) and achieved complete closure at the end of IVC, i.e. at approximatively 40 mmHg.
The present work agrees with Sacks et al. [24] in that the leaflets undergo large anisotropic stretches during closure. Although, the use of an isotropic material model for the leaflet may give a good prediction of the average stress level in the leaflets, our results shows that it is not appropriate for a study of principal strains and stresses.

5 Conclusion

The current analyses point out the importance of the anterior secondary chordae on the mitral systolic function manifested by the chordal force distribution and the apical displacement of the anterior leaflet.

The annulus flexibility introduced in this study, i.e. increase of the saddle height, does not seem to modify much the chordal force distribution or the stress distribution of the leaflets.

The stresses in the mitral apparatus appear to be sensitive to the pressure level during the whole systole whereas the deformations remain nearly constant after complete coaptation of the leaflets.

The stresses calculated in the leaflets are very sensitive to the thickness employed. This points out the importance of the evaluation of the thickness for the stress calculation in the leaflets.

6 Limitations

In the present work, the mitral valve was assumed to be symmetric and only the variation of the saddle height was prescribed as boundary conditions for the flexible annulus. According to Kaplan et al. [10], the annulus area, the interpeak distance and the intervalley distance decrease rapidly between beginning and mid–systole and at the same time the height of the saddle shape increases. The mitral valve function may depend on all these variations of the annular shape and area. In future studies, these changes of the annulus will be included as boundary conditions to get a better understanding of their influence on the mitral valve response and on the mitral apparatus stresses. Although the displacements of the papillary muscles may have an important role in the mitral valve dynamics, they were not accounted for in the present

model due to the difficulty to determine them from the ultrasound measurements.
More data on leaflet thickness and collagen fiber orientation (for the posterior leaflet in particular) are also needed in order to be more accurate in the modelling of the leaflets.
The material model used for the leaflets is based on mechanical data from the central region of the anterior and posterior leaflets. As no data currently exists for other regions of the leaflet, these experimental data were used to model the whole leaflets. This is most likely too simplistic and motivates for further tests of constitutive behaviour.
As membrane elements are used in this study, the stress distribution in the leaflets must be considered with care. The regions of high membrane stress are predicted. But, the use of solid elements to model the valve leaflets is more accurate in order to account for the variation of stress and deformation through the thickness, see Prot [22].
The present finite element model does not account for the effect of the fluid on the valve. However, the hemodynamics in the left ventricle and its interaction with the mitral valve is highly relevant in order to understand the global function of the heart. Hence, a fluid structure interaction model including the left ventricular wall is necessary to investigate the interaction between the mitral valve dynamics, the blood flow and the left ventricle.

ACKNOWLEDGEMENTS

The authors are grateful to the following persons for helpful discussions and assistance, associate professor Ivar Nordrum (Department of Laboratory Medicine, Children's and Women's Health, NTNU, Norway), MD Hans Henrik Dedichen (Department of circulation and medical imaging, NTNU, Norway), MD Håvard Bersås Nordgaard (Department of Cardiothoracic Surgery, St. Olav Hospital, Norway), professor Hans Torp (Department of circulation and medical imaging, NTNU, Norway), Dr. Lasse Løvstakken (Department of circulation and medical imaging, NTNU, Norway) and Mr. Bjarne Bergheim (Department of circulation and medical imaging, NTNU, Norway).

References

[1] Barlow JB (1987) Perspectives on the Mitral Valve. Philadelphia : F.A. Davis.

[2] Cochran RP, Kunzelman KS, Chuong CJ, Sacks MS, and Eberhart RC (1991) Nondestructive analysis of mitral valve collagen fiber orientation. ASIAO Trans. 37(3), 447–448

[3] Dal Pan F, Donzella G, Fucci C, and Schreiber M (2005) Structural effects of an innovative surgical technique to repair heart valve defects. J. Biomech. 38, 2460–2471

[4] Einstein DR, Kunzelman KS, Reinhal, P, Nicosia M, and Cochran RP (2004) Haemodynamic determinants of the mitral valve closure sound: a finite element study. Med. & Biol. Eng. & Comput. 42, 832–846

[5] Flachskampf FA, Chandra S, Gaddipatti A, Levine RA, Weyman AE, Ameling W, Hanrath P, Thomas JD (2000) Analysis of shape and motion of the mitral annulus in subjects with and without cardiomyopathy by echocardiographic 3-dimensional reconstruction. J Am Soc Echocardiogr. 13(4):277–87

[6] Green GR, Dagum P, Glasson JR, Daughters GT, Bolger AF, Foppiano LE, Berry GJ, Ingels NB Jr, Miller DC (1999) Mitral annular dilatation and papillary muscle dislocation without mitral regurgitation in sheep. Circulation 100, 95–102

[7] Ho SY (2002) Anatomy of the mitral valve. Heart 88, 5–10

[8] Holzapfel GA, Sommer G, Gasser CT, and Regitnig P (2005) Determination of the layer-specific mechanical properties of human coronary arteries with non-atherosclerotic intimal thickening, and related constitutive modelling. Am. J. Physiol. Heart Circ. Physiol. 289, H2048–2058

[9] Jimenez JH, Soerensen DD, He Z, He S, Yoganathan AP (2003) Effects of a Saddle Shaped Annulus on Mitral Valve Function and Chordal Force Distribution: An In Vitro Study. Annals of Biomedical Engineering 31, 1171–1181

[10] Kaplan SR, Bashein G, Sheehan FH, Legget ME, Munt B, Li X-N, Sivarajan M, Bolson EL, Zeppa M, Martin RW (2000) Three-dimensional echocardiographic assessment of annular shape changes in the normal and regurgitant mitral valve. American Heart Journal 139, 378–87

[11] Kunzelman KS and Cochran RP (1990) Mechanical properties of basal and marginal mitral valve chordae tendineae. ASAIO Trans. 36, M405–408

[12] Kunzelman KS, Cochran RP, Chuong C, Ring WS, Verrier, E D, and Eberhart, R D (1993) Finite element analysis of the mitral valve. J. Heart Valve Dis. 2, 326–340

[13] Lam JH, Ranganathan N, Wigle ED, Silver MD (1970) Morphology of the human mitral valve: I. Chordae tendinae: a new classification. Circ. 41 , 449–458

[14] Liao J, Vesely I (2003) A structural basis for the size-related mechanical properties of mitral valve chordae tendineae. J. Biomech. 36(8), 1125–33

[15] Lim KH, Yeo JH, Duran CM (2005) Three-dimensional asymmetrical modeling of the mitral valve: a finite element study with dynamic boundaries. J Heart Valve Dis. 14:386392

[16] May-Newman K and Yin FCP (1995) Biaxial mechanical behavior of excised porcine mitral valve. J. Biomech. Eng. 120, 38–47

[17] May-Newman K and Yin FCP (1998) A constitutive law for mitral valve tissue. Am. J. Physiol. 269, 1319–1327

[18] Messas E, Pouzet B, Touchot B, Guerrero JL, Vlahakes GJ, Desnos M, Menasche P, Hagege A, Levine RA (2003) Efficacy of Chordal Cutting to Relieve Chronic Persistent Ischemic Mitral Regurgitation. Circulation 108, 111–115

[19] Nielsen SL, Nygaard H, Fontaine AA, Hasenkam JM, He S, Andersen NT, Yoganathan AP (1999) Chordal force distribution determines systolic mitral leaflet configuration and severity of functional mitral regurgitation - design of a new surgical approach for ventricular remodeling to relieve ischemic mitral regurgitation. Journal of the American College of Cardiology 33, 843–853

[20] Prot V, Skallerud B, Holzapfel GA (2007) Effects of connective tissue pathologies on mitral valve response. MHM 2007, Modelling of heterogeneous materials with applications in construction and biomedical engineering, Prague 106-107

[21] Prot V, Skallerud B, Holzapfel GA (2007) Transversely isotropic membrane shells with application to mitral valve mechanics. Constitutive modeling and finite element implementation. International Journal for Numerical Methods in Engineering 71(8), 987–1008

[22] Prot V (2008) Numerical modelling of the mitral apparatus (PhD thesis). Trondheim, Norway. Norwegian University of Science and Technology

[23] Ritchie J, Jimenez J, He Z, Sacks MS, Yoganathan AP (2006) The material properties of the native porcine mitral valve chordae tendineae: an in vitro investigation. J. Biomech. 39(6), 1129-35

[24] Sacks MS, He Z, Baijens L, Wanant S, Shah P, Sugimoto H and Yoganathan AP (2002) Surface Strains in the Anterior Leaflet of the Functioning Mitral Valve. Annals of Biomedical Engineering 30, 1281–1290

[25] Salgo IS, Gorman JH, Gorman RC, Jackson BM, Bowen FW, Plappert T, St John Sutton MG, Edmunds LH Jr (2002) Effect of annular shape on leaflet curvature in reducing mitral leaflet stress. Circulation 106(6), 711–7

[26] Sanfilippo AJ, Harrigan P, Popovic AD, Weyman AE, and Levine RA (1992) Papillary muscle traction in mitral valve prolapse: quantitation by two-dimensional echocardiography. J. Am. Coll. Cardiol. 19, 564-571

[27] Sedrandsk L, Grande-Allen KJ, Vesely I (2002) Failure mechanics of mitral valve chordae tendinae. Journal of Heart Valve Disease 11, 644–650

[28] Spencer AJM (1984) Constitutive theory for strongly anisotropic solids. In A. J. M. Spencer, editor, Continuum Theory of the Mechanics of Fibre-Reinforced Composites, pages 1–32. Springer-Verlag, Wien. CISM Courses and Lectures No. 282, International Centre for Mechanical Sciences

[29] Tibayan FA, Rodriguez F, Zasio MK, Bailey L, Liang D, Daughters GT, Langer F, Ingels NB Jr, Miller DC (2003) Geometric Distortions of the Mitral Valvular-Ventricular Complex in Chronic Ischemic Mitral Regurgitation. *Circulation* 108, 116–121

[30] Votta E, Maisano F, Soncini M, Redaelli A, Montevecchi FM and Alfieri, O (2002) 3-D computational analysis of the stress distribution on the leaflets after edge-to-edge repair of mitral regurgitation. J. Heart Valve Dis. 11, 810–822

PAPER III

Nonlinear solid finite element analysis of mitral valves with heterogeneous leaflet layers

V. Prot, B. Skallerud

Computational Mechanics. Accepted, 2008

Nonlinear solid finite element analysis of mitral valves with heterogeneous leaflet layers

V. Prot[1], B. Skallerud[1]

[1]Department of Structural Engineering, Norwegian University of Science and Technology, N-7491 Trondheim, Norway

ABSTRACT

The present work addresses an incompressible transversely isotropic hyperelastic material used in three–dimensional solid finite element analysis of a porcine mitral valve to investigate the influence of its layered structure on stress distributions and global responses. The material model implementation is described and checked in single element tests and compared with a membrane implementation in an out–of–plane loading test to study how the layered structures modify the stress response for a simple geometry. Three different collagen layer arrangements are used in finite element analysis of the mitral valve. When the leaflets are arranged in two layers with the collagen on the ventricular side, the stress in the fibre direction through the thickness in the central part of the anterior leaflet is homogenized and the peak stress is reduced. A simulation using membrane elements is also carried out for comparison with the solid finite element results. Compared to echocardiographic measurements, the membrane and solid finite element models bulge too much in the left atrium. This may be due to evidence of active muscle fibres in some parts of the anterior leaflet, whereas our constitutive modelling is based on passive material.

Keywords: mitral valve, solid element, hyperelasticity, transverse isotropy, incompressibility, collagen fibre arrangement.

1 Introduction

The mitral valve is a thin walled complex connective tissue structure located between the left atrium and left ventricle of the heart, preventing the blood from flowing back into the atrium when the ventricle contracts. The mitral apparatus consists of two leaflets (anterior and posterior) attached to the annulus and the chordae tendinae. The chordae are further attached to the papillary muscles. Hence, the structural system has some resemblance with a parachute.

Previously, several numerical simulations of the mitral apparatus using membrane shell elements have been conducted with different types of material models for the leaflets (see, e.g., Kunzelman et al. [1], Einstein et al. [2], Votta et al. [3], Dal Pan et al. [4], Lim et al. [5], Prot et al. [6]). These simulations considered the leaflets to be homogeneous over thickness, and by definition, the collagen fibres are smeared out over the thickness and accounted for in an average sense. However, according to previous studies (Kunzelman et al. [7], Grande-Allen et al. [8], Jensen et al. [9]) the mitral leaflets can be considered as three–layered laminated structures: the atrialis on the atrium side, the ventricularis on the ventricular side and the inner fibrosa layer, with each layer having different mechanical properties.

The fibrosa is the thickest layer and composed of dense collagen. The atrialis is composed of loose connective tissue, the ventricularis is composed mostly of elastin and is the thinnest layer. The thicknesses of these layers are different for each leaflet and vary from the annulus attachment to the free edge, [1]. With the membrane approach these finer structural details are not accounted for.

Kunzelman et al. [1] examined the layer arrangement with a beam in bending with different elastic properties for each layer. Their analysis suggests that this layered structure may decrease the leaflet bending resistance. The present study employs a three dimensional finite element model of the mitral apparatus in order to take into account different material properties for each layer, using solid elements. Even though these elements are computationally more expensive than shell elements, the use of three–dimensional solid elements is probably the most accurate approach for finite element analysis of the mitral valve. Furthermore, using several brick elements through the thickness of the leaflets allows the assignment of different material properties to the different layers. However, this is easy in theory, but very challenging in practice due to scarce data on the different material properties of each layer. Our working hypothesis is that the optimal load carrying of the leaflets is mainly achieved by means of membrane stresses, and that stresses are minimized. This has an analogy in mechanics of arteries, where Kuhl and Holzapfel [10] have shown that the collagen distributions through the different layers of the blood vessel arrange themselves such that the stress peaks through the thickness are reduced. Note that for the aortic valve a bending stiffness is present, since these leaflets have no chordae that can assist in load carrying of the valve. So a question for the layered modeling of mitral leaflets is: how should the collagen be distributed through the layers in order to get an optimal stress state over the thickness? If an answer to this can be found, one has the possibility to account for detailed stress distribution in the different leaflet constituents, and use this to get better understanding of how connective tissue diseases evolve and how the body tries to adjust to this by means of re-modeling and adaptation [11].

May-Newman and Yin [12] described the anisotropic nonlinear mechanical behavior of porcine mitral leaflets and showed that the constitutive material model can be derived under the assumption of material incompressibility and transverse isotropy using the framework of hyperelasticity. Earlier studies have presented general anisotropic hyperelasticity formulations including incompressibility. Weiss et al. [13] derived the general expressions for analysis of ligaments and tendons. Rüter and Stein [14] employed their formulation in simulation of fibre reinforced rubber. Holzapfel et al. [15] employed a model for arteries. Our models and formulations are based on some of the results given in these references. However, in particularization of the model some differences result. In this work we develop a transversely isotropic hyperelastic material model for solid elements based on the model described by Prot et al. [16] for the

mitral leaflets. Note that in [16] membrane elements were employed, and incompressibility was explicitly accounted for using the plane stress condition as in [17]. Herein, we use an uncoupled form for the strain energy function. The constitutive equations for isotropic hyperelasticity from an uncoupled strain energy function were first derived by Simo et al. [18].
The present work is organized as follows. In Section 2 we present the constitutive equations of a transversely isotropic hyperelastic material model for solid elements using a penalty method to treat incompressibility. In section 3 single element simulations are presented in order to validate the stress update of the implementation of the material model and a numerical example is analysed to compare the response obtained with solid elements and membrane-shell elements (see, e.g., Prot et al [16]). Then, finite element analyses of the mitral valve are conducted in order to investigate the influence of the collagen structure on the mitral valve response and particularly on the resistance of leaflets to bending. To the best of our knowledge, nonlinear analysis of the mitral valve using solid element has not been presented before. The global response from simulations is compared to corresponding ultrasound recordings. The comparison illustrates some shortcomings of the simulations. We conclude the paper with a discussion on limitations in our modelling and give some crucial points that need further studies.

2 Continuum mechanical framework

In this section we briefly introduce the continuum mechanical framework. The purpose of this section is to provide the derivation of the stress and the tensors in order to use the transversely isotropic hyperelastic constitutive model with solid finite elements. Further details can be found in [19].

2.1 Kinematics

Let Ω_0 and Ω be the reference and current configurations, respectively. The deformation map $\boldsymbol{\varphi}(\mathbf{X}) : \Omega_0 \rightarrow \mathbf{R}^3$ transforms a material point $\mathbf{X} \in \Omega_0$ into the related current position $\mathbf{x} = \boldsymbol{\varphi}(\mathbf{X}) \in \Omega$. Hence, the deformation gradient $\mathbf{F}$ is defined as $\mathbf{F} = \partial\boldsymbol{\varphi}(\mathbf{X})/\partial\mathbf{X} = \partial\mathbf{x}/\partial\mathbf{X}$, with the volume ratio $J = \det\mathbf{F} > 0$ ($J = 1$ for an incompressible material).
We consider the multiplicative decomposition of the deformation gradient $\mathbf{F}$, first introduced by Flory [20]:

$$\mathbf{F} = (J^{1/3}\mathbf{1})\bar{\mathbf{F}} \tag{1}$$

$$\mathbf{C} = (J^{2/3}\mathbf{1})\bar{\mathbf{C}} \tag{2}$$

The terms $J^{1/3}$ and $J^{2/3}$ are associated with volume changing deformation. $\bar{\mathbf{F}}$ and $\bar{\mathbf{C}} = \bar{\mathbf{F}}^T\bar{\mathbf{F}}$, which are called modified deformation gradient and modified right Cauchy-Green tensor, are associated with the volume preserving deformations of the material:

$$\det(\bar{\mathbf{F}}) = 1 \quad \text{and} \quad \det(\bar{\mathbf{C}}) = \det(\bar{\mathbf{F}})^2 = 1. \tag{3}$$

The modified left Cauchy-Green tensor then reads $\bar{\mathbf{B}} = \bar{\mathbf{F}}\bar{\mathbf{F}}^T$.
We assume that the only anisotropic property arises from a fibre family embedded in the continuum and that the direction of the fibre at point $\mathbf{X}$ in the reference configuration Ω_0 is

defined by a unit vector $\mathbf{a_0}(\mathbf{X})$. During deformation this fibre moves with the material points of the continuum body and arrives at the deformed configuration Ω. Hence, the new fibre direction at the associated point $\mathbf{x}$ in Ω is defined by a vector $\mathbf{a} = \mathbf{F}\mathbf{a}_0$, and the stretch of the fibre in this direction is $|\mathbf{a}|$. For further use, we define the following vector:

$$\bar{\mathbf{a}} = \bar{\mathbf{F}}\mathbf{a}_0, \tag{4}$$

which corresponds to the push-forward of $\mathbf{a}_0$ via the part of the deformation gradient associated with the volume preserving deformations.

2.2 Strain energy function

In order to describe the anisotropic hyperelastic response of the mitral valve leaflets, we use the standard strain energy function Ψ for transversely isotropic materials:

$$\Psi = \Psi(\mathbf{C}, \mathbf{a}_0 \otimes \mathbf{a}_0), \tag{5}$$

and adopt the following decomposition of Ψ into two parts [15],

$$\Psi(\mathbf{C}, \mathbf{a}_0 \otimes \mathbf{a}_0) = U(J) + \bar{\Psi}(\bar{\mathbf{C}}, \mathbf{a}_0 \otimes \mathbf{a}_0), \tag{6}$$

where U and $\bar{\Psi}$ are the volumetric and isochoric contributions of Ψ, respectively. For the particular case of mitral valve leaflets, we assume finally that the energy function may be expressed in terms of three invariants:

$$\Psi(\mathbf{C}, \mathbf{a}_0 \otimes \mathbf{a}_0) = U(J) + \bar{\Psi}(\bar{I}_1, \bar{I}_4), \tag{7}$$

where $\bar{I}_1 = \mathrm{tr}\bar{\mathbf{C}} = \mathrm{tr}\bar{\mathbf{B}}$ and $\bar{I}_4 = \bar{\mathbf{C}} : \mathbf{a}_0 \otimes \mathbf{a}_0$.
Note that:

$$I_1 = J^{2/3}\bar{I}_1, \quad I_4 = J^{2/3}\bar{I}_4, \quad \bar{I}_4 = tr(\bar{\mathbf{a}} \otimes \bar{\mathbf{a}}). \tag{8}$$

We employ the following form for the polyconvex [21], [22] strain energy function Ψ, [16], [15]:

$$\Psi(\bar{I}_1, \bar{I}_4, J) = \underbrace{c_0\left(e^{c_1(\bar{I}_1-3)^2+c_2(\bar{I}_4-1)^2} - 1\right)}_{\bar{\Psi}(\bar{I}_1,\bar{I}_4)\text{: isochoric part}} + \underbrace{\frac{1}{2}\kappa(J-1)^2}_{U(J)\text{: volumetric part}}, \tag{9}$$

where c_0, c_1, c_2 are material parameters, κ is a positive penalty parameter and $(J-1)^2$ is known as the penalty function. The idea is to approximate the material as slightly compressible by using a large value of κ.

2.3 Stress and elasticity tensors

Stress tensors

The second Piola-Kirchhoff stress tensor $\mathbf{S}$ is derived from eq.(7):

$$\mathbf{S} = 2\frac{\partial \Psi}{\partial \mathbf{C}} = \underbrace{2\frac{\partial U}{\partial \mathbf{C}}}_{\mathbf{S}_{vol}} + \underbrace{2\frac{\partial \bar{\Psi}}{\partial \mathbf{C}}}_{\mathbf{S}_{iso}} \tag{10}$$

$$\mathbf{S}_{vol} = \kappa(J^2 - J)\mathbf{C}^{-1} \tag{11}$$

$$\mathbf{S}_{iso} = 2\frac{\partial \bar{\mathbf{C}}}{\partial \mathbf{C}} : \frac{\partial \overline{\Psi}(\bar{I}_1, \bar{I}_4)}{\partial \bar{\mathbf{C}}} \tag{12}$$

$$= \frac{\partial \bar{\mathbf{C}}}{\partial \mathbf{C}} : (2\psi_1 \mathbf{1} + 2\psi_4 \mathbf{a}_0 \otimes \mathbf{a}_0), \quad \text{where} \quad \psi_i = \frac{\partial \bar{\Psi}}{\partial \bar{I}_i}, i = 1, 4 \tag{13}$$

$$= J^{-2/3}\Big(\mathbb{I} - \frac{1}{3}\mathbf{C}^{-1} \otimes \mathbf{C}\Big) : \bar{\mathbf{S}} \quad \text{with} \quad \bar{\mathbf{S}} = 2\psi_1 \mathbf{1} + 2\psi_4 \mathbf{a}_0 \otimes \mathbf{a}_0 \tag{14}$$

$$= J^{-2/3}\left(\overline{\mathbf{S}} - \frac{1}{3}(2\psi_1 \overline{I}_1 + 2\psi_4 \overline{I}_4)\overline{\mathbf{C}}^{-1}\right), \quad \text{with} \quad \mathbf{C}^{-1} \otimes \mathbf{C} = \bar{\mathbf{C}}^{-1} \otimes \bar{\mathbf{C}}. \tag{15}$$

using the following results,

$$\frac{\partial \bar{\mathbf{C}}}{\partial \mathbf{C}} = J^{-2/3}\Big(\mathbb{I} - \frac{1}{3}\mathbf{C} \otimes \mathbf{C}^{-1}\Big) \quad \text{and} \quad \frac{\partial J}{\partial \mathbf{C}} = \frac{1}{2}J\mathbf{C}^{-1}, \tag{16}$$

where $\mathbb{I}$ denotes the fourth order identity tensor, and reads in index notation:

$$(\mathbb{I})_{ijkl} = \frac{1}{2}(\delta_{ik}\delta_{jl} + \delta_{il}\delta_{jk}) \tag{17}$$

The Cauchy stress tensor $\boldsymbol{\sigma}$ is obtained by the push-forward operation of $\mathbf{S}$ to the current configuration, $\boldsymbol{\sigma} = \frac{1}{J}\mathbf{F}\mathbf{S}\mathbf{F}^T$. Thus,

$$\boldsymbol{\sigma} = \kappa(J-1)\mathbf{1} + \frac{1}{J}\mathrm{dev}\bar{\boldsymbol{\sigma}}, \quad \bar{\boldsymbol{\sigma}} = 2\psi_1 \bar{\mathbf{B}} + 2\psi_4 \bar{\mathbf{a}} \otimes \bar{\mathbf{a}}, \tag{18}$$

$$\mathrm{dev}[\cdot] = (\mathbb{I} - \frac{1}{3}\mathbf{1} \otimes \mathbf{1}) : (\cdot).$$

Elasticity tensors

The material elasticity tensor obtained from eq.(7) reads:

$$\mathbb{C} = 4\frac{\partial^2 \Psi}{\partial \mathbf{C} \partial \mathbf{C}} = \underbrace{4\frac{\partial^2 U}{\partial \mathbf{C} \partial \mathbf{C}}}_{\mathbb{C}_{vol}} + \underbrace{4\frac{\partial^2 \bar{\Psi}}{\partial \mathbf{C} \partial \mathbf{C}}}_{\mathbb{C}_{iso}}. \tag{19}$$

We adopt the following notation:

$$\psi_{ij} = \frac{\partial^2 \Psi}{\partial \bar{I}_i \partial \bar{I}_j}, \quad i, j = 1, 4 \tag{20}$$

Hence,

$$\mathbb{C}_{vol} = 2\kappa(J^2-J)\frac{\partial \mathbf{C}^{-1}}{\partial \mathbf{C}} + 2\kappa(J^2-\frac{J}{2})\mathbf{C}^{-1}\otimes\mathbf{C}^{-1}, \tag{21}$$

$$\begin{aligned}\mathbb{C}_{iso} &= 4\psi_{11}\frac{\partial \bar{I}_1}{\partial \mathbf{C}}\otimes\frac{\partial \bar{I}_1}{\partial \mathbf{C}} + 4\psi_{14}\left(\frac{\partial \bar{I}_1}{\partial \mathbf{C}}\otimes\frac{\partial \bar{I}_4}{\partial \mathbf{C}} + \frac{\partial \bar{I}_4}{\partial \mathbf{C}}\otimes\frac{\partial \bar{I}_1}{\partial \mathbf{C}}\right) + 4\psi_{44}\frac{\partial \bar{I}_4}{\partial \mathbf{C}}\otimes\frac{\partial \bar{I}_4}{\partial \mathbf{C}} \\ &\quad +4\psi_1\frac{\partial^2 \bar{I}_1}{\partial \mathbf{C}\partial \mathbf{C}} + 4\psi_4\frac{\partial^2 \bar{I}_4}{\partial \mathbf{C}\partial \mathbf{C}},\end{aligned} \tag{22}$$

$$\begin{aligned}\mathbb{C}_{iso} &= 4\psi_{11}\frac{\partial \bar{I}_1}{\partial \mathbf{C}}\otimes\frac{\partial \bar{I}_1}{\partial \mathbf{C}} + 4\psi_{14}\left(\frac{\partial \bar{I}_1}{\partial \mathbf{C}}\otimes\frac{\partial \bar{I}_4}{\partial \mathbf{C}} + \frac{\partial \bar{I}_4}{\partial \mathbf{C}}\otimes\frac{\partial \bar{I}_1}{\partial \mathbf{C}}\right) + 4\psi_{44}\frac{\partial \bar{I}_4}{\partial \mathbf{C}}\otimes\frac{\partial \bar{I}_4}{\partial \mathbf{C}} \\ &\quad -\frac{2}{3}J^{-2/3}\left(\mathbf{C}^{-1}\otimes\bar{\mathbf{S}} + \bar{\mathbf{S}}\otimes\mathbf{C}^{-1}\right) + \frac{2}{9}\mathrm{tr}(\bar{\mathbf{F}}\bar{\mathbf{S}}\bar{\mathbf{F}}^T)\mathbf{C}^{-1}\otimes\mathbf{C}^{-1} - \frac{2}{3}\mathrm{tr}(\bar{\mathbf{F}}\bar{\mathbf{S}}\bar{\mathbf{F}}^T)\frac{\partial \mathbf{C}^{-1}}{\partial \mathbf{C}}.\end{aligned} \tag{23}$$

Further details are obtained by introducing:

$$\frac{\partial \bar{I}_1}{\partial \mathbf{C}} = J^{-2/3}\left(\mathbf{1} - \frac{1}{3}\bar{I}_1\bar{\mathbf{C}}^{-1}\right), \tag{24}$$

$$\frac{\partial \bar{I}_4}{\partial \mathbf{C}} = J^{-2/3}\left(\mathbf{a}_0\otimes\mathbf{a}_0 - \frac{1}{3}\bar{I}_4\bar{\mathbf{C}}^{-1}\right), \tag{25}$$

$$\frac{\partial^2 \bar{I}_1}{\partial \mathbf{C}\partial \mathbf{C}} = -\frac{1}{3}J^{-2/3}\left(\mathbf{C}^{-1}\otimes\mathbf{1} + \mathbf{1}\otimes\mathbf{C}^{-1}\right) + \frac{1}{9}\bar{I}_1\mathbf{C}^{-1}\otimes\mathbf{C}^{-1} - \frac{1}{3}\bar{I}_1\frac{\partial \mathbf{C}^{-1}}{\partial \mathbf{C}}, \tag{26}$$

$$\frac{\partial^2 \bar{I}_4}{\partial \mathbf{C}\partial \mathbf{C}} = -\frac{1}{3}J^{-2/3}\left(\mathbf{C}^{-1}\otimes\mathbf{a}_0\otimes\mathbf{a}_0 + \mathbf{a}_0\otimes\mathbf{a}_0\otimes\mathbf{C}^{-1}\right) + \frac{1}{9}\bar{I}_4\mathbf{C}^{-1}\otimes\mathbf{C}^{-1} - \frac{1}{3}\bar{I}_4\frac{\partial \mathbf{C}^{-1}}{\partial \mathbf{C}}. \tag{27}$$

The spatial description the elasticity tensor is defined as the push-forward operation of $\mathbb{C}$ as

$$\mathbb{c} = \boldsymbol{\chi}_*(\mathbb{C}), \quad c_{ijkl} = \frac{1}{J}F_{iI}F_{jJ}F_{kK}F_{lL}C_{IJKL}, \tag{28}$$

Note that the push-forward operation of the tensor $-\partial \mathbf{C}^{-1}/\partial \mathbf{C}$ is equal to the fourth-order identity tensor $\mathbb{I}$:

$$F_{iI}F_{jJ}F_{kK}F_{lL}\left(\frac{\partial \mathbf{C}^{-1}}{\partial \mathbf{C}}\right)_{IJKL} = -\frac{1}{2}(\delta_{ik}\delta_{jl} + \delta_{il}\delta_{jk}) = -(\mathbb{I})_{ijkl}. \tag{29}$$

In tensor notation $\mathbb{c}$ is expressed as:

$$\mathbb{c} = \mathbb{c}_{vol} + \mathbb{c}_{iso}, \tag{30}$$

$$\mathbb{c}_{vol} = -2\kappa(J-1)\mathbb{I} + 2\kappa(J-\frac{1}{2})\mathbf{1}\otimes\mathbf{1}, \tag{31}$$

$$\begin{aligned}J\mathbb{c}_{iso} &= 4\psi_{11}\mathrm{dev}\bar{\mathbf{B}}\otimes\mathrm{dev}\bar{\mathbf{B}} + 4\psi_{14}\left(\mathrm{dev}\bar{\mathbf{B}}\otimes\mathrm{dev}(\bar{\mathbf{a}}\otimes\bar{\mathbf{a}}) + \mathrm{dev}(\bar{\mathbf{a}}\otimes\bar{\mathbf{a}})\otimes\mathrm{dev}\bar{\mathbf{B}}\right) \\ &\quad +4\psi_{44}\mathrm{dev}(\bar{\mathbf{a}}\otimes\bar{\mathbf{a}})\otimes\mathrm{dev}(\bar{\mathbf{a}}\otimes\bar{\mathbf{a}}) \\ &\quad -\frac{2}{3}\left(\mathbf{1}\otimes\bar{\boldsymbol{\sigma}} + \bar{\boldsymbol{\sigma}}\otimes\mathbf{1}\right) + \frac{2}{9}(\mathrm{tr}\bar{\boldsymbol{\sigma}})\mathbf{1}\otimes\mathbf{1} + \frac{2}{3}\mathrm{tr}\bar{\boldsymbol{\sigma}}\mathbb{I}.\end{aligned} \tag{32}$$

The material model was implemented in the finite element program `ABAQUS` using the user subroutine `UMAT`. The implementation of the six Cauchy stress components and the tangent stiffness is required. More details on the implementation of the tangent stiffness matrix are given in Appendix A.

3 Numerical examples

The strain energy function expressed in eq.(9) is employed here. It is of a form that captures the hyperelastic behavior of soft biological tissues with one–family of collagen fibres well.
The material parameters c_0, c_1 and c_2 were set equal to: $c_0 = 0.052\,\text{kPa}$, $c_1 = 4.63$, $c_2 = 22.6$ for all the analyses presented in this Section. Note that these material parameters are those proposed by Prot et al. [16] for porcine mitral anterior leaflet by fitting those given first by May-Newman and Yin [12] for an alternative strain energy function.

3.1 Biaxial test simulations

Although it is recommended to use hybrid (mixed) elements for incompressible materials in `ABAQUS`, we investigate first how our material model performs with a pure displacement based finite element. With this, we can determine required magnitudes of κ.
Displacement controlled single element tests were carried out in order to check the proper implementation of the stress and tangent stiffness updates within `ABAQUS` of the material model derived from eq.(9). First, an equibiaxial test was carried out with an eight-noded solid element (`ABAQUS` element type C3D8) for different values of κ in order to show the importance of using a large value to treat the material as incompressible.
In this test, the nodal displacements of the element were imposed as boundary conditions. The same displacements were imposed in the 1 and 2 directions, the element was left free to deform in the 3-direction and the fibre direction was aligned with the 1-direction.
The theoretical principal stretches were determined assuming material incompressibility. From the strain energy function,

$$W = c_0 \left(e^{c_1 (I_1 - 3)^2 + c_2 (I_4 - 1)^2} - 1 \right) + p(J - 1), \tag{33}$$

the theoretical Cauchy stresses were calculated assuming a state of plane stress [16]:

$$\boldsymbol{\sigma} = 2W_1 \mathbf{B} + 2W_4 \mathbf{a} \otimes \mathbf{a} + p\mathbf{1}, \quad \mathbf{a} = \mathbf{F}\mathbf{a}_0, \tag{34}$$

$$\text{with} \quad W_1 = \frac{\partial W}{\partial I_1} \quad \text{and} \quad W_4 = \frac{\partial W}{\partial I_4}, \tag{35}$$

with, $p = -2\psi_1 B_{33}$, determined from the plane stress condition, $\sigma_{33} = 0$,

$$[\mathbf{B}] = \begin{bmatrix} B_{11} & B_{12} & 0 \\ B_{12} & B_{22} & 0 \\ 0 & 0 & B_{33} \end{bmatrix}, \tag{36}$$

$$B_{33} = (B_{11} B_{22} - B_{12}^2)^{-1}, (\det \mathbf{B} = 1). \tag{37}$$

In Figure 1, the theoretical Cauchy stress in the 1-direction is compared with the numerical stresses obtained from the finite element analyses using $\kappa = 10^3$, 10^4, 10^5, and 10^6. It appears that the numerical stresses converge toward the theoretical solution when κ is increased. $\kappa = 10^6$ gives an excellent agreement between the analytical and numerical solutions. The value of J is plotted for different values of κ in Figure 2. In figure 6.3(a) the theoretical Cauchy stresses in the 1 and 2–directions were then compared with those obtained from the finite element analysis using $\kappa = 10^6$.

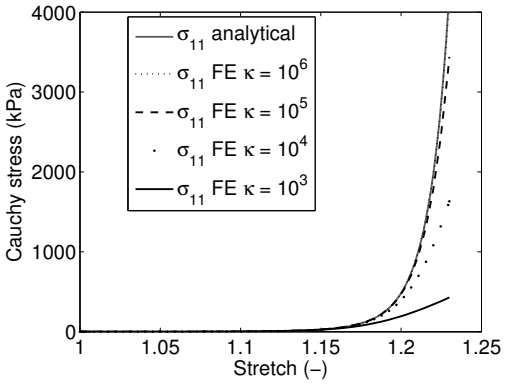

Figure 1: Cauchy stress-stretch curves for a single element equibiaxial test, the same displacements were imposed in the 1 and 2 directions, the 3-direction was left free to deform and the fibre direction aligned with the 1-direction. Analytical values of σ_{11} in the 1-direction are compared with the numerical values obtained with different values of κ.

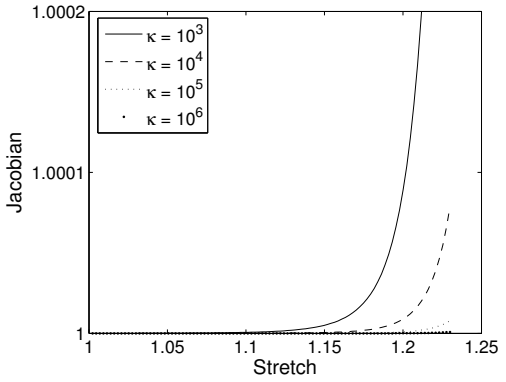

Figure 2: Numerical values of J obtained with different values of κ for a single element equibiaxial test in which the same displacements were imposed in the 1 and 2 directions, the 3-direction was left free to deform and the fibre direction aligned with the 1-direction.

Next, another equibiaxial test was analysed with the fibre direction in the 1-2 plane making an angle of 30° with the 1-direction, i.e. the vector $\mathbf{a}_0$, representing the fibre direction in the reference configuration had the following matrix form in the base $(\mathbf{e}_1, \mathbf{e}_2, \mathbf{e}_3)$,

$$[\mathbf{a}_0] = \left[\begin{array}{ccc} \cos(30^\circ) & \sin(30^\circ) & 0 \end{array} \right]^T. \tag{38}$$

The same boundary conditions as in the previous test were used. The theoretical Cauchy stresses in the 1 and 2–directions and the shear stress in the 1–2 plane expressed as,

$$\sigma_{11} = 2W_1\lambda_1^2 + 2W_4\lambda_1^2 cos(30^\circ)^2 - 2W_1\frac{1}{(\lambda_1\lambda_2)^2}, \tag{39}$$

$$\sigma_{22} = 2W_1\lambda_2^2 + 2W_4\lambda_2^2 sin(30^\circ)^2 - 2W_1\frac{1}{(\lambda_1\lambda_2)^2}, \tag{40}$$

$$\sigma_{12} = 2W_4\lambda_1\lambda_2 cos(30^\circ) sin(30^\circ), \tag{41}$$

where λ_1 and λ_2 are the stretches in the 1 and 2–directions, respectively, were then compared with those obtained from the finite element analysis (see Figure 6.3(b)) using $\kappa = 10^6$ kPa. As

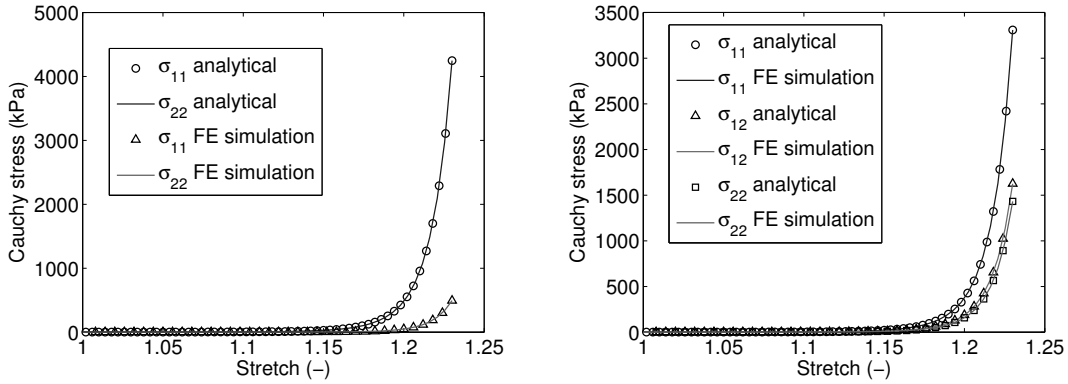

(a) the fibre direction aligned with the 1-direction

(b) the fibre direction is located in 1-2 plane and makes an angle of 30° with the 1-direction

Figure 3: Cauchy stress-stretch curves for a single element equibiaxial test: comparison of theoretical Cauchy stresses with numerical stresses obtained from the `UMAT` subroutine. Stress values σ_{11} are in the 1-direction, and σ_{22} in the 2-direction. The same displacements were imposed in the 1 and 2 directions, the 3-direction was left free to deform.

can be seen from Figure 3, the single element equibiaxial tests illustrate an excellent agreement between the theoretical and the numerical solutions.

3.2 Comparison between solid and membrane elements

In order to compare the implementation of the material model derived from eq.(9) described in Section 2 for solid elements with the implementation of the same material model described by Prot et al. [16] for membrane and shell elements, a part of a sphere (see Figure 4) is subjected to a uniform pressure. Note that the stresses presented in this section are the result of post–processed nodal stresses.

The displacements of the circular edge of the geometry were constrained and a uniform pressure p of 16 kPa was applied on the convex surface. Note that 16 kPa (120 mmHg) corresponds to a typical peak systolic blood pressure for a healthy person. The fibre direction was arranged in the circumferential direction as shown in Figure 4. The first material direction was aligned with the circumferential direction, the second material direction with the meridional direction and the third material direction was defined to be perpendicular to the other material directions. The thickness of the model in the reference configuration t_0 was uniform and equal to 1 mm. For the solid element case κ was set equal to 10^6 kPa. The geometry was meshed with three–noded membrane elements (`ABAQUS` type M3D3) and with eight–noded solid hybrid elements (`ABAQUS` type C3D8H), respectively. In order to apply the same boundary conditions for all cases presented in this section, the geometry was meshed with an even number of elements through the thickness in the solid element cases. After loading, the initial shape, see Figure 6.5(a), took an ogival shape, see Figure 6.5(b). For the solid element case J was equal to 1 up

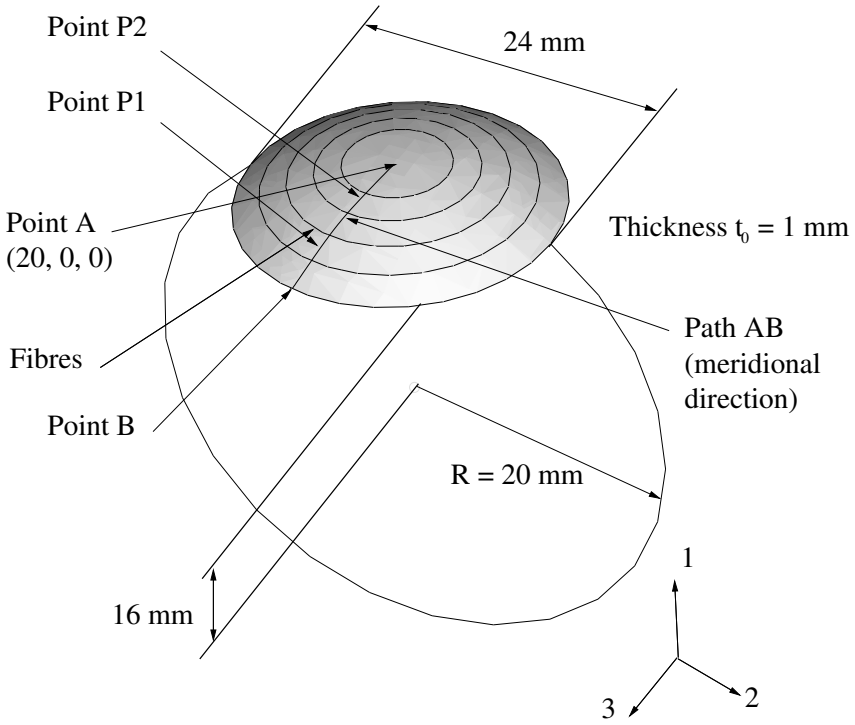

Figure 4: Part of a sphere made of a transversely isotropic material.

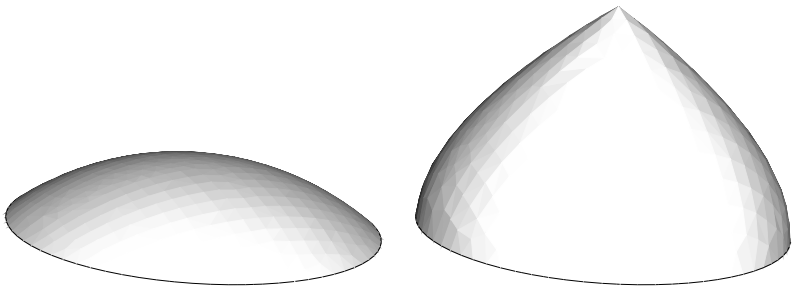

(a) Reference configuration (b) Deformed configuration

Figure 5: Part of a sphere subjected to a uniform pressure on the interior face (a) Reference configuration, (b) Deformed configuration.

to five digits.

In the case of soft biological tissue reinforced by one family of collagen fibres like for instance the mitral leaflets, the material parameter c_2 governs the stiffness in the collagen fibre direction. In order to study the effect of the fibre structure with the model presented in this section two other analyses using solid elements were conducted on the same model with different layers through the thickness: one with two layers having a thickness of 0.5 mm and each meshed with two solid elements, in this case the material parameter c_2 was set equal to zero in the layer adjacent to the concave surface of the geometry and c_2 was kept equal to 22.6 in the other layer, and a second one with three layers having the same thicknesses of $\frac{1}{3}$ mm and meshed with two solid elements for each layer, c_2 was set equal to zero in the outer layers and kept equal to 22.6

in the middle layer.
The displacement of point A in the 1–direction (see Figure 4) is plotted in Figure 6 for all cases. Figure 6 shows a very good agreement between the simulation using membrane elements and the one using solid elements with uniform collagen fibre distribution over the thickness.
In order to check the results obtained with the finite element analyses we compared the stresses

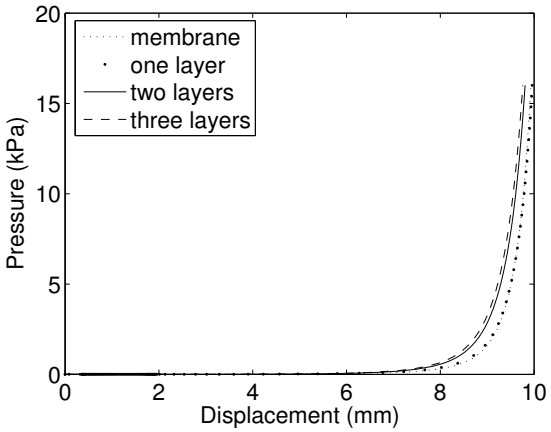

Figure 6: Displacement of the point A in the 1–direction (see Figure 4) versus pressure for the membrane and solid cases.

calculated along the path AB, see Figure 4, with Laplace's law:

$$\frac{\bar{\sigma}_1}{r_1} + \frac{\bar{\sigma}_2}{r_2} = \frac{p}{t}, \tag{42}$$

where r_1 and r_2 are the principal radius of curvature of the membrane, $\bar{\sigma}_1$ and $\bar{\sigma}_2$ are the principal membrane stresses, respectively. p is the pressure acting on the membrane and t is the current thickness of the membrane. Note that Laplace's law is independent of the material constitutive model. As the problem is axisymmetric the stresses along the path AB are representative for the whole model.
For the membrane element case, the stresses obtained from the finite element analysis must obey Laplace's law. However, for the solid element analyses this need not be the case. Our motivation here for comparing the stresses obtained with the solid finite element analyses to Laplace's law is to investigate on a simple geometry how the layer arrangements employed here and in the next Section affect the stress response, and especially how much it deviates from the membrane behavior. These analyses are carried out as a precursor of the mitral valve simulations in the next section.
In the problem described in this section, the principal radius of curvature r_1 and r_2 are normal to the circumferential and meridional directions, respectively. In order to determine the varying principal radii of curvature corresponding to the deformed geometry at many steps in the analysis, the profiles of the deformed configurations were fitted to polynomial functions, for more details see [23]. $\bar{\sigma}_1$ and $\bar{\sigma}_2$ correspond to the membrane stress in the fibre direction and meridional direction, respectively.
In the case using membrane elements $\bar{\sigma}_1$ and $\bar{\sigma}_2$ are straightforward to determine. In the cases using solid elements the membrane stresses $\bar{\sigma}_1$ and $\bar{\sigma}_2$ are calculated by dividing the membrane

forces in each direction by the current thickness t calculated from the deformed configuration and using the post–processed nodal stresses. The membrane forces N_1 and N_2 are derived from:

$$N_1 = \int_t \sigma_1(t)dt \simeq \sum_{i=1}^{N_{el-layer}} \bar{\sigma}_1^i \Delta t_i, \quad N_2 = \int_t \sigma_2(t)dt \simeq \sum_{i=1}^{N_{el-layer}} \bar{\sigma}_2^i \Delta t_i, \tag{43}$$

where $\bar{\sigma}^i$ is the average stress in the solid element layer i. Then the average membrane stresses are calculated as,

$$\bar{\sigma}_1^{FE} = \frac{N_1}{t}, \quad \bar{\sigma}_2^{FE} = \frac{N_2}{t}. \tag{44}$$

The sum

$$\frac{\bar{\sigma}_1^{FE}}{r_1} + \frac{\bar{\sigma}_2^{FE}}{r_2}, \tag{45}$$

where $\bar{\sigma}_1^{FE}$ and $\bar{\sigma}_2^{FE}$ are both calculated from the finite element analysis, is plotted against p/t in Figures 7(a)-(d) for the membrane element case and the solid element cases using one, two and three layers, respectively, at three different pressure levels (30 mmHg, 60 mmHg and 120 mmHg) and at several locations along the path AB. Note that the corresponding pressure dependent r_1, r_2, t were employed with eq.(42).

As expected, Figure 6.7(a) shows a very good agreement between the finite element results and Laplace's law for the case using membrane elements. The deviation observed between the finite element results and Laplace's law for the cases using solid elements (see Figures 6.7(b), 6.7(c) and 6.7(d)) may be due bending introduced by using solid elements: this means that the load is not carried only by the membrane forces but also by bending moments. However, the three cases using solid elements show a quite good agreement with Laplace's law.

Figure 8, illustrating the stress distribution through the thickness at points P1 and P2 (see Figure 4) at 120 mmHg in all the cases presented in this Section, shows that the analysis using solid elements with one homogeneous material layer yields the most homogeneous stress distribution through the thickness in both directions. Figure 8 also shows that in this example the peak stresses in both directions are increased with the cases using two and three material layers. At a given pressure level (120 mmHg) and at a given location along the path AB, Figure 6.9(a) shows that $\bar{\sigma}_1^{FE}$ has a quite similar value in each case except in the neighbourhood of point B. However, Figure 8 shows that the stress distribution over the thickness is very different from one case to an other. In order to investigate how much bending is introduced in the response of the structure for each case, two ratios R_1 and R_2 defined as,

$$R_1 = \frac{M_1}{N_1\sqrt{r_s t}}, \quad R_2 = \frac{M_2}{N_2\sqrt{r_s t}}, \tag{46}$$

are plotted along the path AB in Figure 6.9(b), where M_1 and M_2 are bending moments defined as,

$$M_1 = \int_t \sigma_1(t)tdt, \quad M_2 = \int_t \sigma_2(t)tdt, \tag{47}$$

N_1 and N_2 (eq.(43)) are membrane forces, r_s is the radius of the circular edge of the structure (where the boundary conditions are applied) shown in Figure 4 and t is the current thickness of

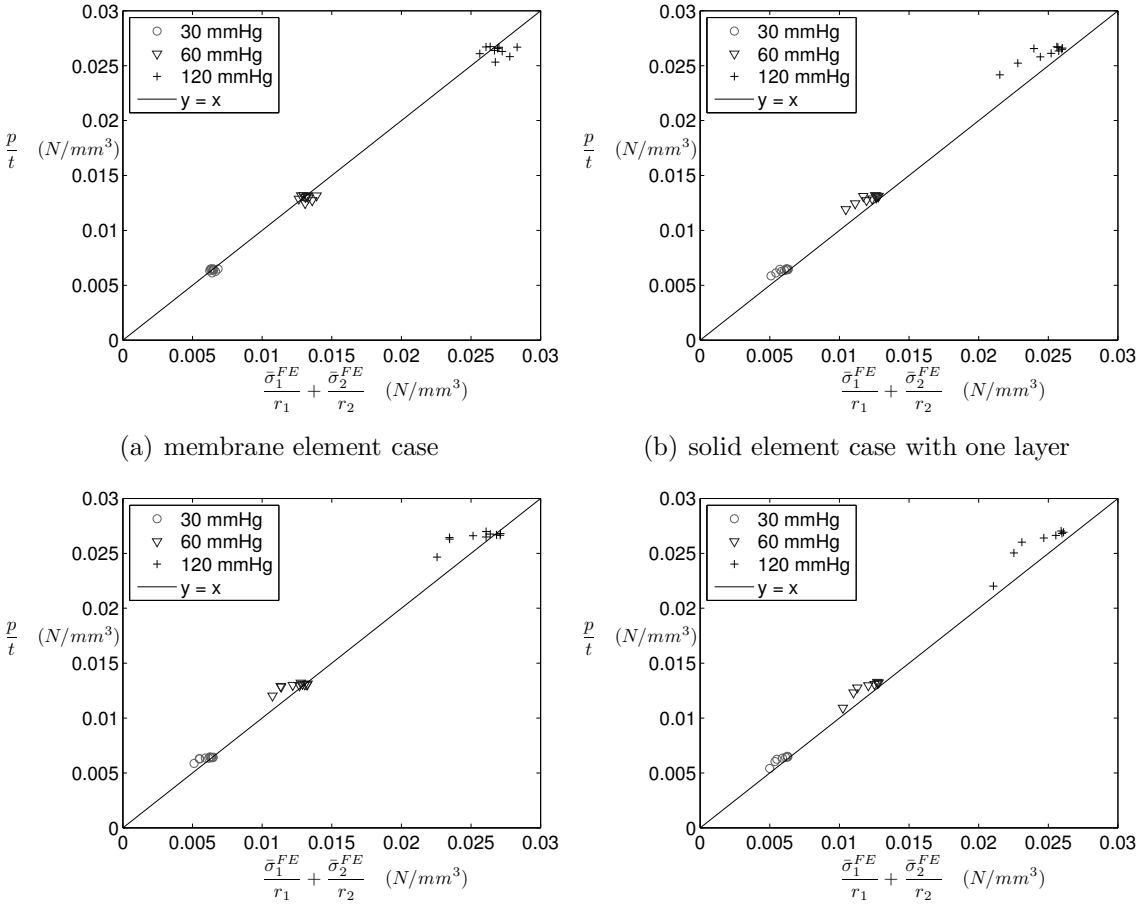

(a) membrane element case

(b) solid element case with one layer

(c) solid element case with two layers

(d) solid element case with three layers

Figure 7: The sum $\frac{\bar{\sigma}_1^{FE}}{r_1} + \frac{\bar{\sigma}_2^{FE}}{r_2}$ where $\bar{\sigma}_1^{FE}$ and $\bar{\sigma}_2^{FE}$ are both calculated from the finite element analyses is plotted against p/t and represented by circles, plusses and triangles at 30 mmHg, 60 mmHg, and 120 mmHg, respectively, for different locations along the path AB (see, Figure 4). t, r_1 and r_2 are calculated from the deformed configuration of the finite element model. The solid line shows where the symbols, i.e. $\circ$, $\bigtriangledown$ and $+$, would be located if the finite element analysis followed exactly Laplace's law.

the structure along the path AB. As can be seen from Figure 6.9(b), both ratios R_1 and R_2 are significantly inferior to unity meaning that in each case the problem is membrane dominated. However, the case using two layers introduces the most bending in the structure described in this section.

3.3 Mitral valve simulations

In this section a three dimensional finite element model of a porcine mitral valve is presented. The closure of the valve between early systole ($p = 0$) and peak systole ($p = 120$ mmHg) is considered. Note that in this section the stresses plotted through the thickness of the leaflets are post–processed nodal stresses.

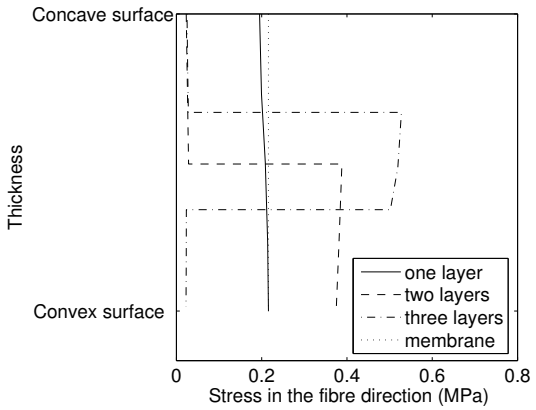

(a) Stress through the thickness along the fibres at point P1 (see Figure 4) at 120 mmHg

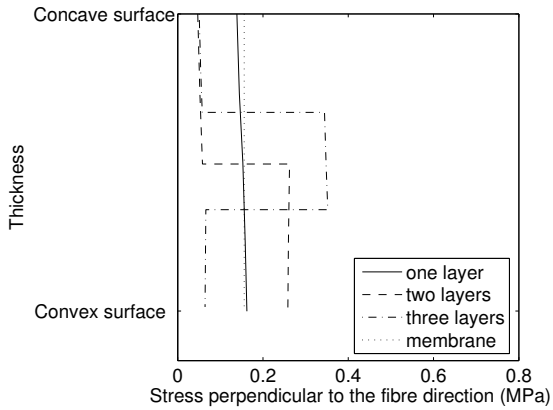

(b) Stress through the thickness perpendicular to the fibres at point P1 (see Figure 4) at 120 mmHg

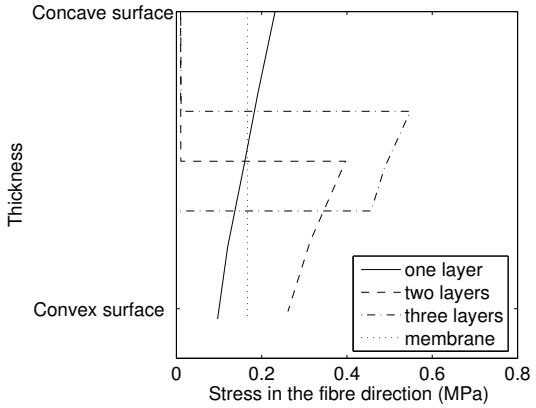

(c) Stress through the thickness along the fibres at point P2 (see Figure 4) at 120 mmHg

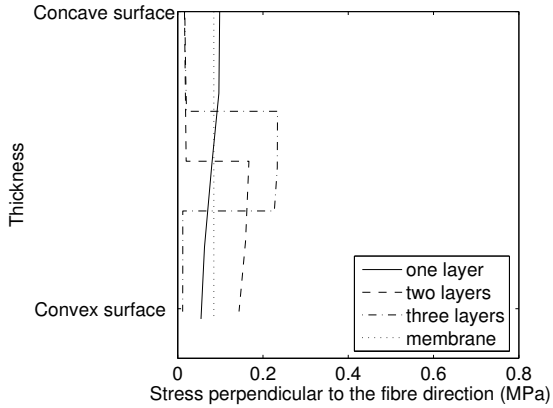

(d) Stress through the thickness perpendicular to the fibres at point P2 (see Figure 4) at 120 mmHg

Figure 8: (a) Cauchy stress parallel to the fibres at point P1, (b) Cauchy stress perpendicular to the fibres at point P1, (c) Cauchy stress parallel to the fibres at point P2, (d) Cauchy stress perpendicular to the fibres at point P2.

Geometry, material and boundary conditions

The geometry of the model is shown in Figure 10 and the modelling of the chordae tendinae are described by Prot et al. [6]. The shape of the annulus was measured at early systole from 3D ultrasound measurements carried out on the heart of the anaesthetized animal. The annulus was idealized as a nonplanar ellipse. The distance between the highest point of the anterior annulus to the highest point of the posterior annulus was 30.9 mm. The distance between the two commissures was 34.1 mm. The saddle height, defined as the distance between the highest point of the anterior annulus and the plane defined by the posterior annulus, was 4.81 mm. The maximum distance from the annulus to the free edge of the anterior and posterior leaflets were measured to be 23 mm and 11 mm, respectively, post mortem. The thickness of the leaflets was assumed to be constant and equal to 1 mm. The cross section areas of the chordae used in our model were based on the average values given by Liao and Vesely [24]: 0.38 mm^2 and

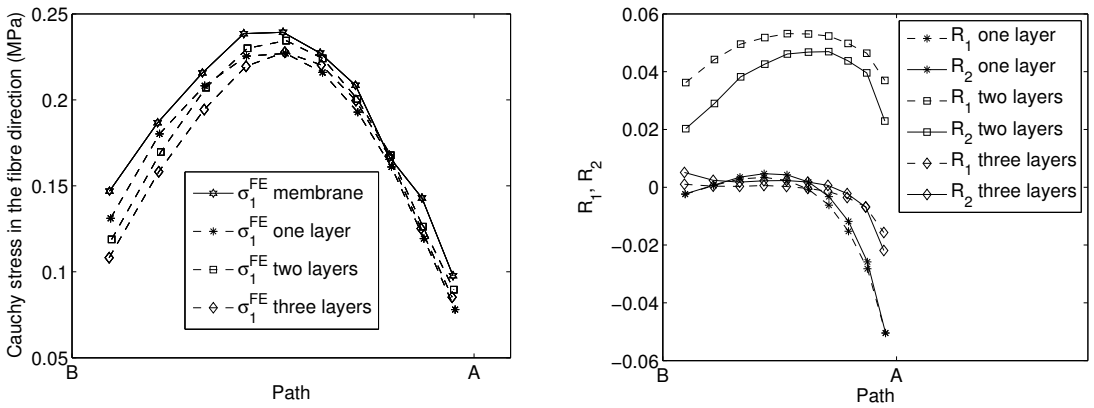

(a) $\bar{\sigma}_1^{FE}$ along the path AB (b) R_1 and R_2 (see eq.(46)) along the path AB

Figure 9: (a) $\bar{\sigma}_1^{FE}$ along the path AB (see Figure 4) at 120 mmHg for all the cases, (b) R_1 and R_2 (see eq.(46)) along the path AB at 120 mmHg for the cases using solid elements.

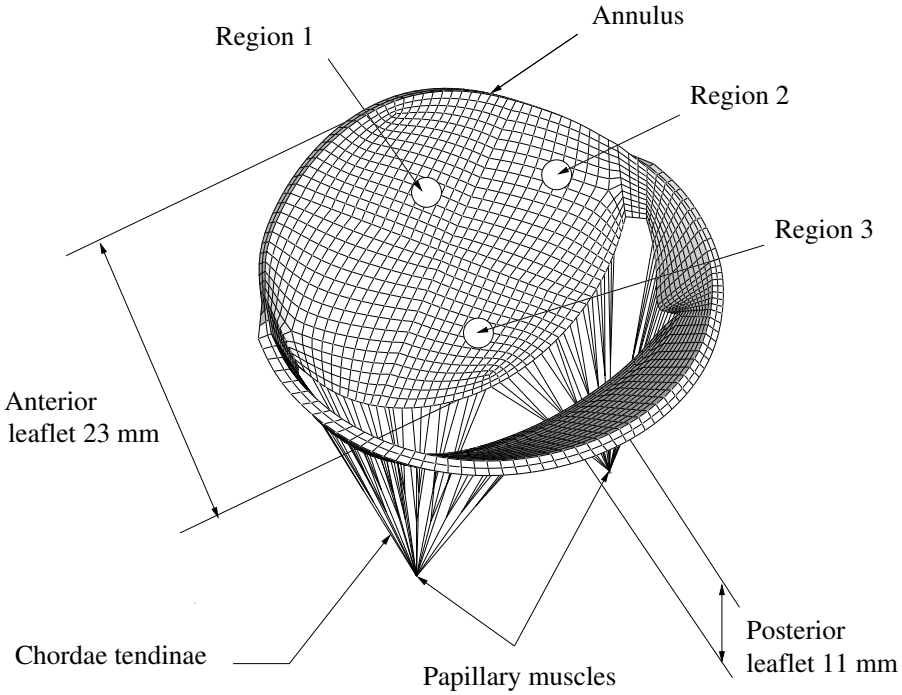

Figure 10: Initial geometry of the mitral valve at beginning of systole.

2.05 mm^2 for marginal (primary) and strut (secondary) chordae, respectively.
The constitutive model derived from eq.(9) was used for both leaflets using the material parameters in Table 1.

The chordae were modeled as an incompressible hyperelastic material. The nonlinear stress-stretch behaviour was implemented from experimental data published in [25]. The same material model was used for all the chordae, derived from the following strain energy function,

$$U(I_1) = a_1(\exp^{(a_2(I_1-1))} - 1), \tag{48}$$

Table 1: Material parameter values for the strain-energy function (9)

	c_0(kPa)	c_1	c_2
Anterior leaflet	0.0520	4.63	22.6
Posterior leaflet	0.171	5.28	6.46

$a_1 = 0.0565$ kPa and $a_2 = 29.6$ for the marginal (primary) chordae and $a_1 = 0.050$ kPa and $a_2 = 35$ for the strut (secondary) chordae.
The fibre orientation was set in the leaflets using the `ABAQUS` user subroutine ORIENT according to the mean collagen fibre direction map from SALS data shown by Einstein et al. [26].
The leaflets were meshed with eight noded brick hybrid elements (C3D8H `ABAQUS` type) and the chordae with truss elements (T3D2 `ABAQUS` type). The mesh in the initial configuration is shown in Figure 10.
The displacements of two nodes representing the papillary muscles were constrained. The annulus was assumed to be fixed, with translations constrained but not the rotations. In order to capture coaptation (i.e., apposition of the posterior and anterior leaflets) a contact condition was prescribed on the atrium surface of the leaflets. The blood pressure measured in the left ventricle of the pig between beginning of systole and the maximum pressure in the ventricle was applied on the ventricular surface of the leaflets as load history. All simulations were quasi–static.

Collagen structure

Collagen fibres are a major component of the mitral apparatus and play an important role in providing mechanical strength to the leaflets. In this section we use a simplistic approach to study the influence of the position of the collagenous layer. As the material parameter c_2 of the strain energy function (9) governs the stiffness in the fibre direction, we used the values of c_2 related in Table 1 for the collagenous layer and $c_2 = 0$ in the other layers. Note that using $c_2 = 0$ corresponds to the use of an isotropic hyperelastic material model. Kunzelman et al. [7] found that the mitral leaflets may be divided into three layers and that the middle layer (fibrosa) of the leaflet, composed of dense collagen, was the stiffest layer in the mitral leaflets. However, near the annulus the thickness of the mitral valve leaflet is dominated by the fibrosa (collagen dominated layer) and the ventricularis is the thinnest of the layers and disappears toward the free edge. Thus, the layer arrangement of the leaflets may be simplified as one heavily collagenous layer on the ventricular side (fibrosa) and one loose connective tissue layer (atrialis/spongiosa) on the atrium side.
Hence, as in Section 3.2, three analyses with different layer arrangements were conducted with different material properties in the layers.
In case one, the leaflets were modeled with one material layer of 1 mm with two solid elements through the thickness using the material properties in Table 1 (i.e. collagen uniformly distributed over thickness). In case two, the leaflets were modeled with two material layers (0.5 mm each) meshed with one solid element for each layer : the material parameter c_2 was equal to zero in the atrium layers of both leaflets and kept equal to 22.6 and 6.46 in the ventricular layers of the anterior and posterior leaflets, respectively. In case three, the leaflets were modeled with three material layers ($\frac{1}{3}$ mm each) meshed with one solid element for each layer: the material

parameter c_2 was equal to zero in the atrium and ventricular layers of both leaflets and kept equal to 22.6 and 6.46 in the middle layers of the anterior and posterior leaflets, respectively. The material layer arrangements of the three cases are illustrated in Figure 11.

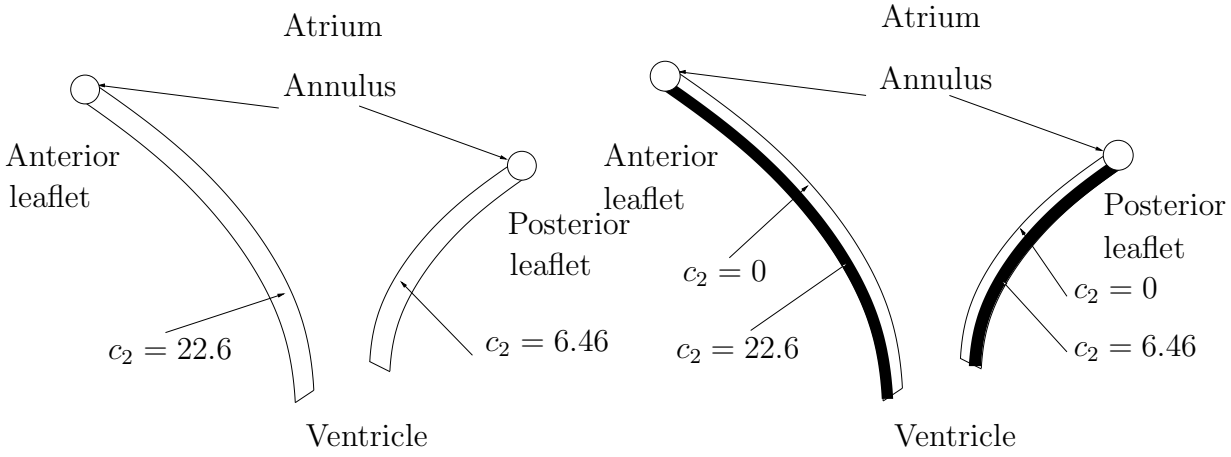

(a) case one (two homogeneous solid element layers)

(b) case two (two solid element layers)

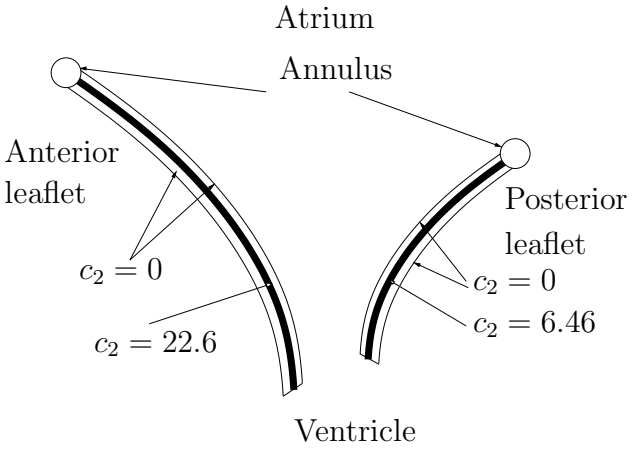

(c) case three (three solid element layers)

Figure 11: Collagen arrangement in the mitral leaflet for the three cases

Stress distribution through the thickness

In all cases, the mitral valve completed coaptation very early in systole. The deformed shape of the valve as shown in Figure 12, was very similar in the three cases studied in this section. However, Figures 13 and 14 illustrate the stress distribution through the thickness of the anterior leaflet in three regions (see Figure 10). As can be seen the stress distribution through the thickness of the leaflet is quite different for the three cases. As can be seen in Figure 13, the stresses in the atrium surface and in the ventricular surface are reduced and increased, respectively, with the leaflet composed of two different layers compared to the case with constant material properties through the thickness. Hence, especially in region 1, i.e. in the middle part of the anterior leaflet at about one third of the distance between the annulus and the coaptation line, the model using two different layers homogenizes the stress distribution through

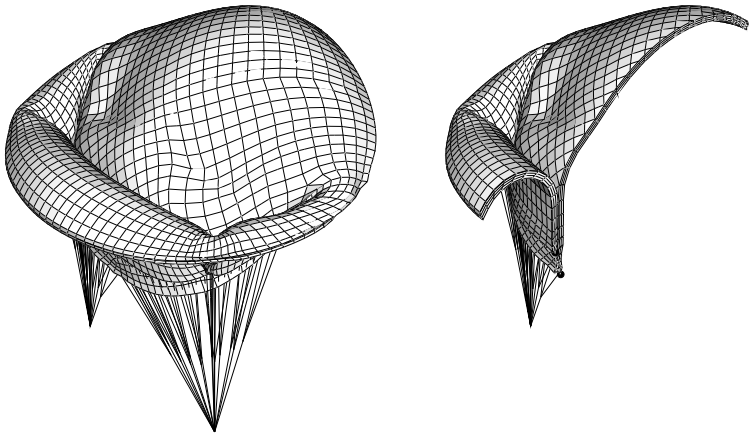

(a) Deformed configuration of the mitral valve

(b) Deformed configuration of the mitral valve (cut view)

Figure 12: Deformed configuration of the mitral valve at peak systole

the thickness in the fibre direction (see Figure 6.13(a)). However, this is not the case in the direction perpendicular to the fibres (see Figure 14). The analyses show that the anterior leaflet experiences greater stresses on the atrium side compared to a membrane approach, but no compressive stress on the ventricular side.

Comparison with echocardiographic measurements

In this Section, as the deformed shapes are very similar for the three cases, results using two layers of solid elements with homogeneous material properties over the leaflet thickness are presented (Figure 6.11(a)). Among all of the chordae attached to the mitral leaflets two of them are larger and longer. They are called strut chordae and are attached on the ventricular surface of the anterior leaflet beyond the free edge. As they carry a large part of the load due to the blood pressure applied on the valve leaflets during systole these chordae have an important supportive role in the mitral apparatus [6], [27]. In addition, they are characterized by a large attachment area to the anterior leaflet ventricular surface.
In the present model the chordae are meshed with truss elements. In order to model the attachment of the strut chordae to the anterior leaflet, the extremity of the chordae arising from the leaflet was divided into multiple branches. First these branches were attached at several points along the circumferential direction, as shown in Figure 6.15(a). Note that this modelling for the strut chordae was used for the simulations presented in the previous section. In Figure 16 the solid line representing the deformed shape of the leaflet obtained from the finite element analysis with this configuration is compared with the ultrasound measurements carried out on the pig for several pressure levels. As can be seen in Figures 6.16(b) and 6.16(c) the anterior leaflet bulges too much into the left atrium compared to the echocardiographic measurement. Hence, in order to reduce the bulging of the anterior leaflet into the left atrium the modelling of the strut chordae was slightly modified: several branches were added and attached along the radial direction as shown in Figure 6.15(b). The dashed line in Figures 6.16(b) and 6.16(c) shows that this second configuration for the strut chordae reduces the bulging of the leaflet somewhat but does not give the flat shape that the anterior leaflet exhibits

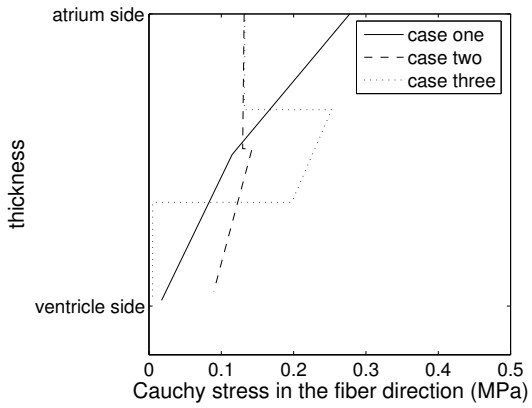

(a) Cauchy stress in the fibre direction, region 1 (see, Figure 10)

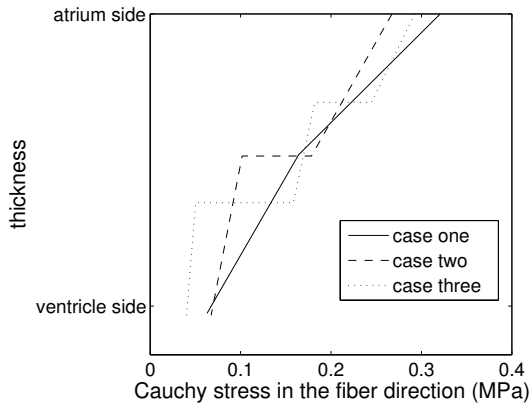

(b) Cauchy stress in the fibre direction, region 2 (see, Figure 10)

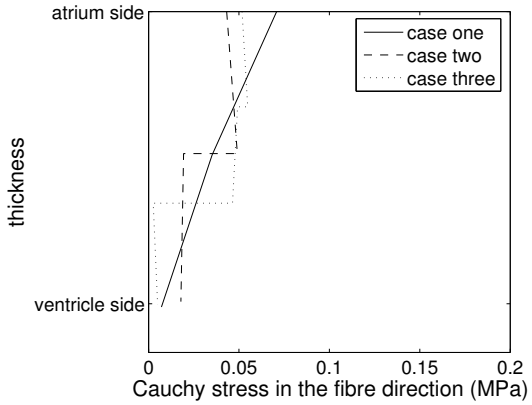

(c) Cauchy stress in the fibre direction, region 3 (see, Figure 10)

Figure 13: Cauchy stress in the fibre direction through the thickness of the anterior leaflet, in region 1, region 2 and region 3 (see, Figure 10), for each case shown in Figure 11.

in the echocardiographic images. In Figure 6.16(d) the deformed shape of the leaflets at peak systole obtained with the simulations using solid elements with the two configurations for the strut chordae modelling (see Figure 15) and a simulation using membrane elements are plotted with the deformed profile of the leaflets observed in the ultrasound measurement. As can be seen, the deformed profiles obtained from the simulations are quite similar. However, the coaptation area is slightly translated toward the anterior annulus in the case using membrane elements.

4 Discussion

A constitutive model for an incompressible hyperelastic transversely isotropic material has been presented for use in solid finite element analysis. Incompressibility was modeled via a penalty method. With a single element test, we show the required magnitude of the penalty

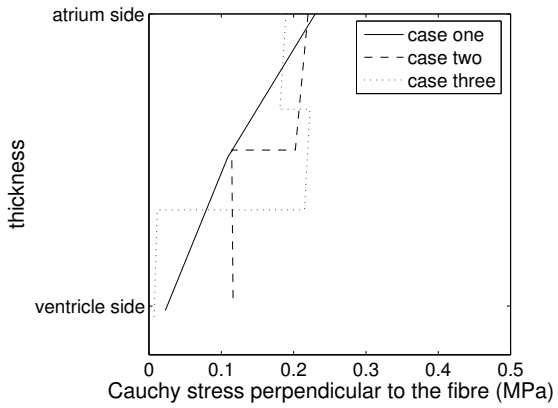

(a) Cauchy stress perpendicular to the fibre direction, region 1 (see, Figure 10)

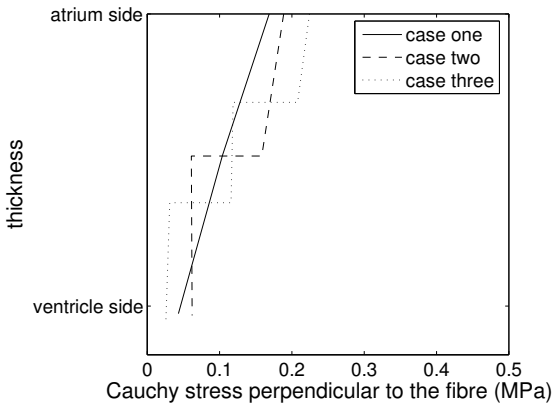

(b) Cauchy stress perpendicular to the fibre direction, region 2 (see, Figure 10)

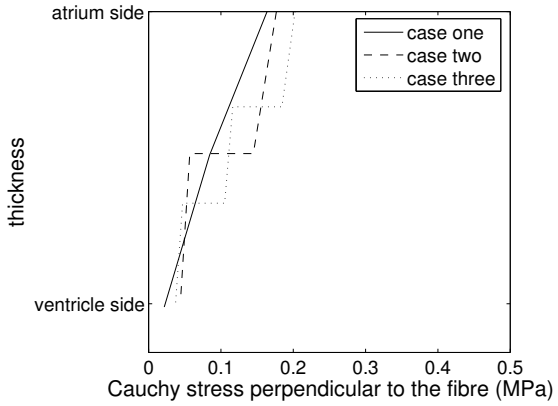

(c) Cauchy stress perpendicular to the fibre direction, region 3 (see, Figure 10)

Figure 14: Cauchy stress perpendicular to the fibre direction through the thickness of the anterior leaflet, in region 1, region 2 and region 3 (see, Figure 10), for each case shown in Figure 11.

parameter κ in order to obtain a good agreement with the analytical solution. The use of hybrid elements is recommended with the incompressible hyperelastic material model, in this case `ABAQUS` recalculates the hydrostatic stress implemented in UMAT and modifies the tangent stiffness matrix accordingly.

The out of plane loading example performed on a part of a sphere shows that the average membrane stresses are not much affected by the different layer arrangements used in this study. However, we found that in this example the case using three different layers with fibres in the central layer was the closest to the membrane behaviour: it minimizes the bending stress in this particular structure and the load bearing is mainly by membrane forces.

In order to study the influence of the collagen structure in the mitral valve leaflets, a simplistic approach has been used. The thicknesses of the different layers of the mitral leaflets are almost constant in the direction parallel to the annulus but vary from the annulus to the free edge [7]. This was not accounted for in this study. In addition, we do not attempt to give layer specific

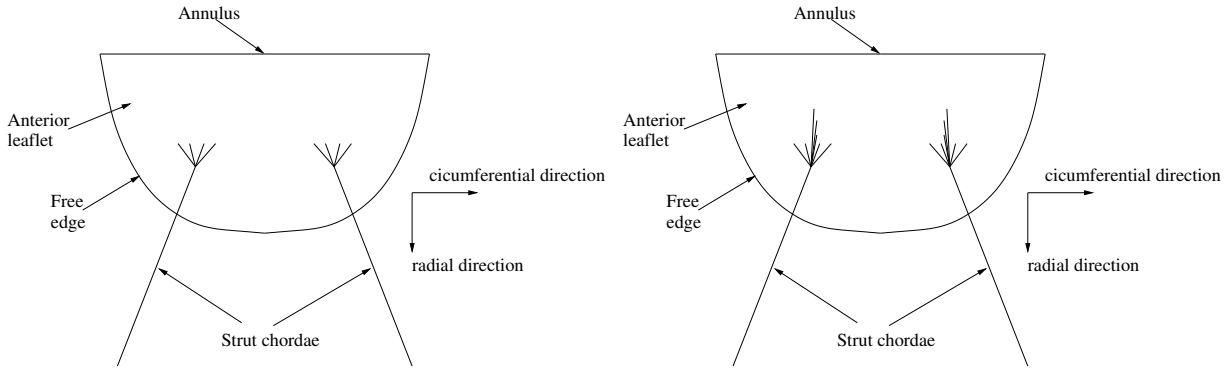

(a) strut chordae modelling 1 (b) strut chordae modelling 2

Figure 15: (a) The strut chordae are modeled with branches attached at some points of the anterior leaflet along the circumferential direction, (b) The strut chordae are modeled with branches attached at some points of the anterior leaflet along the circumferential direction and along the radial direction.

material parameters for the different layers of the leaflets.
Our finite element simulations show that in the central part of the anterior leaflet, when the anterior leaflet is divided in two layers with the collagen layer on the ventricular side, the stresses in the fibre direction are reduced and the resistance to bending of the leaflets is reduced in that direction compared to the case with only one uniform layer. In both directions the stresses are higher on the atrium side than on the ventricular side of the leaflets for all collagen arrangements used in this study. In addition no compressive stress is observed in the directions parallel and perpendicular to the fibres.
The stress distributions presented in this work have to be considered with care since our model exhibits too much bulging. Indeed, comparing the deformed shape obtained from the finite element analysis to the one observed from the echocardiographic recording, we see that in our model the anterior leaflet bulges too much into the left atrium whereas the leaflets exhibit a flat shape in the ultrasound measurement. This may be due to several aspects that are not taken into account in our model. First, the pressure load applied on the leaflets is uniform which may not be the case in reality. Also, the thickness of the leaflets is constant in our model but anatomical measurements show that the leaflets are thicker near the annulus. In addition, the leaflets are modeled as a passive biological tissue. However, Sonnenblick et al. [28] showed in dogs that the anterior leaflet contains muscle fibres from atrial origin and that the electrically stimulated mitral valve actively developed tension and shortened. Moreover, Timek et al. [29] showed in sheep that these muscles fibres have a direct role in evolution of the leaflet's shape. Our results agree with Curtis and Priola [30] who studied the action the muscle fibres present in the anterior leaflet. They show that when the muscle fibres are active, the mitral valve does not bulge into the left atrium and that in the case of passified muscle fibres the valve deflection was significantly increased at any left ventricular pressure value. In [29], it is stated that: "little is known about the in vivo function of myocardial fibers, which insert into the mitral annulus and leaflet". However, shortening of the anterior leaflet due to contraction of its muscle fibres during systole may reduce its bulging into the left atrium and promote the flat shape of the leaflets during systole.

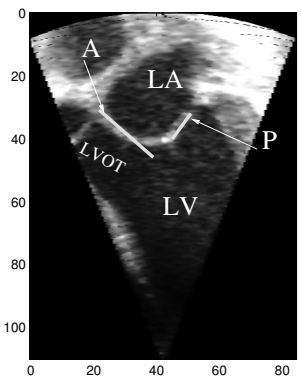

(a) Initial position (beginning of systole)

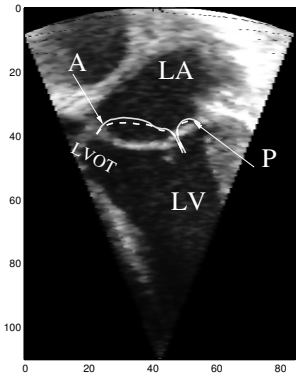

(b) 80 mmHg

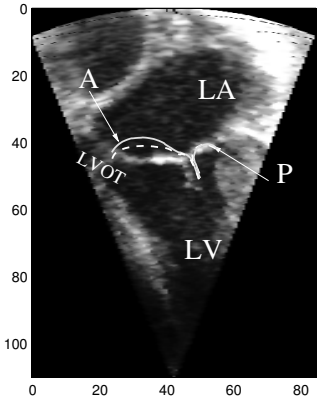

(c) peak systole (120 mmHg)

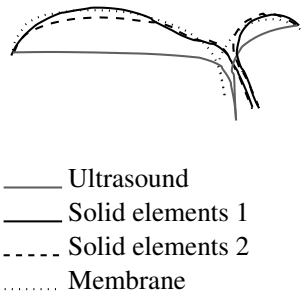

(d)

Figure 16: (a) The solid line shows the initial position of the FE model, (b) the solid and the dashed lines show the deformed shapes obtained with the finite element simulations using solid elements for the strut chordae configurations 1 and 2 (see Figure 15), respectively, at 80 mmHg,(c) the solid and the dashed lines show the deformed shapes obtained with the finite element simulations using solid elements for the strut chordae configurations 1 and 2 (see Figure 15), respectively, at 120 mmHg (d) the red line shows the deformed shape of the leaflets observed from the ultrasound recording, the solid, dashed and dot lines show the deformed shapes obtained with the finite element simulations using solid elements for the strut chordae configurations 1 and 2 (see Figure 15) and the simulation using membrane elements, respectively. (LVOT = Left Ventricular Outflow Tract, LA = left atrium, LV = left ventricle, A = anterior, P = posterior)

Our simulations show that the use of a transversely isotropic hyperelastic material model for the mitral leaflet will induce bulging of the valve into the left atrium and even with a larger attachment zone of the strut chordae to the ventricular surface of the valve this bulging remains. However, the three dimensional finite element model of the mitral apparatus presented in this study shows the great mobility of the anterior leaflet coming in apposition with the posterior leaflet during left ventricular isovolumetric contraction. The two leaflets come into contact

at their respective rough zone giving a large coaptation area. Hence, despite the discrepancy observed in the deformed shape of the leaflets at peak systole our model simulates a proper closure of the valve. Furthermore, the simulations indicate that even for a passive (no leaflet muscle fibre contraction) leaflet, regurgitation does not occur.

5 Conclusion

The present study suggests that the material heterogeneity employed herein does not influence much the global response of the mitral valve. However, our results show that the stress in the leaflets are affected by using layers with different material properties. In the central part of the anterior leaflet, the stresses in the fibre direction and the resistance to bending of the leaflet are reduced in that area when the leaflets are modeled with two material layers. Furthermore for all the material layer arrangements used in this study the stresses were higher on the atrium side than on the ventricular side of the leaflets. We show that using a passive transversely isotropic hyperelastic material model for the leaflets the valve bulges too much in the left atrium. We conclude that the flat shape of the leaflets shown by the ultrasound recording may be due to the presence of active muscle fibres. Hence, for improved material modelling, the account of muscle fibres need further studies and layer–specific material parameters need also to be established.

ACKNOWLEDGEMENT

The authors are grateful to Professor G. A. Holzapfel for helpful discussions on constitutive modelling.
The authors want also to acknowledge Simula Research Laboratory AS (Center of excellence, biomedical computing, CBC) for providing financial support for parts of this research.

Appendix A

The spatial tangent moduli $\mathbb{c}$ defined in eq.(28) gives the following relationship,

$$\mathcal{L}_{\mathcal{V}}\boldsymbol{\tau} = \dot{\boldsymbol{\tau}} - \mathbf{L}\boldsymbol{\tau} - \boldsymbol{\tau}\mathbf{L}^T = J\mathbb{c} : \mathbf{D}, \tag{49}$$

where $\boldsymbol{\tau} = J\boldsymbol{\sigma}$ is the Kirchhoff stress tensor, $\mathbf{L}$ the velocity gradient, $\mathbf{D}$ the rate of deformation, and $\mathcal{L}_{\mathcal{V}}\boldsymbol{\tau}$ the convected rate of the Kirchhoff stress, also called the Lie derivative of the Kirchhoff stress. We note also that $\mathbf{L} = \mathbf{D} + \mathbf{W}$ where $\mathbf{D}$ is the symmetric part of the velocity gradient. The Jaumann objective stress rate $\boldsymbol{\tau}^{\nabla\mathcal{J}}$ is used in ABAQUS/Standard for continuum elements,

$$\boldsymbol{\tau}^{\nabla\mathcal{J}} = \dot{\boldsymbol{\tau}} - \mathbf{W}\boldsymbol{\tau} - \boldsymbol{\tau}\mathbf{W}^T = \mathbb{C}^{\tau\mathcal{J}} : \mathbf{D}, \tag{50}$$

where $\mathbb{C}^{\tau\mathcal{J}}$ is the Jaumann (Kirchhoff) tangent moduli. This leads to the following relation between the spatial second elasticity tensor $\mathbb{C}$ and the Jaumann (Kirchhoff) tangent moduli

$\mathbb{C}^{\tau\mathcal{J}}$ [31]:

$$\begin{aligned}\mathcal{L}_{\mathcal{V}}\boldsymbol{\tau} &= \boldsymbol{\tau}^{\nabla\mathcal{J}} - (\mathbf{L}-\mathbf{W})\boldsymbol{\tau} - \boldsymbol{\tau}(\mathbf{L}-\mathbf{W})^T = J\mathbb{C} : \mathbf{D} \\ &= \boldsymbol{\tau}^{\nabla\mathcal{J}} - \mathbf{D}\boldsymbol{\tau} - \boldsymbol{\tau}\mathbf{D}, \qquad (51)\\ J\mathbb{C} : \mathbf{D} &= \mathbb{C}^{\tau\mathcal{J}} : \mathbf{D} - J\mathbb{C}^{'} : \mathbf{D}, \qquad (52)\\ \mathbb{C}^{\tau\mathcal{J}} &= J\left(\mathbb{C} + \mathbb{C}^{'}\right), \qquad (53)\\ \text{where} \quad \mathbb{C}^{'} : \mathbf{D} &= \mathbf{D}\boldsymbol{\sigma} + \boldsymbol{\sigma}\mathbf{D}, \qquad (54)\\ \text{with,} \quad C^{'}_{ijkl} &= \frac{1}{2}(\delta_{ik}\sigma_{jl} + \delta_{il}\sigma_{jk} + \delta_{jk}\sigma_{il} + \delta_{jl}\sigma_{ik}). \qquad (55)\end{aligned}$$

The fourth order tensor $\mathbb{C}^{'}$ possesses the major and minor symmetries. Now, in `ABAQUS` the spatial fourth order tensor $\mathbb{c}^{\texttt{ABAQUS}}$ needs to be implemented, i.e,

$$\mathbb{c}^{\texttt{ABAQUS}} = \frac{1}{J}\mathbb{C}^{\tau\mathcal{J}}, \qquad (56)$$

or in index notation,

$$c^{\texttt{ABAQUS}}_{ijkl} = c_{ijkl} + \frac{1}{2}(\delta_{ik}\sigma_{jl} + \delta_{il}\sigma_{jk} + \delta_{jk}\sigma_{il} + \delta_{jl}\sigma_{ik}). \qquad (57)$$

c_{ijkl} is the push-forward of the material elasticity tensor $\mathbb{C}$ in the current configuration according to (28). This term needs to be updated for each material model derived from a specific strain energy function. The second term $C^{'}_{ijkl}$ of the spatial tensor implemented in the user-defined subroutine UMAT needs to be coded once only.

References

[1] Kunzelman KS, Cochran RP, Chuong C, Ring WS, Verrier ED, and Eberhart RD. Finite element analysis of the mitral valve. *J. Heart Valve Dis.* 1993; **2**:326–340.

[2] Einstein DR, Kunzelman KS, Reinhall P, Nicosia M, and Cochran RP. Haemodynamic determinants of the mitral valve closure sound: a finite element study. *Med. & Biol. Eng. & Comput.* 2004; **42**:832–846.

[3] Votta E, Maisano F, Soncini M, Redaelli A, Montevecchi FM, and Alfieri O. 3-D computational analysis of the stress distribution on the leaflets after edge-to-edge repair of mitral regurgitation. *J. Heart Valve Dis.* 2002; **11**:810–822.

[4] Dal Pan F, Donzella G, Fucci C, and Schreiber M. Structural effects of an innovative surgical technique to repair heart valve defects. *J. Biomech.* 2005; **38**:2460–2471.

[5] Lim KH, Yeo JH, Duran CM. Three-dimensional asymmetrical modeling of the mitral valve: a finite element study with dynamic boundaries. *J Heart Valve Dis.* 2005; **14**:386392, 2005.

[6] Prot V, Haaverstad R, Skallerud B. Finite element analysis of the mitral apparatus: annulus shape effect and chordal force distribution. *J. Biomechanics and Modeling in Mechanobiology.* Accepted, 2007.

[7] Kunzelman KS, Cochran RP, Murphree SS, Ring WS, Verrier ED, Eberhart RC. Differential collagen distribution in the mitral valve and its influence on biomechanical behavior. *J. Heart Valve Dis.* 1993; **2**:236-244.

[8] Grande-Allen KJ, Calabro A, Gupta V, Wight TN, Hascall VC, Vesely I. Glycosaminoglycans and proteoglycans in normal mitral valve leaflets and chordae: association with regions of tensile and compressive loading. *Glycobiology* 2004 **14(7)**:621–633.

[9] Jensen A, Baandrup U, Hasenkam J, Kundu T, Jørgensen C. Distribution of the microelastic properties within the human anterior mitral leaflet. *Ultrasound in Medicine & Biology* 2006; **2(12)**:1943–1948, 2006.

[10] Kuhl E and Holzapfel GA. A continuum model for remodeling in living structures. *J. Mater. Sci.* 2007 **42**:8811–8823.

[11] Prot V, Skallerud B, Holzapfel GA. Effects of connective tissue pathologies on mitral valve response. *MHM 2007, Modelling of heterogeneous materials with applications in construction and biomedical engineering, Prague* 2007; 106-107.

[12] May-Newman K and Yin FCP. A constitutive law for mitral valve tissue. *J. Biomech. Eng.* 1998; **120**:38–47.

[13] Weiss JA, Maker BN, and Govindjee S. Finite element implementation of incompressible, transversely isotropic hyperelasticity. *Comput. Meth. Appl. Mech. Eng.* 1996; **135**:107–128.

[14] Rüter M and Stein E. Analysis, finite element computation and error estimation in transversely isotropic nearly incompressible finite elasticity. *Comput. Meth. Appl. Mech. Eng.* 2000; **190(5)**: 519–541.

[15] Holzapfel GA, Gasser TC, Ogden RW. A new constitutive framework for arterial wall mechanics and a comparative study of material models. *Journal of Elasticity* 2000; **61**:1-48.

[16] Prot V, Skallerud B, Holzapfel GA. Transversely isotropic membrane shells with application to mitral valve mechanics. Constitutive modeling and finite element implementation. *Int. J. Numer. Meth. Eng.* 2007; **71(8)**, 987–1008.

[17] Gruttmann F and Taylor RL. Theory and finite element formulation of rubberlike membrane shells using principal stretches. *Int. J. Numer. Meth. Eng.* 1992; **35**:1111–1126.

[18] Simo JC, Taylor RL, Pister KS. Variational and projection methods for the volume constraint in finite deformation elasto-plasticity. *Comput. Meth. Appl. Mech. Eng.* 1985; **51**:177–208.

[19] Holzapfel GA. *Nonlinear Solid Mechanics. A Continuum Approach for Engineering.* John Wiley & Sons, Chichester, 2000.

[20] Flory PJ. Thermodynamics relations for high elastic materials. *Trans. Faraday Soc.* 1961; **57**:829–838.

[21] Schröder J and Neff P. Invariant formulation of hyperelastic transverse isotropy based on polyconvex free energy functions. *Int. J. Solids Structures*, 2003; **40**:401–445.

[22] Balzani D, Neff P, Schröder J, and Holzapfel GA. A polyconvex framework for soft biological tissues. adjustment to experimental data. *Int. J. Solids Structures*, 2006; **43**:6052–6070.

[23] Humphrey JD. *Cardiovascular Solid Mechanics. Cells, Tissues, and Organs.* Springer–Verlag New York, pp139–140, 2002.

[24] Liao J, Vesely I. A structural basis for the size-related mechanical properties of mitral valve chordae tendineae. *J. Biomech.* 2003; **36(8)**:1125–33.

[25] Kunzelman KS and Cochran RP. Mechanical properties of basal and marginal mitral valve chordae tendineae. *ASAIO Trans.* 1990; **36**:M405–408.

[26] Einstein DR, Kunzelman KS, Reinhall P, Nicosia M, and Cochran RP. The relationship of normal and abnormal microstructural proliferation to the mitral valve closure sound. *J. biomech. eng.* 2005; **127(1)**:134–147.

[27] Jimenez JH, Soerensen DD, He Z, He S, Yoganathan AP. Effects of a Saddle Shaped Annulus on Mitral Valve Function and Chordal Force Distribution: An In Vitro Study. *Annals of Biomedical Engineering* 2003; **31**:1171–1181.

[28] Sonnenblick EH, Napolitano LM, Daggett WM, and Cooper T. An intrinsic neuromuscular basis for mitral valve motion in the dog. *Circ. Res.* 1967; **21**:9-15.

[29] Timek TA, Lai DT, Dagum P, Tibayan F, Daughters GT, Liang D, Berry GJ, Miller DC and Ingels NB. Ablation of mitral annular and leaflet muscle: effects on annular and leaflet dynamics. *Am. J. Physiol. Heart Circ. Physiol.* 2003; **285**:1668-1674.

[30] Curtis BC and Priola DV. Mechanical properties of the canine mitral valve: effects of autonomic stimulation. Am. J. Physiol. 1992; **31**:56–62.

[31] Belytschko T, Liu WK and Moran B. *Nonlinear finite elements for continua and structures.* John Wiley & Sons, Chichester, pp231–232, 2000.

PAPER IV

Healthy and hypertrophic obstructive cardiomyopathic human mitral valves and chordae tendinae: mechanical experiments, constitutive modelling, finite element analyses

V. Prot, B. Skallerud, G. Sommer, G. A. Holzapfel

Submitted, 2008

Is not included due to copyright

DEPARTMENT OF STRUCTURAL ENGINEERING
NORWEGIAN UNIVERSITY OF SCIENCE AND TECHNOLOGY

N7491 TRONDHEIM, NORWAY
Telephone: +47 73 59 47 00 Telefax: +47 73 59 47 01

"Reliability Analysis of Structural Systems using Nonlinear Finite Element Methods",
C. A. Holm, 1990:23, ISBN 82-7119-178-0.

"Uniform Stratified Flow Interaction with a Submerged Horizontal Cylinder",
Ø. Arntsen, 1990:32, ISBN 82-7119-188-8.

"Large Displacement Analysis of Flexible and Rigid Systems Considering Displacement-Dependent Loads and Nonlinear Constraints",
K. M. Mathisen, 1990:33, ISBN 82-7119-189-6.

"Solid Mechanics and Material Models including Large Deformations",
E. Levold, 1990:56, ISBN 82-7119-214-0, ISSN 0802-3271.

"Inelastic Deformation Capacity of Flexurally-Loaded Aluminium Alloy Structures",
T. Welo, 1990:62, ISBN 82-7119-220-5, ISSN 0802-3271.

"Visualization of Results from Mechanical Engineering Analysis",
K. Aamnes, 1990:63, ISBN 82-7119-221-3, ISSN 0802-3271.

"Object-Oriented Product Modeling for Structural Design",
S. I. Dale, 1991:6, ISBN 82-7119-258-2, ISSN 0802-3271.

"Parallel Techniques for Solving Finite Element Problems on Transputer Networks",
T. H. Hansen, 1991:19, ISBN 82-7119-273-6, ISSN 0802-3271.

"Statistical Description and Estimation of Ocean Drift Ice Environments",
R. Korsnes, 1991:24, ISBN 82-7119-278-7, ISSN 0802-3271.

"Properties of concrete related to fatigue damage: with emphasis on high strength concret",
G. Petkovic, 1991:35, ISBN 82-7119-290-6, ISSN 0802-3271.

"Turbidity Current Modelling",
B. Brørs, 1991:38, ISBN 82-7119-293-0, ISSN 0802-3271.

"Zero-Slump Concrete: Rheology, Degree of Compaction and Strength. Effects of Fillers as Part Cement-Replacement",
C. Sørensen, 1992:8, ISBN 82-7119-357-0, ISSN 0802-3271.

"Nonlinear Analysis of Reinforced Concrete Structures Exposed to Transient Loading",
K. V. Høiseth, 1992:15, ISBN 82-7119-364-3, ISSN 0802-3271.

"Finite Element Formulations and Solution Algorithms for Buckling and Collapse Analysis of Thin Shells",
R. O. Bjærum, 1992:30, ISBN 82-7119-380-5, ISSN 0802-3271.

"Response Statistics of Nonlinear Dynamic Systems",
J. M. Johnsen, 1992:42, ISBN 82-7119-393-7, ISSN 0802-3271.

"Digital Models in Engineering. A Study on why and how engineers build and operate digital models for decisison support",
J. Høyte, 1992:75, ISBN 82-7119-429-1, ISSN 0802-3271.

"Sparse Solution of Finite Element Equations",
A. C. Damhaug, 1992:76, ISBN 82-7119-430-5, ISSN 0802-3271.

"Some Aspects of Floating Ice Related to Sea Surface Operations in the Barents Sea",
S. Løset, 1992:95, ISBN 82-7119-452-6, ISSN 0802-3271.

"Modelling of Cyclic Plasticity with Application to Steel and Aluminium Structures",
O. S. Hopperstad, 1993:7, ISBN 82-7119-461-5, ISSN 0802-3271.

"The Free Formulation: Linear Theory and Extensions with Applications to Tetrahedral Elements with Rotational Freedoms",
G. Skeie, 1993:17, ISBN 82-7119-472-0, ISSN 0802-3271.

"Høyfast betongs motstand mot piggdekkslitasje. Analyse av resultater fra prøving i Veisliter'n",
T. Tveter, 1993:62, ISBN 82-7119-522-0, ISSN 0802-3271.

"A Nonlinear Finite Element Based on Free Formulation Theory for Analysis of Sandwich Structures",
O. Aamlid, 1993:72, ISBN 82-7119-534-4, ISSN 0802-3271.

"The Effect of Curing Temperature and Silica Fume on Chloride Migration and Pore Structure of High Strength Concrete",
C. J. Hauck, 1993:90, ISBN 82-7119-553-0, ISSN 0802-3271.

"Failure of Concrete under Compressive Strain Gradients",
G. Markeset, 1993:110, ISBN 82-7119-575-1, ISSN 0802-3271.

"An experimental study of internal tidal amphidromes in Vestfjorden",
J. H. Nilsen, 1994:39, ISBN 82-7119-640-5, ISSN 0802-3271.

"Structural analysis of oil wells with emphasis on conductor design",
H. Larsen, 1994:46, ISBN 82-7119-648-0, ISSN 0802-3271.

"Adaptive methods for non-linear finite element analysis of shell structures",
K. M. Okstad, 1994:66, ISBN 82-7119-670-7, ISSN 0802-3271.

"On constitutive modelling in nonlinear analysis of concrete structures",
O. Fyrileiv, 1994:115, ISBN 82-7119-725-8, ISSN 0802-3271.

"Fluctuating wind load and response of a line-like engineering structure with emphasis on

motion-induced wind forces",
J. Bogunovic Jakobsen, 1995:62, ISBN 82-7119-809-2, ISSN 0802-3271.

"An experimental study of beam-columns subjected to combined torsion, bending and axial actions",
A. Aalberg, 1995:66, ISBN 82-7119-813-0, ISSN 0802-3271.

"Scaling and cracking in unsealed freeze/thaw testing of Portland cement and silica fume concretes",
S. Jacobsen, 1995:101, ISBN 82-7119-851-3, ISSN 0802-3271.

"Damping of water waves by submerged vegetation. A case study of laminaria hyperborea",
A. M. Dubi, 1995:108, ISBN 82-7119-859-9, ISSN 0802-3271.

"The dynamics of a slope current in the Barents Sea",
Sheng Li, 1995:109, ISBN 82-7119-860-2, ISSN 0802-3271.

"Modellering av delmaterialenes betydning for betongens konsistens",
Ernst Mørtsell, 1996:12, ISBN 82-7119-894-7, ISSN 0802-3271.

"Bending of thin-walled aluminium extrusions",
Birgit Søvik Opheim, 1996:60, ISBN 82-7119-947-1, ISSN 0802-3271.

"Material modelling of aluminium for crashworthiness analysis",
Torodd Berstad, 1996:89, ISBN 82-7119-980-3, ISSN 0802-3271.

"Estimation of structural parameters from response measurements on submerged floating tunnels",
Rolf Magne Larssen, 1996:119, ISBN 82-471-0014-2, ISSN 0802-3271.

"Numerical modelling of plain and reinforced concrete by damage mechanics",
Mario A. Polanco-Loria, 1997:20, ISBN 82-471-0049-5, ISSN 0802-3271.

"Nonlinear random vibrations - numerical analysis by path integration methods",
Vibeke Moe, 1997:26, ISBN 82-471-0056-8, ISSN 0802-3271.

"Numerical prediction of vortex-induced vibration by the finite element method",
Joar Martin Dalheim, 1997:63, ISBN 82-471-0096-7, ISSN 0802-3271.

"Time domain calculations of buffeting response for wind sensitive structures",
Ketil Aas-Jakobsen, 1997:148, ISBN 82-471-0189-0, ISSN 0802-3271.

"A numerical study of flow about fixed and flexibly mounted circular cylinders",
Trond Stokka Meling, 1998:48, ISBN 82-471-0244-7, ISSN 0802-3271.

"Estimation of chloride penetration into concrete bridges in coastal areas",
Per Egil Steen, 1998:89, ISBN 82-471-0290-0, ISSN 0802-3271.

"Stress-resultant material models for reinforced concrete plates and shells",
Jan Arve Øverli, 1998:95, ISBN 82-471-0297-8, ISSN 0802-3271.

"Chloride binding in concrete. Effect of surrounding environment and concrete composition",
Claus Kenneth Larsen, 1998:101, ISBN 82-471-0337-0, ISSN 0802-3271.

"Rotational capacity of aluminium alloy beams",

Lars A. Moen, 1999:1, ISBN 82-471-0365-6, ISSN 0802-3271.

“Stretch Bending of Aluminium Extrusions”,
Arild H. Clausen, 1999:29, ISBN 82-471-0396-6, ISSN 0802-3271.

“Aluminium and Steel Beams under Concentrated Loading”,
Tore Tryland, 1999:30, ISBN 82-471-0397-4, ISSN 0802-3271.

“Engineering Models of Elastoplasticity and Fracture for Aluminium Alloys”,
Odd-Geir Lademo, 1999:39, ISBN 82-471-0406-7, ISSN 0802-3271.

“Kapasitet og duktilitet av dybelforbindelser i trekonstruksjoner”,
Jan Siem, 1999:46, ISBN 82-471-0414-8, ISSN 0802-3271.

“Etablering av distribuert ingeniørarbeid; Teknologiske og organisatoriske erfaringer fra en norsk ingeniørbedrift”,
Lars Line, 1999:52, ISBN 82-471-0420-2, ISSN 0802-3271.

“Estimation of Earthquake-Induced Response”,
Símon Ólafsson, 1999:73, ISBN 82-471-0443-1, ISSN 0802-3271.

“Coastal Concrete Bridges: Moisture State, Chloride Permeability and Aging Effects” Ragnhild Holen Relling, 1999:74, ISBN 82-471-0445-8, ISSN 0802-3271.

“Capacity Assessment of Titanium Pipes Subjected to Bending and External Pressure”,
Arve Bjørset, 1999:100, ISBN 82-471-0473-3, ISSN 0802-3271.

“Validation of Numerical Collapse Behaviour of Thin-Walled Corrugated Panels”,
Håvar Ilstad, 1999:101, ISBN 82-471-0474-1, ISSN 0802-3271.

“Strength and Ductility of Welded Structures in Aluminium Alloys”,
Miroslaw Matusiak, 1999:113, ISBN 82-471-0487-3, ISSN 0802-3271.

“Thermal Dilation and Autogenous Deformation as Driving Forces to Self-Induced Stresses in High Performance Concrete”,
Øyvind Bjøntegaard, 1999:121, ISBN 82-7984-002-8, ISSN 0802-3271.

“Some Aspects of Ski Base Sliding Friction and Ski Base Structure”,
Dag Anders Moldestad, 1999:137, ISBN 82-7984-019-2, ISSN 0802-3271.

“Electrode reactions and corrosion resistance for steel in mortar and concrete”,
Roy Antonsen, 2000:10, ISBN 82-7984-030-3, ISSN 0802-3271.

“Hydro-Physical Conditions in Kelp Forests and the Effect on Wave Damping and Dune Erosion. A case study on Laminaria Hyperborea”,
Stig Magnar Løvås, 2000:28, ISBN 82-7984-050-8, ISSN 0802-3271.

“Random Vibration and the Path Integral Method”,
Christian Skaug, 2000:39, ISBN 82-7984-061-3, ISSN 0802-3271.

“Buckling and geometrical nonlinear beam-type analyses of timber structures”,
Trond Even Eggen, 2000:56, ISBN 82-7984-081-8, ISSN 0802-3271.

“Structural Crashworthiness of Aluminium Foam-Based Components”,
Arve Grønsund Hanssen, 2000:76, ISBN 82-7984-102-4, ISSN 0809-103X.

"Measurements and simulations of the consolidation in first-year sea ice ridges, and some aspects of mechanical behaviour",
Knut V. Høyland, 2000:94, ISBN 82-7984-121-0, ISSN 0809-103X.

"Kinematics in Regular and Irregular Waves based on a Lagrangian Formulation",
Svein Helge Gjøsund, 2000-86, ISBN 82-7984-112-1, ISSN 0809-103X.

"Self-Induced Cracking Problems in Hardening Concrete Structures",
Daniela Bosnjak, 2000-121, ISBN 82-7984-151-2, ISSN 0809-103X.

"Ballistic Penetration and Perforation of Steel Plates",
Tore Børvik, 2000:124, ISBN 82-7984-154-7, ISSN 0809-103X.

"Freeze-Thaw resistance of Concrete. Effect of: Curing Conditions, Moisture Exchange and Materials",
Terje Finnerup Rønning, 2001:14, ISBN 82-7984-165-2, ISSN 0809-103X

"Structural behaviour of post tensioned concrete structures. Flat slab. Slabs on ground",
Steinar Trygstad, 2001:52, ISBN 82-471-5314-9, ISSN 0809-103X.

"Slipforming of Vertical Concrete Structures. Friction between concrete and slipform panel",
Kjell Tore Fosså, 2001:61, ISBN 82-471-5325-4, ISSN 0809-103X.

"Some numerical methods for the simulation of laminar and turbulent incompressible flows",
Jens Holmen, 2002:6, ISBN 82-471-5396-3, ISSN 0809-103X.

"Improved Fatigue Performance of Threaded Drillstring Connections by Cold Rolling",
Steinar Kristoffersen, 2002:11, ISBN: 82-421-5402-1, ISSN 0809-103X.

"Deformations in Concrete Cantilever Bridges: Observations and Theoretical Modelling",
Peter F. Takcs, 2002:23, ISBN 82-471-5415-3, ISSN 0809-103X.

"Stiffened aluminium plates subjected to impact loading",
Hilde Giæver Hildrum, 2002:69, ISBN 82-471-5467-6, ISSN 0809-103X.

"Full- and model scale study of wind effects on a medium-rise building in a built up area",
Jónas Thór Snæbjørnsson, 2002:95, ISBN82-471-5495-1, ISSN 0809-103X.

"Evaluation of Concepts for Loading of Hydrocarbons in Ice-infested water",
Arnor Jensen, 2002:114, ISBN 82-417-5506-0, ISSN 0809-103X.

"Numerical and Physical Modelling of Oil Spreading in Broken Ice",
Janne K. Økland Gjøsteen, 2002:130, ISBN 82-471-5523-0, ISSN 0809-103X.

"Diagnosis and protection of corroding steel in concrete",
Franz Pruckner, 20002:140, ISBN 82-471-5555-4, ISSN 0809-103X.

"Tensile and Compressive Creep of Young Concrete: Testing and Modelling",
Dawood Atrushi, 2003:17, ISBN 82-471-5565-6, ISSN 0809-103X.

"Rheology of Particle Suspensions. Fresh Concrete, Mortar and Cement Paste with Various Types of Lignosulfonates",
Jon Elvar Wallevik, 2003:18, ISBN 82-471-5566-4, ISSN 0809-103X.

"Oblique Loading of Aluminium Crash Components",

Aase Reyes, 2003:15, ISBN 82-471-5562-1, ISSN 0809-103X.

"Utilization of Ethiopian Natural Pozzolans",
Surafel Ketema Desta, 2003:26, ISSN 82-471-5574-5, ISSN:0809-103X.

"Behaviour and strength prediction of reinforced concrete structures with discontinuity regions",
Helge Brå, 2004:11, ISBN 82-471-6222-9, ISSN 1503-8181.

"High-strength steel plates subjected to projectile impact. An experimental and numerical study",
Sumita Dey, 2004:38, ISBN 82-471-6281-4 (electronic version), ISBN 82-471-6282-2 (printed version), ISSN 1503-8181.

"Alkali-reactive and inert fillers in concrete. Rheology of fresh mixtures and expansive reactions",
Bård M. Pedersen, 2004:92, ISBN 82-471-6401-9 (printed version), ISBN 82-471-6400-0 (electronic version), ISSN 1503-8181.

"On the Shear Capacity of Steel Girders with Large Web Openings",
Nils Christian Hagen, 2005:9 ISBN 82-471-6878-2 (printed version), ISBN 82-471-6877-4 (electronic version), ISSN 1503-8181.

"Behaviour of aluminium extrusions subjected to axial loading",
Østen Jensen, 2005:7, ISBN 82-471-6872-3 (electronic version) , ISBN 82-471-6873-1 (printed version), ISSN 1503-8181.

"Thermal Aspects of corrosion of Steel in Concrete",
Jan-Magnus Østvik, 2005:5, ISBN 82-471-6869-3 (printed version) ISBN 82-471-6868 (electronic version), ISSN 1503-8181.

"Mechanical and adaptive behaviour of bone in relation to hip replacement",
A study of bone remodelling and bone grafting. Sébastien Muller, 2005:34, ISBN 82-471-6933-9 (printed version) (ISBN 82-471-6932-0 (electronic version), ISSN 1503-8181.

"Analysis of geometrical nonlinearities with applications to timber structures",
Lars Wollebæk, 2005:74, ISBN 82-471-7050-5 (printed version), ISBN 82-471-7019-1 (electronic version), ISSN 1503-8181.

"Pedestrian induced lateral vibrations of slender footbridges",
Anders Rönnquist, 2005:102, ISBN 82-471-7082-5 (printed version), ISBN 82-471-7081-7 (electronic version), ISSN 1503-8181.

"Initial Strength Development of Fly Ash and Limestone Blended Cements at Various Temperatures Predicted by Ultrasonic Pulse Velocity",
Tom Ivar Fredvik, 2005:112, ISBN 82-471-7105-8 (printed version), ISBN 82-471-7103-1 (electronic version), ISSN 1503-8181.

"Behaviour and modelling of thin-walled cast components",
Cato Dørum, 2005:128, ISBN 82-471-7140-6 (printed version), ISBN 82-471-7139-2 (electronic version), ISSN 1503-8181.

"Behaviour and modelling of selfpiercing riveted connections",

Raffaele Porcaro, 2005:165, ISBN 82-471-7219-4 (printed version), ISBN 82-471-7218-6 (electronic version), ISSN 1503-8181.

"Behaviour and Modelling og Aluminium Plates subjected to Compressive Load",
Lars Rønning, 2005:154, ISBN 82-471-7169-1 (printed version), ISBN 82-471-7195-3 (electronic version), ISSN 1503-8181

"Bumper beam-longitudinal system subjected to offset impact loading",
Satyanarayana Kokkula, 2005:193, ISBN 82-471-7280-1 (printed version), ISBN 82-471-7279-8 (electronic version), ISSN 1503-8181.

"Control of Chloride Penetration into Concrete Structures at Early Age",
Guofei Liu, 2006:46, ISBN 82-471-7838-9 (printed version), ISBN 82-471-7837-0 (electronic version), ISSN 1503-8181.

"Modelling of Welded Thin-Walled Aluminium Structures",
Ting Wang, 2006:78, ISBN 82-471-7907-5 (printed version), ISBN 82-471-7906-7 (electronic version), ISSN 1503-8181.

"Time-variant reliability of dynamic systems by importance sampling and probabilistic analysis of ice loads",
Anna Ivanova Olsen, 2006:139, ISBN 82-471-8041-3 (printed version), ISBN 82-471-8040-5 (electronic version), ISSN 1503-8181.

"Fatigue life prediction of an aluminium alloy automotive component using finite element analysis of surface topography",
Sigmund Kyrre Ås, 2006:25, ISBN 82-471-7791-9 (printed version), ISBN 82-471-7791-9 (electronic version), ISSN 1503-8181.

"Constitutive models of elastoplasticity and fracture for aluminium alloys under strain path change",
Dasharatha Achani, 2006:76, ISBN 82-471-7903-2 (printed version), ISBN 82-471-7902-4 (electronic version), ISSN 1503-8181.

"Simulations of 2D dynamic brittle fracture by the Element-free Galerkin method and linear fracture mechanics",
Tommy Karlsson, 2006:125, ISBN 82-471-8011-1 (printed version), ISBN 82-471-8010-3 (electronic version), ISSN 1503-8181.

"Penetration and Perforation of Granite Targets by Hard Projectiles",
Chong Chiang Seah, 2006:188, ISBN 82-471-8150-9 (printed version), ISBN 82-471-8149-5 (electronic version) ISSN 1503-8181.

"Deformations, strain capacity and cracking of concrete in plastic and early hardening phases",
Tor Arne Hammer, 2007:234, ISBN 978-82-471-5191-4 (printed version), ISBN 978-82-471-5207-2 (electronic version) ISSN 1503-8181.

"Crashworthiness of dual-phase high-strength steel: Material and Component behaviour",
Venkatapathi Tarigopula, 2007:230, ISBN 82-471-5076-4 (printed version) ISBN 82-471-5093-1 (electronic version) ISSN 1503-8181.

"Fibre reinforcement in load carrying concrete structures",

Åse Lyslo Døssland, 2008:50, ISBN 978-82-471-6910-0 (printed version), ISBN 978-82-471-6924-7 (electronic version), ISSN 1503-8181.

"Low-velocity penetration of aluminium plates",
Frode Grytten, 2008:46, ISBN 978-82-471-6826-4 (printed version) ISBN 978-82-471-6843-1 (electronic version) ISSN 1503-8181.

"Robustness studies of structures subjected to large deformations",
Ørjan Fylling, 2008:24, ISBN 978-82-471-6339-9 (printed version) ISBN 978-82-471-6342-9 (electronic version) ISSN 1503-8181.

"Constitutive modelling of morsellised bone",
Knut Birger Lund, 2008:92, ISBN 978-82-471-7829-4 (printed version) ISBN 978-82-471-7832-4 (electronic version) ISSN 1503-8181.

"Experimental Investigations of Wind Loading on a Suspension Bridge Girder",
Bjørn Isaksen, 2008:131, ISBN 978-82-471-8656-5 (printed version) ISBN 978-82-471-8673-2 (electronic version) ISSN 1503-8181.

"Cracking Risk of Concrete Structures in the Hardening Phase",
Guomin Ji, 2008:198, ISBN 978-82-471-1079-9 (printed version), ISBN 978-82-471-1080-5 (electronic version) ISSN 1503-8181.